

**Cavitation on a Propeller
in a Non-uniform Flow Field**

Thesis by

Elizabeth Anne McKenney

CALIFORNIA INSTITUTE OF TECHNOLOGY

DTIC QUALITY INSPECTED 5

19950719 010

UNCLASSIFIED

SECURITY CLASSIFICATION OF THIS PAGE

Original contains color
plates: All DTIC reproductions
will be in black and
white

REPORT DOCUMENTATION PAGE

Form Approved
OMB No. 0704-01881a. REPORT SECURITY CLASSIFICATION
UNCLASSIFIED

2a. SECURITY CLASSIFICATION AUTHORITY

2b. DECLASSIFICATION/DOWNGRADING SCHEDULE

4. PERFORMING ORGANIZATION REPORT NUMBER(S)

E200.32

6a. NAME OF PERFORMING ORGANIZATION
California Institute of
Technology6b. OFFICE SYMBOL
(if applicable)

6c. ADDRESS (City, State, and ZIP Code)

Mail Code 104-44
1201 E. California
Pasadena, CA 911258a. NAME OF FUNDING/SPONSORING
ORGANIZATION

Office of Naval Research

8c. ADDRESS (City, State, and ZIP Code)

800 Quincy Street
Arlington, VA 222178b. OFFICE SYMBOL
(if applicable)

1b. RESTRICTIVE MARKINGS

3. DISTRIBUTION/AVAILABILITY OF REPORT

Approved for public release
distribution unlimited

5. MONITORING ORGANIZATION REPORT NUMBER(S)

7a. NAME OF MONITORING ORGANIZATION
Office of Naval Research

7b. ADDRESS (City, State, and ZIP Code)

4520 Executive Drive, Suite 300
San Diego, CA 92121

9. PROCUREMENT INSTRUMENT IDENTIFICATION NUMBER

10. SOURCE OF FUNDING NUMBERS

PROGRAM
ELEMENT NO.
N00014
N00014PROJECT
NO.
91
92TASK
NO.
J
JWORK UNIT
ACCESSION NO.
1295
1189

11. TITLE (Include Security Classification)

Cavitation on a Propeller in a Non-uniform Flow Field

12. PERSONAL AUTHOR(S)

McKenney, Elizabeth Anne

13a. TYPE OF REPORT

Technical

13b. TIME COVERED

FROM 1992 TO 1994

14. DATE OF REPORT (Year, Month, Day)

1995 May 23

15. PAGE COUNT

160

16. SUPPLEMENTARY NOTATION

Sponsored by the Applied Hydrodynamics Research Program administered by the Office of Naval Research, technical monitor J. Fein

17. COSATI CODES

FIELD GROUP SUB-GROUP

18. SUBJECT TERMS (Continue on reverse if necessary and identify by block number)

19. ABSTRACT (Continue on reverse if necessary and identify by block number)

Unsteady lifting surface flows are important subjects for study, both for the purposes of improving propulsive or lifting efficiency and also for mitigating the destructive effects and noise caused by cavitation. Some progress may be made by selecting a simple type of unsteadiness for closer study. In the present work, this tactic was implemented in two ways: the operation of a propeller at an angle of yaw to the freestream and the pitching oscillation of a finite-span hydrofoil.

A new facility was designed and constructed to set a propeller at an angle of yaw to the freestream, creating a fairly simple non-uniformity in the propeller inflow. Tip vortex cavitation inception measurements were made for a range of yaw angles and freestream velocities, and photographs of the cavitation were taken to illustrate the effects of the yaw angle.

The unsteady tip vortex flow field was measured on an oscillating finite aspect ratio hydrofoil using Particle Image Velocimetry (PIV), revealing how the circulation varied during

20. DISTRIBUTION/AVAILABILITY OF ABSTRACT

☒ UNCLASSIFIED/UNLIMITED ☒ SAME AS RPT. ☐ DTIC USERS

21. ABSTRACT SECURITY CLASSIFICATION

unclassified

22a. NAME OF RESPONSIBLE INDIVIDUAL

E.A. McKenney

22b. TELEPHONE (Include Area Code)

818 395-4153

22c. OFFICE SYMBOL

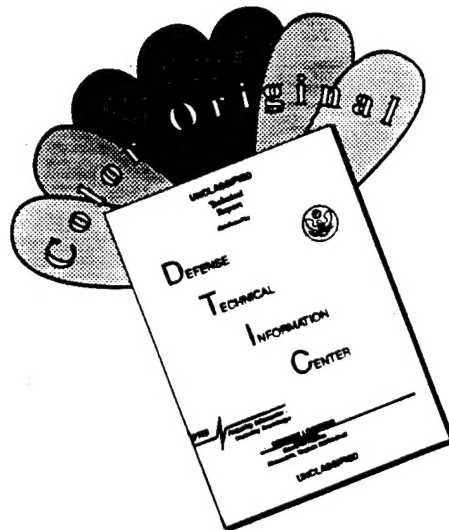
19. (continued)

a typical oscillation cycle. The results were compared with unsteady infinite-span theory, and also with recent measurements using LDV techniques on the same foil.

The hydrofoil was also the focus of a study of surface cavitation. High-speed motion pictures of the cavitation cycle helped to separate the process into its component stages, and variations with cavitation number and reduced frequency of oscillation were observed. The acoustic signals generated by the cavity collapse were correlated with the motion pictures, providing insights into the correspondence between the flow structures involved in the cavity collapse process and the sound generated by them.

The results from these studies provide valuable insights into the effects of unsteadiness in lifting surface flows.

DISCLAIMER NOTICE



THIS DOCUMENT IS BEST QUALITY AVAILABLE. THE COPY FURNISHED TO DTIC CONTAINED A SIGNIFICANT NUMBER OF COLOR PAGES WHICH DO NOT REPRODUCE LEGIBLY ON BLACK AND WHITE MICROFICHE.

A Study of Tip Vortices and Cavitation on a Propeller in a Non-uniform Inflow

Elizabeth McKenney

Division of Engineering and Applied Sciences
California Institute of Technology
1995

This work was supported by the Applied Hydrodynamics Research Program administered by the Office of Naval Research under Contract Numbers N-00014-91-J-1295 and N-00014-92-J-1189, technical monitor J. Fein.

Approved for public release; distribution unlimited.

Report No. Eng. 200.32
May 1995

Approved by:
A. J. Acosta

A Study of Tip Vortices and Cavitation on a Propeller in a Non-uniform Flow Field

Thesis by

Elizabeth Anne McKenney

In Partial Fulfillment of the Requirements
for the Degree of
Doctor of Philosophy

California Institute of Technology
Pasadena, California

1995

(Submitted May 23, 1995)

Accession For		
NTIS	CRA&I	<input checked="checked" type="checkbox"/>
DTIC	TAB	<input type="checkbox"/>
Unannounced		<input type="checkbox"/>
Justification		
By		
Distribution /		
Availability Codes		
Dist	Avail and/or Special	
A-1		

© 1995

Elizabeth Anne McKenney

All Rights Reserved

Acknowledgements

It is a common myth, particularly popular among those who have not (yet) completed a PhD, that the accomplishment of acquiring an advanced degree is unequivocal proof of a person's genius, independence, and general expertise. I set forth here the utter fallacy of this myth: This thesis, as well as the PhD degree to which it shall in part entitle me, is evidence only of the extent to which its author was willing and able to ask of and learn from those of greater experience, and of God's grace in providing the strength (and the supportive environment of colleagues, friends, and family) to see the work through to the end.

I owe a great deal to my advisors – Christopher Brennen and Allan Acosta, who guided me through the research presented in this thesis, as well as Erik Antonsson who supported me for the first two years at Caltech. My thesis defense committee provided many useful criticisms and helpful suggestions: Fred Raichlen, Tony Leonard, Melany Hunt, and Tim Colonius. I also would like to thank Joe Katz of The Johns Hopkins University and his graduate students for their technical assistance in the tip vortex studies.

The Thomas building staff has not only helped me with academic and administrative affairs over the past six years, but Jackie Beard, Dana Young, and Cecilia Lin have also taken the time to be my friends. In addition, Joe Fontana and Rich Eastvedt of the Keck shop, Rodney Rojas of the M. E. shop, and George Yamamoto of Central Engineering provided both manual and creative assistance during these experiments.

My fellow grad students over the years have made the time more bearable, as well as acting as colleagues in the learning process of research: Wen-Jean Hsueh, Yan Kuhn de Chizelle, Roberto Zenit, Garrett Reisman, and Carl Wassgren are only a few of many; Doug Hart and Dennis Moore in particular merit much of the credit for my having made it through graduate school successfully.

Finally, my friends and family have been an invaluable support structure over the years. Locally, I would like to mention Elizabeth Duxbury (who could have known the Caltech Housing Office would pair us up so well, six years ago?), Ernest Prabhakar, David Noble, Valerie Robinson, Sheila Wright, and the Calvary Worship Team and Summer Team who have all been essential to my spiritual and emotional well-being during this time. And in the far field, my parents and brothers (and their families) have been patient as well as supportive, and Peter Ragonesi and John and Catherine Daly have kept in touch over the miles and the years. You are all very dear to me – thank you!

Abstract

Unsteady lifting surface flows are important subjects for study, both for the purposes of improving propulsive or lifting efficiency and also for mitigating the destructive effects and noise caused by cavitation. Some progress may be made by selecting a simple type of unsteadiness for closer study. In the present work, this tactic was implemented in two ways: the operation of a propeller at an angle of yaw to the freestream and the pitching oscillation of a finite-span hydrofoil.

A new facility was designed and constructed to set a propeller at an angle of yaw to the freestream, creating a fairly simple non-uniformity in the propeller inflow. Tip vortex cavitation inception measurements were made for a range of yaw angles and freestream velocities, and photographs of the cavitation were taken to illustrate the effects of the yaw angle.

The unsteady tip vortex flow field was measured on an oscillating finite aspect ratio hydrofoil using Particle Image Velocimetry (PIV), revealing how the circulation varied during a typical oscillation cycle. The results were compared with unsteady infinite-span theory, and also with recent measurements using LDV techniques on the same foil.

The hydrofoil was also the focus of a study of surface cavitation. High-speed motion pictures of the cavitation cycle helped to separate the process into its component stages, and variations with cavitation number and reduced frequency of oscillation were observed. The acoustic signals generated by the cavity collapse were correlated with the motion pictures, providing insights into the correspondence between the flow structures involved in the cavity collapse process and the sound generated by them.

The results from these studies provide valuable insights into the effects of unsteadiness in lifting surface flows.

Contents

Acknowledgements	iii
Abstract	iv
Nomenclature	xi
1 Introduction	1
1.1 Propeller Flows	1
1.2 Tip Vortex Flows	4
1.3 Cavitation	10
1.4 Project Overview	13
2 Experimental Facilities	19
2.1 Low Turbulence Water Tunnel	19
2.2 Yawed Propeller Apparatus	19
2.3 Oscillating Foil Apparatus	20
2.4 PIV Data Acquisition	21
2.4.1 Pulsed Laser Sheet	25
2.4.2 PIV Photographic System	26
2.5 Cavitation Data Acquisition	28
2.5.1 Photographic Methods	28
2.5.2 Acoustic Measurements	29
3 Yawed Propeller Experiments	40
3.1 Experimental Procedures	40
3.2 Cavitation Observations	41
3.3 Cavitation Inception Results	44

4	Tip Vortex Studies	52
4.1	Current Experiments	52
4.2	Unsteady Vortex Characteristics	54
4.3	Unsteady Circulation Results	57
5	Cloud Cavitation	80
5.1	Cavitation Cycle	80
5.2	Cavitation Acoustics	86
6	Conclusions	104
6.1	Yawed Propeller Experiments	104
6.2	Unsteady Hydrofoil Tip Vortex	105
6.3	Surface Cavitation Studies	107
A	Appendix: Propeller Facility	117
A.1	Propeller Specifications	117
A.2	Propeller Timing Unit	118
A.3	Facility Design	119
A.4	Propeller Disassembly Instructions	120

List of Figures

1.1	This container ship propeller has a diameter of 8.5 meters, weighs 70 tons, and absorbs 42.5 MW at 94 RPM. From Patience (1991).	15
1.2	Typical wake velocity field from the hull of a large ship. Contours are fraction of hull speed, flow is out of the paper. From Sharma, <i>et al.</i> , (1990).	16
1.3	Theoretical vortex flow field, from Katz and Plotkin (1991).	17
1.4	Photograph of vortex wake behind the oscillating hydrofoil, from Hart (1993). The vortices are made visible by air injection into the core region.	18
2.1	Caltech Low Turbulence Water Tunnel facility.	31
2.2	Propeller installed in the LTWT test section.	32
2.3	Oscillating hydrofoil in the water tunnel test section.	33
2.4	Particle Image Velocimetry setup.	34
2.5	Particle injection system for the oscillating hydrofoil.	35
2.6	Sensitivity vs. wavelength charts for Kodak films.	36
2.7	Portion of PIV image showing optical aberrations.	37
2.8	Movie camera LED trigger circuit timing.	38
2.9	Comparison of acoustic signals from two methods. Top signal is taken from flush-mounted transducer within the test section, bottom signal is from hydrophone enclosed in lucite box outside test section.	39
3.1	Geometry and notation for $\beta = 0^\circ$.	46
3.2	Geometry and notation for $\beta \neq 0^\circ$.	47
3.3	Variation in quasi-static blade loading with blade position (2D).	48

3.4	Types of cavitation observed near inception.	49
3.5	Photograph(s) of tip vortex cavitation. $\beta = 0^\circ, 10^\circ, 20^\circ$; $\sigma_T = 0.6$, $J = 0.4$	50
3.6	Tip vortex cavitation inception number σ_T as a function of advance ratio $J = \frac{U}{nd}$, for different values of β	51
4.1	PIV image showing tip vortex on foil; $k = 0.48$, $\phi = 180^\circ$	62
4.2	Filtered PIV image; $k = 0.48$, $\phi = 180^\circ$	63
4.3	Vector map calculated from same image; $k = 0.48$, $\phi = 180^\circ$	64
4.4	Comparison of spanwise velocity components, present data and data from Hart (1993); $k = 0.48$, $\phi = 180^\circ$	65
4.5	PIV image showing secondary flow; $k = 0$, $\phi = 0^\circ$	66
4.6	Change in vortex core diameter with phase angle; $k = 0, 0.48, 0.96$. . .	67
4.7	Comparison of two methods of measuring vortex core diameter; $k = 0.48$. (Phase angles of V_{max} results are artificially offset to the right for clarity.)	68
4.8	Change in vortex distance from trailing edge; $k = 0, 0.48, 0.96$. . .	69
4.9	Example of interactive contour; $k = 0.48$, $\phi = 180^\circ$. (Note that axis scales are unequal.)	70
4.10	Contours used for circulation profile; $k = 0.48$, $\phi = 180^\circ$. (Note that axis scales are unequal.)	71
4.11	Circulation profile; $k = 0.48$, $\phi = 180^\circ$. $A^* = \frac{\pi}{4}(d/D)^2$	72
4.12	Data plotted as V vs. R . Curve is best fit to $V = C/r$; $k =$ 0.48 , $\phi = 180^\circ$	73
4.13	Comparison of contour integral and curve fit methods; $k = 0.48$. .	74
4.14	Circulation vs. phase angle, compared with 2D calculations; $k = 0.48$. .	75
4.15	Circulation vs. phase angle, compared with Hart (1993) results; $k = 0.48$	76
4.16	Circulation vs. phase angle, compared with 2D calculations; $k = 0.96$	77

4.17 Circulation vs. phase angle, compared with Hart (1993) results; $k = 0.96$	78
4.18 Circulation vs. phase angle; $k = 0.0, 0.48, 0.96$	79
5.1 Cavity size plotted against phase angle, for reduced frequency $k =$ 0.73 and cavitation number $\sigma = 1.34$	92
5.2 Schematic representation of selected events in a typical cavitation cycle. See next figure for photographs.	93
5.3 Photographs of selected events in the cavitation cycle.	94
5.4 Schematic of starting and leading-edge vortices, from Freymuth, <i>et</i> <i>al.</i> (1986b).	95
5.5 Formation of MAXP distortion—Sketch from Bark (1985) and pho- tograph from current experiments.	96
5.6 Cavity area plotted against phase angle, for reduced frequency $k = 0.74$ and four cavitation numbers. ($\square \sigma = 1.53$, $\square \sigma =$ 1.34 , $\diamond \sigma = 1.15$, $\diamond \sigma = 0.88$)	97
5.7 Phase angles of selected events in cavitation cycle, for reduced fre- quency $k = 0.74$ and four cavitation numbers. ($\square \sigma = 1.53$, $\square \sigma =$ 1.34 , $\diamond \sigma = 1.15$, $\diamond \sigma = 0.88$)	98
5.8 Cavity size plotted against phase angle, for cavitation number $\sigma =$ 1.15 and two reduced frequencies. ($\diamond \triangle k = 0.56$, $\diamond \triangle k = 0.74$)	99
5.9 Raw acoustic signal from hydrophone, for one cycle with cavitation number $\sigma = 1.15$ and reduced frequency $k = 0.74$	100
5.10 Plot of filtered acoustic signal, with cavity size and foil angle curves.	101
5.11 Changes in acoustic intensity, p_A^* , with reduced frequency for three cavitation numbers. ($\triangle \sigma = 1.45$, $\square \sigma = 1.16$, $\square \sigma = 0.85$)	102

5.12	Acoustic impulse magnitude ranges as a function of the maximum bubble or cloud volume, from Reisman, <i>et al.</i> (1994). (a) Rayleigh-Plesset spherical bubble model for the same conditions as (b) and (c); (b) single travelling bubble cavitation from Kuhn de Chizelle, <i>et al.</i> (1994); (c) cloud cavitation results from Reisman, <i>et al.</i> (1994).	103
A.1	Propeller and Gearcase.	122
A.2	Yawed propeller assembly, outside test section.	123
A.3	Blade section notation.	124
A.4	Propeller blade measurements.	125
A.5	Encoder circuit schematic.	126
A.6	Frequency display circuit schematic.	127
A.7	Propeller apparatus drawings.	128

Nomenclature

General

ν = Fluid kinematic viscosity, m^2/s

p = Test section ambient pressure, Pa

p_v = Vapor pressure of water (room temperature), Pa

ρ = Fluid density, kg/m^3

\vec{u} = Local velocity vector, m/s

U_∞ = Tunnel test section velocity, m/s

Propeller

α_{eff} = Effective angle of attack of blade element, degrees

α_0 = Geometric angle of attack of blade element, degrees

β = Yaw angle of propeller, defined in right-hand sense with respect to upward pointing rotation vector, degrees

d = Diameter of propeller = 0.2159 m

n = Propeller rotation speed, cps

J = Advance ratio, $U_\infty/n \cdot d$

ϕ = Blade position (measured from top dead center), degrees

Φ = Propeller pitch, m

R_o = Radius of propeller = 0.108 m

S = Slip ratio = $1 - \frac{U_\infty}{n\Phi}$

σ_T = Cavitation number based on tip speed = $(p - p_v)/\frac{1}{2}\rho u_T^2$

u_T = Blade tip speed = $\omega d/2$

U_{eff} = Effective inflow velocity of blade, m/s

ω = Propeller rotation frequency, rad/s

Hydrofoil

α = Instantaneous angle of attack of foil, degrees

$\bar{\alpha}$ = Average angle of attack of foil, degrees

$\Delta\alpha$ = Amplitude of foil oscillation, degrees

c = Chord length, m

d_p = Particle diameter, m

Γ = Circulation, m^2/s

k = Reduced frequency = $\omega c/2U$

p_A^* = Dimensionless acoustic intensity

ϕ = Phase angle, degrees

\mathcal{R} = Distance from noise source to hydrophone, m

ρ_p = Particle density, kg/m^3

σ = Cavitation number based on $U_\infty = (p - p_v)/\frac{1}{2}\rho U_\infty$

σ_i = Cavitation inception number

ω = Forced frequency of foil oscillation, rad/s

ω_n = Cavity natural shedding frequency, rad/s

u = Local streamwise velocity component, m/s

v = Local spanwise velocity component, m/s

Chapter 1 Introduction

A marine propeller is one of many common examples of unsteady lifting surface flows, among others such as airplane wings, sailboat keels, fish fins, and helicopter blades. These flows are important subjects for study, both for the purposes of improving propulsive or lifting efficiency and also for mitigating the destructive effects and noise caused by cavitation. The inherent complexity of a fully unsteady three-dimensional flow, however, makes a complete understanding very difficult to achieve. Experiments can provide many insights, but they are limited by our inability to model the true flow with a great degree of accuracy.

Some progress may be made by selecting a simple type of unsteadiness for closer study. In the present work, this tactic was implemented in two ways: the operation of a propeller at an angle of yaw to the freestream and the pitching oscillation of a finite-span hydrofoil.

1.1 Propeller Flows

Every marine propeller in a real application suffers from some degree of flow non-uniformity in the water in which it operates. The hull of the ship creates a complicated wake flow just upstream of the propeller, and this wake may be disturbed further by transient effects such as ship maneuvers. This is coupled with interactions between the propeller flow and the hull boundary layer, resulting in a very complicated flow field—one on which efficient operation of the propeller depends heavily, yet which remains at present beyond the capabilities of current analysis and modelling techniques to predict. At the same time, however, it is also a very rich source of interesting simpler flows that are well worth investigating, and which may help in the long run to shed some light on the larger problem.

Each blade of a propeller is a lifting surface much like an airplane wing, generating lift by virtue of its shape, its orientation, and its motion relative to the surrounding fluid. Figure 1.1 shows a propeller designed for a large container ship. As the propeller rotates, part of the lift force on each blade contributes to the total thrust of the propeller; the remainder imparts angular momentum to the fluid which must be overcome by the torque produced by the motor.

As in the case of the wing, the lift on each blade will be a function of the speed of the flow approaching its leading edge, as well as its angle of attack with respect to that flow. Since the hull of the ship creates a highly irregular flow around the propeller, not only the speed but the angle of the inflow to a given blade will change as it rotates through different regions of the wake, and in fact they will vary along the span of the blade as well. This will produce corresponding variations in the lift on the blade, which may produce undesirable vibrations in the flow field that could resonate with the hull or fatigue the blade material. Figure 1.2 shows a typical wake velocity field from a large ship. Another undesirable effect is that, even if conditions in the ambient flow are not conducive to cavitation inception, the varying inflow may cause such conditions to exist momentarily on the blade, resulting in intermittent or early cavitation. In most cases, this nonuniformity is unsteady and very complex in its structure, as illustrated in the studies by English (1992) of the propeller-hull vortex interaction. The severe difficulties inherent in the investigation and explication of the problem are, of course, merely considered a challenge to today's researchers, armed with 1990's computer technology. But they are also "standing upon the shoulders of giants"¹—decades of work by previous theorists who have paved the way. Kerwin (1986) offers a good survey of this history, from which the following comments are derived:

Betz (1919) is generally hailed as one of the first to develop a clear theoretical treatment of a propeller with a uniform inflow. He concluded that if a propeller had blades with the optimum circulation distribution, it would generate in its wake

¹Sir Isaac Newton, 1642–1727

a helical vortex system moving downstream at a constant velocity. The potential problem set up by Betz was later solved by Goldstein (1929). In the meantime, Prandtl (1921) was inspired by the vortex system idea to adapt lifting-line theory to study propeller blade hydrodynamics. This method proved fairly useful for aircraft propellers but failed to address the problems of marine propellers such as cavitation and the lack of a uniform inflow. Lerbs (1952) later extended Prandtl's theory to include a radially varying inflow velocity distribution. For the most part, however, researchers and designers dealt with the discrepancies between propeller theory and marine applications by developing an extensive system of empirical correction factors. This remained the most practical propeller design method until the advent of digital computer technology began to make such techniques obsolete. Sparenberg (1959) developed a lifting surface theory that quickly became very popular in computational algorithms, although lifting-line theory is still widely used. Brockett (1981) and Greeley and Kerwin (1982) developed full three-dimensional codes for propeller design, incorporating all the major aspects of the propeller design problem but neglecting the propeller hub. Wang (1985) then published an analysis which included the hub as well.

But, as pointed out by Kerwin (1986), the real test of a theory or numerical solution is not how neat the answers look but how closely they can be shown to model actual propeller flows. The major obstacle to comparing experimental results to calculations is that the precise non-uniform and time-varying inflow velocity distribution is unknown. A number of studies have attempted to simulate various experimentally measured wake distributions. Chapter 7 of the ITTC Cavitation Committee Report (1993) contains an excellent summary of recent work in this area.

Simulating a wake distribution, whether at model or full scale, is a difficult task. One approach to studying the effects of such nonuniformity is to break down the problem into smaller pieces which can be more readily understood and, perhaps, solved analytically. These solutions could then be compared with exper-

imental results in order to build a qualitative understanding of the problem as well as a quantitative one. For example, one of the simplest variations in inflow is the strictly sinusoidal one generated by setting the propeller axis of rotation at some angle of yaw to the freestream, such as a propeller might experience temporarily when the ship makes a turn. One of the present studies involves an examination of the characteristics of a yawed propeller mounted in a water tunnel. This causes a periodic fluctuation in the inflow to each blade as it makes one full revolution. It varies the magnitude of the incoming velocity vector to the blade section, as well as changing the direction of that velocity—altering the effective angle of attack of the blade section. Since lift is a function of both the effective angle of attack and the incoming flow magnitude, this yaw angle in the propeller's heading introduces a periodic fluctuation in the lift, or loading of the blade, which is fairly straightforward to discuss theoretically or model numerically. There are also more subtle consequences of the unsteady inflow, most notably the potential for creating cavitating conditions on the propeller blades or in the tip vortices, one of the consequences examined in this thesis.

The yawed propeller apparatus described in this work was designed and built to study a variety of aspects of this flow. Information about the influence of yaw angle on propeller cavitation characteristics, both on the blade and in the tip vortex region, was obtained from the apparatus. The unsteady tip vortex flow was also studied in detail, to gain insight into tip vortex cavitation inception as well as to provide indirect measurements of the unsteady blade loading.

1.2 Tip Vortex Flows

One of the notable features of the propeller wake is the helical vortex structure formed by the blade tip vortices. Tip vortices occur at the ends of lifting surfaces where the higher-pressure flow leaks around to the lower-pressure region on the suction side, rolling up the bound vortex sheet into a flow structure attached to

the tip of the leading edge and extending far into the wake. The leakage flow introduces spanwise velocity components on both sides of the lifting surface, and a downwash component is produced in the wake by the vortex flow at the tip; these effects may act to decrease significantly the lift force on a surface with low aspect ratio such as a marine propeller blade.

The vortex flow continues to be of interest even downstream of the lifting surface that created it. When tip vortices occur on the wings of large aircraft, they can become a hazard to smaller craft following too closely. When they occur on helicopter blades, they reduce the lift of the following blade which must experience a reduced inflow. On a marine propeller the effects on the wake flow field are not as much a concern as is the occurrence of cavitation in the vortex cores, creating noise and possibly leading to erosive blade cavitation. The nature of the vortex velocity distribution is such that the lowest pressure occurs in the vortex core, so the core then becomes the most likely place for cavitation inception. Modern theory describes the two-dimensional cross-section of an isolated vortex flow as consisting of two concentric regions of purely tangential flow. The inner core region acts in solid body rotation, so the velocity profile is $v_\theta(r) = \omega_y r$ where ω_y is the vorticity normal to the cross-sectional plane. The outer region, where viscous dissipation of the vorticity occurs, has a velocity profile that drops off as $v_\theta(r) = \Gamma/2\pi r$. Both regions are illustrated in Figure 1.3, taken from Katz and Plotkin (1991).

Another reason for studying tip vortices is that, since they are formed by the same pressure imbalance that gives a wing its lift, examining the characteristics of this vortex can be a useful means for understanding both steady and unsteady forces that the blade (and thus the propeller) may be experiencing, providing information which might be difficult to measure directly. This is particularly true in the case of propeller tip vortices, where the installation of force measuring devices may be inconvenient if not highly impractical, and a non-intrusive method of measuring the flow is desired. These indirect measurements can also be used

to validate computational models of similar flows. The current work uses Particle Image Velocimetry (PIV) to examine the tip vortex flow on an oscillating hydrofoil, with the longer-range goal of looking directly at the propeller tip vortices.

Given all the applications that involve tip vortices, it is no surprise that these flows have been a popular topic in fluid mechanics research for many decades. Work in the earlier part of this century focussed on developing mathematical treatments of airfoil wakes including tip vortices. In the early 1930's Betz (1933) applied the Kutta-Joukowski theorem ($Lift = \rho UT$) to airfoils, and developed a number of formulae dealing with plane vortex systems (i.e., all vortex filaments are straight and parallel). It was also known that an airfoil in a starting flow sheds a spanwise vortex, of equal strength and opposite sign to the "bound" vortex which gives the wing its lift. By Helmholtz' law, neither of these vortices can end abruptly in the fluid, but must be interconnected or end at a boundary. In the case of the airfoil, these two vortices are joined by trailing vortices from each wingtip to form a rectangular vortex ring. Sears (1938) developed a mathematical expression for the impulse of this "closed, plane vortex element," based on theory developed originally by Theodorsen (1935) and presented in more accessible form by von Kármán and Sears (1938). A decade later, Spreiter and Sacks (1951) published a theoretical study of how the trailing vortex sheet initially rolls up into these two wingtip vortices. Their paper included photographs of flow visualization studies showing this process, looking at cross-sections of the wake between the trailing edge of the wing and about 2 chords downstream of the trailing edge. These photographs clearly demonstrate the tip vortex rollup as well as the downwash effect of the velocities induced by the vortices, and there is even some evidence of the vortex sheet itself breaking up into small discrete streamwise vortices in between the larger tip vortices. McCormick (1962) studied the rollup of the trailing vortex sheet and concluded that the characteristics of the tip vortex seem to depend heavily on the thickness of the pressure-side boundary layer.

In a numerical work, Moore (1974) examined a finite vortex sheet composed

of point vortex elements, and calculated how this structure rolls up with time due to mutual induced velocities; the results show a "marked ellipticity" to the vortex spiral when rollup is nearly complete. Measurements by El-Ramly and Rainbird (1977) showed that less than 80% of the root circulation had rolled up into the tip vortex by 13 chord-lengths downstream of the trailing edge, and the authors also noted that the vortex system was completely contained within the viscous wake of the wing.

Freymuth and his colleagues (1984, 1985, 1986a, 1986b, 1987, 1988a, 1988b, 1989) published a series of papers which visualized the full three-dimensional vortex system generated by a wing in a starting flow of constant acceleration. By painting the wing with titanium tetrachloride before the experiment, they were able to tag specifically the fluid in the boundary layer, thus tracing the wake vorticity from its source to the complicated structure that formed behind the wing. In particular, they were able to visualize the leading edge, or "bound" vortex as well as the starting vortex, and their photographs clearly show these two spanwise vortices joining at the tips of the leading edge to form a continuous vortex loop. It is also easy to discern the shed vorticity between these two larger vortices—the spanwise vortices of the vortex sheet shed by the trailing edge are not only distinctly visible but also interact with the tip vortices in a complex pattern.

While the Freymuth studies gave an excellent overview of the vortex system on the foil, the details of the vortex formation were too small to be discerned in their photographs. The studies by Francis and Katz (1988) and Katz and Bueno Galdo (1989) examined the finer details of the tip flow on a hydrofoil in steady flow by seeding the freestream with dye and viewing cross-sections by means of a laser sheet normal to the flow. Both of these papers present detailed views of the development of the tip vortex alongside the foil, noting that there are actually several secondary vortices which form along with the main tip vortex and interact with it, and eventually are entrained into it somewhere downstream

of the trailing edge. Francis and Katz (1988) examined the variations in the tip vortex flow with Reynolds number and with incidence angle, and developed empirical relations which reflect their data. Katz and Bueno Galdo (1989) looked at the effect of painting the foil surface with roughness elements of various sizes, and found that increasing the surface roughness seems to reduce the tip vortex strength. Stinebring, *et al.* (1989) used Laser Doppler Velocimetry (LDV) to measure the tip vortex structure, including the axial velocities, and discovered that the peak axial velocity did not coincide with the center of the vortex, resulting in a very unstable flow. They also proposed that a rough estimate of the core mean pressure could be calculated by using the radial equilibrium equation

$$\frac{dp}{dr} = \frac{\rho V_T^2}{r}, \quad (1.1)$$

where V_T is the tangential velocity. Green and Acosta (1991) used double-pulsed holography to track the instantaneous tangential and axial velocities in the vortex. Their results show that, near the trailing edge, the axial flow in the center of the vortex exceeded the freestream velocity. It also was observed to be highly unsteady, with fluctuations as high as the freestream velocity at times; when these fluctuations were sufficiently large and sudden, vortex kinking could occur.

Studies by Shekarritz, *et al.* (1991, 1992, 1993), and Pogozielski, *et al.* (1993) used Particle Image Velocimetry (PIV) to examine the tip vortex on a foil, as well as the junction vortex that formed where the foil connected to the axisymmetric body that carried it. They found that the circulation of the tip vortex remained fairly constant for several chord lengths downstream of the foil, and that the circulation within the vortex varied with the square of the radius within the core. Measurements of the vortex axial velocity showed that its variations seemed to coincide with the presence the secondary vortices such as those just mentioned above. It is also significant to note that their study of the tip vortex rollup concludes that the rollup process is “nearly complete at the trailing edge” but

that the circulation at that point is less than 66% of the root circulation.

All of these studies just mentioned focus on tip vortices in steady flow. The current work is concerned with the effect of unsteadiness on the tip vortex characteristics, particularly as it applies to the propeller operating in unsteady conditions.

Lawrence and Gerber (1952) presented a theoretical treatment of the effects of oscillation (both heaving and pitching motions) on the average lift and moment forces on a low aspect ratio wing. Their results are important for aerodynamic applications, where the emphasis is on determining the ability of the wing to support an aircraft, but are of less use in the context of avoiding (or at least predicting) transient cavitation conditions on a marine propeller. For the latter problem, it is necessary to know specifically how the lift varies with the periodic flow conditions, not merely the average effects of the motion.

Most research on the structure of unsteady wakes, as reviewed by McCroskey (1982), has focussed on the spanwise shedding of vortices without any discussion of the tip vortex. A few studies since then, such as Gad-el-Hak and Ho (1986) and Freymuth (1988a) have visualized the three-dimensional vortex system on a pitching foil; the amplitude of the oscillations was sufficiently large to cause separated flow conditions. While the photographs of these vortex systems are dramatic in their exposition of the complexity of the wake vortex interaction, such extreme changes in incidence angle are less relevant to the types of unsteady flow that might be expected to occur on a propeller blade. Recently, McKenney and Hart (1993) used LDV techniques to survey the wake flow very near the trailing edge of a pitching hydrofoil, and determined from these velocity measurements the changes in both spanwise and streamwise circulation with the phase of the foil. Finally, Hart (1993) conducted an extensive survey of the wake of an oscillating finite aspect ratio hydrofoil, using flow visualization techniques as well as LDV to analyze the wake structure. Figure 1.4 illustrates the complex vortex structure of the wake flow behind the oscillating hydrofoil. His results concur with much of

the two-dimensional research on similar flows, and also provide insight into the variation in circulation on the oscillating foil based on velocity changes measured at the trailing edge.

The propeller facility designed for the current work can be used to study several specific regions of the flow field, including the blade tip vortices, using Particle Image Velocimetry (PIV). As an initial test of the PIV setup, and as a followup to the hydrofoil wake studies by Hart (1993) using LDV, the research presented here includes a PIV study of the tip vortex on the same oscillating hydrofoil. The results, discussed in Chapter 4, indicate how the circulation varies with the foil oscillation, and are compared to theoretical studies as well as with the results reported by Hart.

1.3 Cavitation

Another possible consequence of foil oscillation is the formation of transient surface cavitation on the hydrofoil. This is an important phenomenon of interest in propeller research, for a variety of reasons. Cavitation occurs when the local pressure in a liquid falls below the vapor pressure of the liquid, forming pockets, or cavities, of vapor within the liquid. The cavities themselves can mar a propeller's performance by altering the flow around the blade, but equally serious is the force with which they collapse—the pressures required to create the cavities are extremely low, and thus cavitation tends to collapse with great violence, usually generating a great deal of noise and possibly causing damage to nearby surfaces, particularly the propeller.

In many applications, cavitation tends to occur first within the core of the tip vortex. The region of greater concern, however, is on the blade itself where cavitation begins along the leading edge and may grow to cover the entire suction side (face) of the blade in extreme cases. Clearly in such cases the density change within the cavity will affect the lift generated by the blade; this not only

changes the overall thrust the propeller can produce but also may create undesirable vibrations due to unsteady loading. In addition, the violence of the collapsing cavitation may generate a great deal of noise in operation as well as damaging the propeller over time.

Cavitation research up to the 1940's was seeking primarily to minimize the erosive effects and thrust losses caused by heavy sheet and cloud cavitation, which tends to occur at relatively high speeds. It was not until the development of the submarine which, in the words of Strasberg (1977), "turned out to be an unusually useful test vehicle for studying propeller noise" that it was noticed that noise from cavitation could occur at much lower speeds than cavitation was previously thought to occur (as little as 2.5 knots, near the surface), and tip vortex cavitation was discovered.

Two recent reviews, Fruman (1994) and Arndt and Maines (1994) discuss many of the notable research developments on the subject of tip vortex cavitation. A number tip vortex studies, both with and without cavitation, cite McCormick (1962) as the seminal work from which they evolved. McCormick studied the rollup of the trailing vortex sheet with an eye to relating the formation of the tip vortex to the inception of cavitation in the vortex core. From his cavitation observations, he developed empirical relations for the cavitation inception number based on incidence angle and Reynolds number. Several other research projects have made progress in observing the details of the tip vortex inception process (Arndt, *et al.* (1986), Arndt and Dugue (1992), Maines and Arndt (1993a), Maines and Arndt (1993b), Green (1988), and Hart (1993)) as well as developing numerical schemes to describe it (Yongsong (1986) and Hsu (1991)), but the capricious nature of cavitation inception continues to defy reliable prediction. Hart (1993) made a notable contribution, however, in observing the non-monotonic behavior of tip vortex inception with reduced frequency of oscillation.

Attached cavitation occurring on lifting surfaces has received a great deal of attention due to its detrimental characteristics, such as erosion damage to the sur-

face and the generation of noise. Knapp (1955) was one of the earliest researchers to describe the cavitation growth and collapse process in detail. Later studies have considered the causes and character of the inception of such cavitation, the mechanisms which cause the most severe erosion, and the correlation of the flow mechanisms with the noise produced when they collapse.

Strasberg (1977) gives a brief history of research results concerning propeller cavitation noise. He notes the abrupt increase in propeller operation noise that accompanies the inception of cavitation, even when the cavitation only occurs in the tip vortex region. Noordzij and van Oossanen (1977) describe tip vortex cavitation as being the least noisy type of cavitation, with "bubble" cavitation being the most noisy. Sharma, *et al.* (1990) also found this to be true. In particular, they observed that when the propeller operated in the unsteady wake flow of the ship, tip vortex cavitation was no longer the dominant type of cavitation on the propeller. With the non-uniform inflow, attached cavitation became dominant, and included cloud-like formations; at the same time, the noise was observed to increase significantly.

Research on hydrofoils, under both steady and oscillating conditions, has confirmed these results. Details of the surface cavitation dynamics will be discussed in Chapter 5, but here is a brief synopsis: Travelling bubbles near the leading edge appear to coalesce and form a single sheet cavity attached to the leading edge across most or all of the span; this cavity then collapses into a froth of tiny bubbles and the remains are convected downstream. Of particular note is that, as the attached cavity collapses and is shed into the wake, the breakup of the cavity often results in the occurrence of cloud cavitation, distinct clouds of very small bubbles which persist long after the sheet cavity has dissipated. The structure of such clouds appears to contain strong vortices, possibly formed by the shear layer at the surface of the collapsing cavity (Avellan, *et al.* (1988); Kubota, *et al.* (1989); Maeda, *et al.* (1991); Yamaguchi, *et al.* (1991)). These clouds then collapse with some violence, often causing severe erosion on the surface and gener-

ating significant amounts of noise (Knapp (1955); Bark and van Berlekom (1978); Kato (1985); Ye, *et al.* (1989); Soyama, *et al.* (1992)).

Much of the cloud cavitation research has been concerned primarily with stationary foil sections in a constant freestream, and the intermittent nature of the cavity collapse process has made this a difficult and interesting problem. Consideration has also been given, however, to the effect of an unsteady flow environment as well as the effects of finite span (Shen and Peterson (1978), (1980); Franc and Michel (1988); Hart, *et al.* (1990); Kato, *et al.* (1992)). In particular, Stern (1989) studied the cavity dynamics on an oscillating hydrofoil and discovered a dependence on the ratio of the sheet cavity's natural shedding frequency (ω_n) to the forcing frequency of oscillation (ω). In examining fluctuations in the length of the attached cavity, for example, he found that for large values of ω_n/ω there was little effect on the cavity shedding frequency; if the ratio was small, however, the cavity shedding process seemed to follow the foil oscillation frequency fairly closely, with variations in length corresponding to the changes in incidence angle but with the maximum size of the cavity reduced from the steady-state case. For values of the frequency ratio close to 1, the changes in cavity size also followed the foil oscillation, but the maximum size of the cavity was significantly larger than the steady-state value. Hart (1993) noted differences not only in the cavitation process depending on this ratio (including a phase lag between the maximum cavity size and the maximum foil angle) but also in the sound produced by the cavitation. He observed that for oscillation frequencies close to the cavity natural shedding frequency the noise produced by the cavitation increased significantly. Chapter 5 will discuss quantitative results concerning this phenomenon.

1.4 Project Overview

This project was developed in response to certain expressed needs and goals of naval architects. Of particular concern at the present time is preventing or min-

imizing cavitation noise during maneuvers, either in making normal course corrections or in sudden defensive tactics. Since the propeller inflow may change significantly when the craft changes direction, it is quite possible that the blade tip may encounter transient conditions favorable for cavitation inception.

Current methods of predicting tip vortex cavitation inception (both experimental and CFD) are considered unsatisfactory because they depend on certain functions of the water condition and the precise blade flow that are known only empirically and for limited cases. In the same way, prediction of cavitation inception during maneuvers is also not considered practicable using current techniques, since present experimental models are only approximate and the few numerical attempts on the problem have not yet been fully validated by experimental results. Suggestions for future research frequently stress developing a more detailed and/or accurate understanding of tip vortex flows, including cavitation inception and the transition process from tip vortex cavitation to leading edge or sheet cavitation.

The organization of the remainder of this thesis is as follows: The next chapter will describe in some detail the experimental techniques used in the current studies, as well as specifications for instrumentation specifically developed for this work. Chapter 3 discusses some preliminary observations of the effect of yaw on propeller tip vortex cavitation, using a new apparatus designed at Caltech for the experiments (the finer details of the apparatus itself will be left to the Appendix), and the following chapter shows results of PIV measurements of the tip vortex on the oscillating hydrofoil. Observations of surface and cloud cavitation on an oscillating hydrofoil will be described in Chapter 5. Finally, Chapter 6 will summarize the conclusions reached in this thesis.



Figure 1.1: This container ship propeller has a diameter of 8.5 meters, weighs 70 tons, and absorbs 42.5 MW at 94 RPM. From Patience (1991).

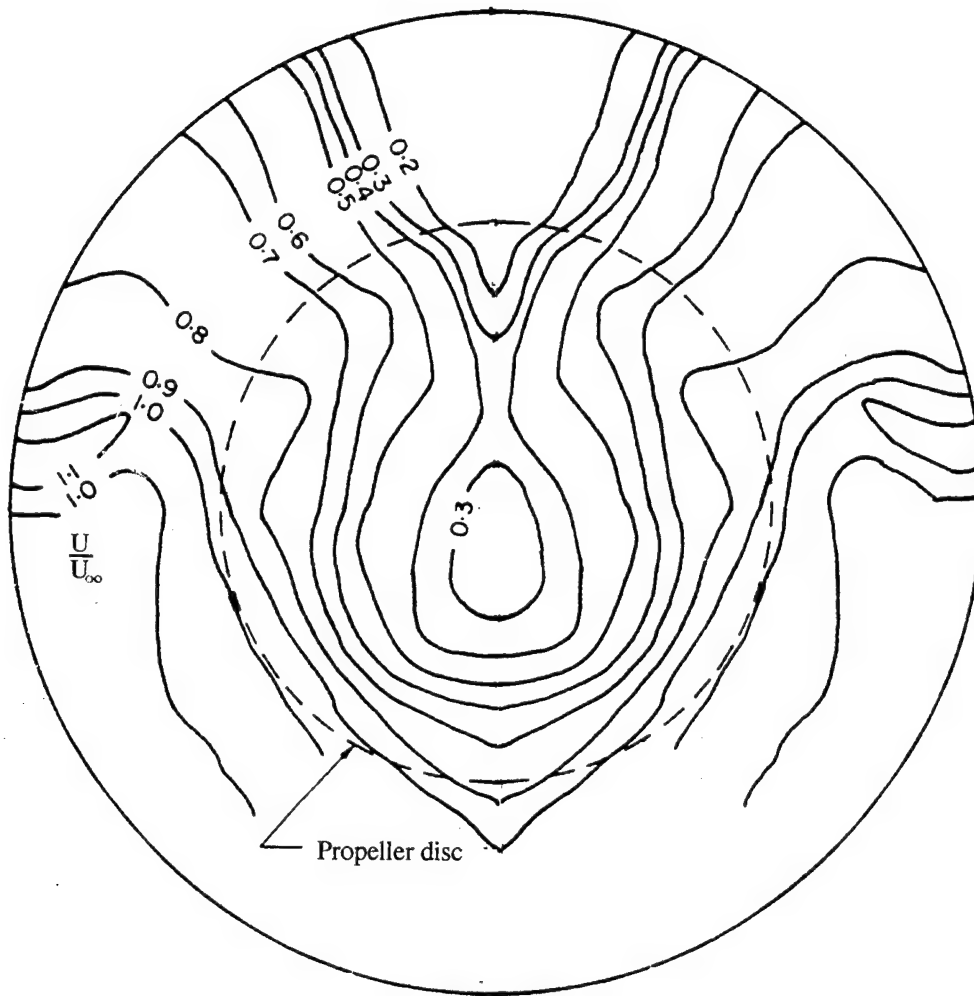


Figure 1.2: Typical wake velocity field from the hull of a large ship. Contours are fraction of hull speed, flow is out of the paper. From Sharma, *et al.*, (1990).

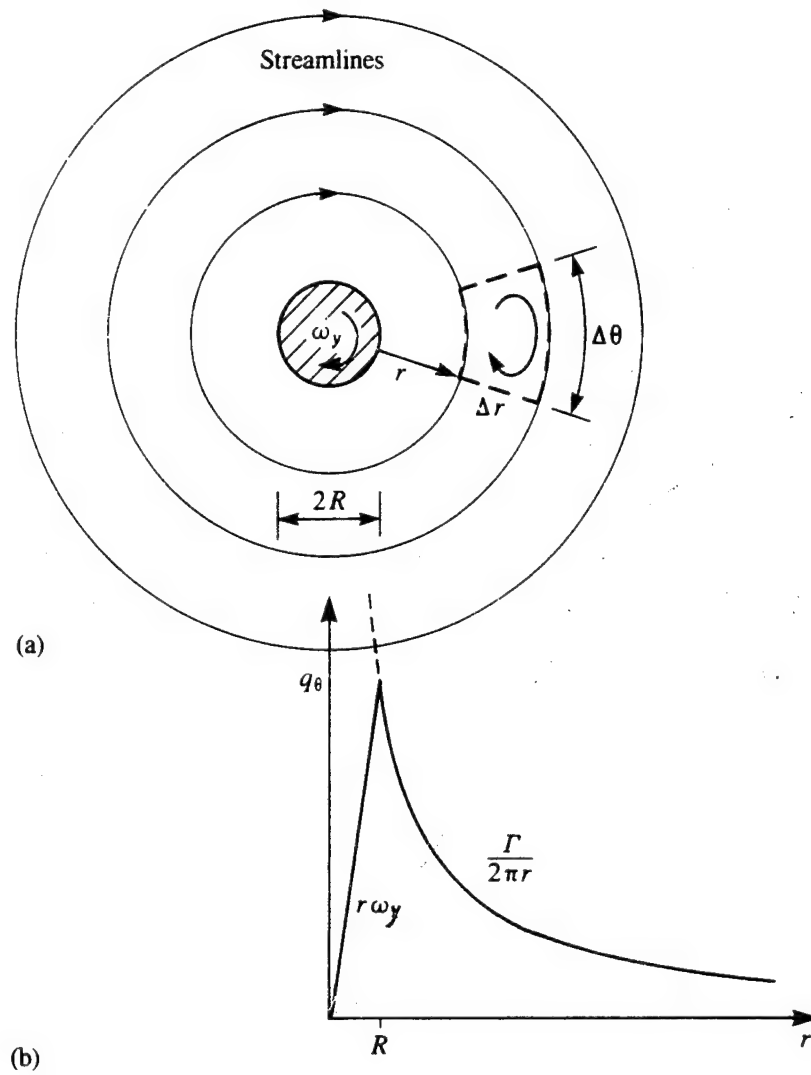


Figure 1.3: Theoretical vortex flow field, from Katz and Plotkin (1991).



Figure 1.4: Photograph of vortex wake behind the oscillating hydrofoil, from Hart (1993). The vortices are made visible by air injection into the core region.

Chapter 2 Experimental Facilities

2.1 Low Turbulence Water Tunnel

The Caltech Low Turbulence Water Tunnel (LTWT) is a closed-circuit facility, with a $30.5\text{cm} \times 30.5\text{cm} \times 2.5\text{m}$ test section and a 16:1 contraction ratio. A sketch of the facility is shown in Figure 2.1. It is capable of freestream velocities up to 10m/s and can support pressures down to 20kPa . It is equipped with a $5\mu\text{m}$ filter line, and a deaeration system capable of reducing the dissolved air content of the water to as little as 3ppm . The total air content (TAC) of the water in the tunnel was measured using a Van Slyke apparatus. To minimize corrosion of the various metal surfaces of the interior of the tunnel, the water is treated with sodium chromate and carefully pH-balanced. Gates (1977) provides a complete description of this facility.

2.2 Yawed Propeller Apparatus

A propeller drive unit was installed in the LTWT test section as shown in Figure 2.2. This apparatus provides a variety of functions to accommodate a range of experiments. The 8.5-inch diameter propeller is a commercial right-handed, three-bladed model. Both the propeller and its right-angle gearcase were obtained from the lower end of a Johnson 6-HP marine outboard motor; they are now driven by a 5-HP Baldor AC motor (controlled by a programmable inverter unit from Sabina Electric) located outside the test section. The motor is capable of speeds up to 3450 RPM; this corresponds to a propeller rotation speed of approximately 1550 RPM due to the gear ratio within the gearcase. (For the current study the propeller rotated at 1060 RPM.) The angle of the propeller with respect to the

freestream was set via a taper-lock bushing. It could be adjusted easily between experiments, allowing the propeller to be yawed up to 20° from the freestream direction.

A shaft encoder is geared to the drive shaft so that it matches the propeller gearcase ratio and provides electronic signals (1440 pulses/rev) to indicate the angular position and motion of the propeller blades. An electronic circuit was designed to process the encoder pulses and provide synchronization pulses at desired intervals (once per rotation or once per blade), useful for triggering other equipment such as strobe flashes or a computer data acquisition system. This unit also calculates and displays the rate of rotation of the propeller.

Details of the propeller apparatus and the associated electronics may be found in Appendix A.

2.3 Oscillating Foil Apparatus

In the current work, a NACA 64A309 hydrofoil was reflection-plane mounted in the test section, as shown in Figure 2.3 and described in Hart (1993). The hydrofoil has a rectangular planform with a chord of 15.2cm and a semi-span of 17.5cm ; it is made of stainless steel and polished to a smooth finish. It is connected to a 750 watt DC motor by a four-bar linkage such that it oscillates nearly sinusoidally in pitch about a point near the center of pressure, $0.38c$ from the leading edge ($c = \text{chord}$). A slip-collet connecting the oscillation linkage to a coupling shaft allows adjustment of the mean angle of attack. In addition, the linkage is adjustable for oscillation amplitudes ranging from $\pm 1^\circ$ to $\pm 5^\circ$. The oscillation frequency may be continuously varied from 0 to 50Hz. An optical shaft encoder mounted to the DC motor generates a digital signal (1024 pulses per revolution), providing an electronic means for determining the instantaneous angle of attack of the foil. A control unit (designed by Hart (1993)) uses the encoder pulses to generate a synchronization pulse at a selected angle; it also outputs a separate signal that

pulses every time the foil reaches zero degrees angle of attack (the "ZERO" pulse).

For the present experiment, the foil oscillated at 5 Hz and 10 Hz. Its mean angle of attack was 5° , and the oscillation amplitude was $\pm 5^\circ$, giving a range of 0° to 10° degrees in angle of attack during each cycle. The freestream velocity was kept constant at 5 m/s , thus the reduced frequencies for the experiment were $k = 0.48$ and 0.96 . Since each angle of attack between $\alpha = 0^\circ$ and $\alpha = 10^\circ$ is visited twice by the foil during a single oscillation cycle, discussions in this thesis concerning the foil will generally refer to "phase angle" rather than angle of attack: The phase angle, ϕ , is defined such that $\phi = 0^\circ$ represents $\alpha = 0^\circ$, $\phi = 180^\circ$ indicates $\alpha = 10^\circ$, and $\phi = 360^\circ$ means the foil has returned to $\alpha = 0^\circ$. Thus from $\phi = 0^\circ$ to $\phi = 180^\circ$ the angle of attack is increasing, and from $\phi = 180^\circ$ to $\phi = 360^\circ$ the angle of attack is decreasing.

2.4 PIV Data Acquisition

Particle Image Velocimetry (PIV) is a relatively new flow visualization method, one which provides quantitative as well as qualitative information about the flow. Adrian (1991) has recently written an detailed review of the specifics of implementing the various types of particle-imaging techniques and interpreting results. All of the methods that he discusses involve using flow tracers which are illuminated for a specific amount of time, and the velocity field is determined by examining a photographic record of the positions of the tracers during that time. The current experiments fall into the category of low-image-density PIV, or "particle-tracking velocimetry," where the flow tracers are sufficiently sparse that overlap of particle images is infrequent to rare. In the present case, a slice of the flow field is illuminated by three very short bursts of a pulsed laser sheet, and the flow is seeded with microscopic particles designed to fluoresce at the precise wavelength of the laser. During the laser pulses a still camera views the laser sheet with its shutter open, recording multiple images of each particle caught in the laser sheet. When

the resulting photograph is later analyzed, the spacing between the multiple images of a given particle will indicate the speed of the particle, and the change in its position describes the direction of motion.

For this technique to result in useful information about the flow, it must be possible to identify precisely the location of a given particle relative to the flow field of interest, as well as the physical distances that correspond to the spacings on the photograph. This can be accomplished by including some reference point in the field of view, such as a boundary or other object whose location can be determined without ambiguity, and by taking calibration photographs of some item of known size which will establish the exact scale of the images relative to the physical apparatus. Also, if the photographs are to be analyzed as digitized computer images, as is generally now the case, there must be some reliable method of distinguishing the actual particles from background noise in the image.

Given a photograph or digitized image and the appropriate scaling and position factors to locate the image in the overall flow field, there are two common ways of extracting the velocity information. One method is to break down the image into small sub-images, or "windows," and then to correlate each sub-image with itself at slightly changed positions. The result of this auto-correlation will be a statistical calculation of the most likely direction and speed of motion of the particles in that window; the algorithm is repeated over the entire image, often with overlapping sub-images which will produce a data set with higher spatial resolution. This technique works best with high-density flow fields, where each window contains a sufficient number of particles for an accurate statistical analysis (though not so many particles as to make them indistinguishable from one another).

The second commonly used analysis technique involves matching each particle image in the photograph with its multipulsed partners, and measuring the change in position between pulses. If the particle trains are sparse enough for an unambiguous identification, this can be done automatically with a computer.

If, however, the particle trains overlap to some extent, or if the flow field is not uniformly seeded, it may be necessary to identify them visually—that is, to use human judgement to select the particle images that belong to a given set, though it may still be left to the computer to calculate the displacements. This in turn can introduce errors into the data, of course: Since the particles will in general take up many pixels but must somehow be represented as occurring at a point location, and differences in lighting may cause the centroid of the particle image to appear slightly offset from the actual center of the particle. Errors in locating the position of the particle image will then lead to errors in the velocity magnitude and direction that are calculated from the assumed position.

A number of concerns need to be addressed in assessing the potential success of a given PIV setup:

1. The lenses and other optical components (including test section windows if applicable) should be free of optical aberrations, or at least such deviances should be minimized. This is probably the most difficult ideal to achieve, and is often neglected due to financial factors.
2. The particle density should be sufficient to map the desired region of the flow field, but not so dense that particles are difficult to distinguish, by computer or by human eye depending on the analysis method chosen.
3. The particle dynamics need to be considered, since the particles will not perfectly track the flow but will suffer some slight slip velocity that depends on the drag force on the particles. Adrian (1991) suggests the relation (using Stokes' law to evaluate C_D)

$$|v - u| = \rho_p d_p^2 |\dot{v}| / 36 \rho \nu, \quad (2.1)$$

For the current experiment, this velocity deficit evaluates to about 6 cm/s , or 1% of the freestream velocity.

4. The laser sheet thickness should be considered carefully. If the sheet is too thin, then the streamwise component of a particle's velocity may carry it through the laser sheet before the pulse sequence is complete, leaving more incomplete particle trains in the image. Adrian refers to this as the "probability of not being truncated,"

$$F_o(w\Delta t) = 1 - \frac{|w|\Delta t}{z_o}, \quad |w|\Delta t < z_o, \quad (2.2)$$

where w is the out-of-plane velocity component and z_o is the thickness of the laser sheet. For the present experiment this value is 0.8125, or over 80% probability that the particle image train for a given particle will be complete. If the laser sheet is too thick, the streamwise positions of the particles will become ambiguous, making it difficult to reconstruct the original flow location of the velocity vectors.

5. The use of the laser sheet to illuminate the flow will tend to bias the results towards particles of lower velocities (Willert and Gharib (1991)): Since the images only show particle movement in the plane of the laser sheet, particles moving more quickly in the freestream direction do not evidence any motion and thus provide no velocity information. This would include particles outside the vortex, as well as some in the very center of the core region (where the axial velocities can sometimes exceed the freestream velocity).
6. At small angles of attack the vortex is at its weakest and affects only a very small region of the flow; velocities in the plane of the laser sheet will be small, and the motion of particles slight. In these cases most of the photograph may consist of single particle images, resulting in very sparse velocity maps.

A number of researchers have helped to hone this method into a very useful and practical technique (see Adrian (1991) and Willert and Gharib (1991)); recent tip vortex studies using PIV on stationary hydrofoils include Shekariz, *et al.* (1991,

1992, 1993) and Pogozielski, *et al.* (1993) as already mentioned in Chapter 1.

PIV has the great advantage of providing an instantaneous view of the entire tip vortex region, unlike point-measurement techniques which can only collect information at a single point over time. This makes PIV data insensitive to the effects of vortex meandering, as long as there is some way to locate the vortex unambiguously in the laboratory frame of reference. It also allows a high-resolution scan of the flow field in a much shorter time span than (for example) LDV techniques. Also, like LDV but unlike hot-wire or other probe-type measurements, PIV is non-intrusive and thus does not disturb the flow.

2.4.1 Pulsed Laser Sheet

The PIV system was based upon a high-power pulsed ruby laser, designed and built at Caltech; this laser is described in detail in Acosta, *et al.* (1983). The laser cavity consists of a helical flashlamp surrounding a 4-inch long ruby rod with a 100% reflective back mirror and a 40% reflective front mirror. Between the back mirror and the ruby is a Pockels cell which is used to pulse the laser by only allowing the ruby light to pass through when a voltage is applied to the Pockels cell electrodes. Custom-built electronics allow the laser to be pulsed up to three times in short succession, with spacings up to 200 μsec or more between pulses. These instruments were originally described in O'Hern (1987), and recent modifications to them are detailed in Hart (1993).

For the present work, two cylindrical lenses were added to produce a light sheet that cut across the test section 2cm downstream of the trailing edge of the foil. See Figure 2.4 for a sketch of the setup. The laser sheet was approximately 8mm thick, sufficiently thin with respect to the distance to the focal plane of the camera such that it could be considered a two-dimensional sheet for computational purposes. The flow was seeded with microscopic fluorescent particles for the PIV images provided by J. Katz of Johns Hopkins University for this purpose. These particles are made of methyl methacrylate, dissolved and mixed with a special

dye (DTDC¹ iodine) that fluoresces precisely at the ruby wavelength of 694 *nm*. The particles are formed by spraying the mixture into a heated chamber, then collecting and washing the "dust" (20-100 micron) that forms. Since the spraying process leaves small air pockets within the particles, their specific gravity will vary between 0.95-1.1.

The flow seeding was accomplished by means of an injection system feeding into a hole bored through the rotating shaft of the foil, as shown in Figure 2.5. The particle slurry sits in a lucite tank which is fed by pressurized air. A tube extending to the bottom of the tank connects the liquid to the foil shaft, and a small channel in the brass tip cap of the foil leads the particles to a small hole at the tip of the trailing edge of the foil.

2.4.2 PIV Photographic System

The camera system used for photographing the PIV images went through several major changes during the design of the experiment. Originally, the PIV photographs were to be taken using a borescope as an inverted periscope. A special adapter was constructed so that a Nikon N2000 SLR camera and lens could be mounted directly to the eyepiece of the borescope, and the top of the test section was fitted with a device to allow the insertion point of the borescope some range of motion. This had the advantage that the borescope's position could easily be changed in order to view different regions of the flow, while remaining fairly non-intrusive. A Karl Storz borescope, model TE88310DF, was purchased and installed in the test section, only to discover that the borescope's internal lens system caused a prohibitive attenuation in the light reaching the camera focal plane. After several unsuccessful attempts to modify the borescope and camera system to admit more light, the borescope was finally discarded.

Instead, a special mirror mount was designed to bolt to the floor of the test

¹3-3'-Diethylthiadicarbocyanine

section and hold a flat first-surface mirror at approximately 45° to the freestream flow, several chords downstream of the foil. The same SLR camera was then set up outside the test section, aimed at the mirror in such a way as to gain a view looking directly upstream at the trailing edge of the foil. This allowed light from the fluorescent particles to reach the film, and a 2X teleconverter was added in order to achieve the desired magnification of the flow region of interest. The quality of the images remained poor, however, and research ensued to find a better film than either of the types tried so far (Konica 3200 color film and Kodak Tmax 3200 black and white film). After comparing several specialized film types, Kodak High-Speed Infrared Film was selected for its improved sensitivity in the red and near-infrared wavelength range. The sensitivity chart provided by Kodak for this film is shown in Figure 2.6, and the ruby wavelength of 694 nm is noted for reference. Also in the figure is the chart for Kodak Tmax 3200 film, another popular film for PIV studies but clearly less sensitive in the range of the ruby laser. The film was processed using Kodak D-19 developer, with the developing time doubled to enhance the contrast of the negatives.

At this point, photographs of the flow field showed fairly bright images of the particles. These images, however, were not clean "dots" as would be expected from the spherical particles. The problem appeared to be aberrations in the lens system, as examples of both coma and astigmatism were noted. A portion of one of the photographs, showing these aberrations, is displayed in Figure 2.7. The aberrations were reduced by eliminating the teleconverter from the system, but the magnification was now insufficient for individual particle tracking. The desired magnification was regained, without increase in optical aberration, by switching to an extension ring with an $f/2.8\text{ }70\text{-}200\text{ mm}$ zoom lens (adjusted nearly to the 200 mm focal length). Some aberrations were still noticeable, but by adjusting the 45° mirror slightly the tip vortex flow region could be moved to the center of the field where the aberrations were at a minimum. Another useful tactic was closing down the aperture (to an f -stop of 4, in most cases) and then increasing

the developing time to heighten contrast. Since the smaller aperture reduced the amount of light reaching the film plane, this had the effect of reducing the apparent particle density in the flow; however, the particles that were sufficiently illuminated by the laser sheet were recorded more cleanly on the film.

The final photographic setup for the PIV experiments is as shown in Figure 2.4.

2.5 Cavitation Data Acquisition

The surface cavitation studies on the oscillating hydrofoil consisted primarily of observations of the cavitation process, as will be discussed in Chapter 5. In addition, acoustic measurements of the cavitation noise were correlated with the observations in order to determine the specific sources of the noise.

2.5.1 Photographic Methods

Still photographs were taken of various stages of the cavitation process by using the foil timing circuit to trigger strobe lighting at the desired phase of the foil oscillation cycle.

A high speed (500 frames per second) 16mm movie camera was also used to film several complete oscillation cycles under selected conditions. This camera (LOCAM II model 50-0003 by Redlake Corp.) is equipped with two internal LEDs which mark the edge of the movie film. One of the LEDs automatically generates marks at 100Hz, which make it possible to ascertain the instantaneous framing rate of the camera in a particular segment of the developed film (this is important because the camera takes several seconds to get up to full speed). The other LED marks the film each time it is triggered by an external signal from the user.

A special circuit was designed to use the second LED to record foil timing information on the edge of the movie film, as well as to indicate the moment at which acoustic data was recorded during filming. A timing diagram illustrating

the operation of this circuit is shown in Figure 2.8. The foil "ZERO" signal was the input to the circuit, and the circuit included a "TRIGGER" button to be pressed during the filming. Normally, the "ZERO" signal marked the film every time the foil was at 0° angle of attack, except when the trigger button was pressed to record the acoustic data. Pressing the button caused the next "ZERO" pulse to be rerouted to the computer trigger input instead of the camera; this provided the necessary signal to start the data acquisition, as well as leaving a distinct blank section on the film edge which could readily be identified later as corresponding to the computer trigger time. This allowed later synchronization of the acoustic signals with the details of the cavitation process.

The high-speed motion pictures were used to obtain information about the cavitation process itself. The film was projected onto a grid, and the area covered by the cavity in a given frame was measured and normalized by the area covered by the foil surface. Certain distinctive events in the cavitation sequence were also noted, such as the moment of tip vortex cavity inception and the beginning of the collapse phase. The angle of the foil during each frame was calculated from the location of the marks on the film. For the two reduced frequencies represented by the motion pictures, 500 frames per second results in a phase angle resolution of 8.3° (for $k = 0.74$) or 6.3° (for $k = 0.56$) between frames. These correspond to changes in angle of attack of 0.46° and 0.35° , respectively.

2.5.2 Acoustic Measurements

The sound generated by the cavitation on the hydrofoil was recorded by a B&K model 8103 hydrophone (bandwidth 100kHz) installed in a Lucite box filled with water and affixed tightly to the outside of the test section. The complete arrangement is illustrated in Figure 2.3. As graphically demonstrated by Bark and van Berlekom (1978), mounting a hydrophone externally in this way significantly degrades the signal: the presence of the test section and lucite box walls has a severely attenuating effect on the measured signal, and resonances within the box

camouflage many of the finer details of the acoustic output of the cavitation. This approach is, however, a simple way to obtain preliminary qualitative information about variations in the cavitation noise level. The results discussed in this thesis, first presented in McKenney and Brennen (1994), were obtained using this imprecise method, but the major conclusions drawn from those results (see Chapter 5) were later verified using more precise acoustic measuring techniques as discussed in Reisman, *et al.* (1994). Figure 2.9 shows acoustic signals acquired using both methods, for comparison. It is clear that, while the present approach contains a great deal of adulteration from stray resonances, the qualitative information is the same: The sharp pulse in the latter trace coincides well with the high-frequency burst demonstrated using the current system.

The output signal from the hydrophone was low-pass filtered prior to being recorded by a digital data acquisition system. Since the sampling rate was approximately 143kHz , the filter was set to a cutoff frequency of 70kHz , just below the Nyquist frequency. The data acquisition system also recorded timing information from the oscillation of the foil. Acoustic data was also collected from the water tunnel test section without cavitation, for the purpose of eliminating any facility resonances from the cavitation data. It was determined that most of the tunnel impulse response appeared at very low frequencies. Since most of the distinctive features of the cavitation data are high-frequency bursts, the data was filtered using a digital high-pass filtering algorithm with a cutoff frequency of 500 Hz .

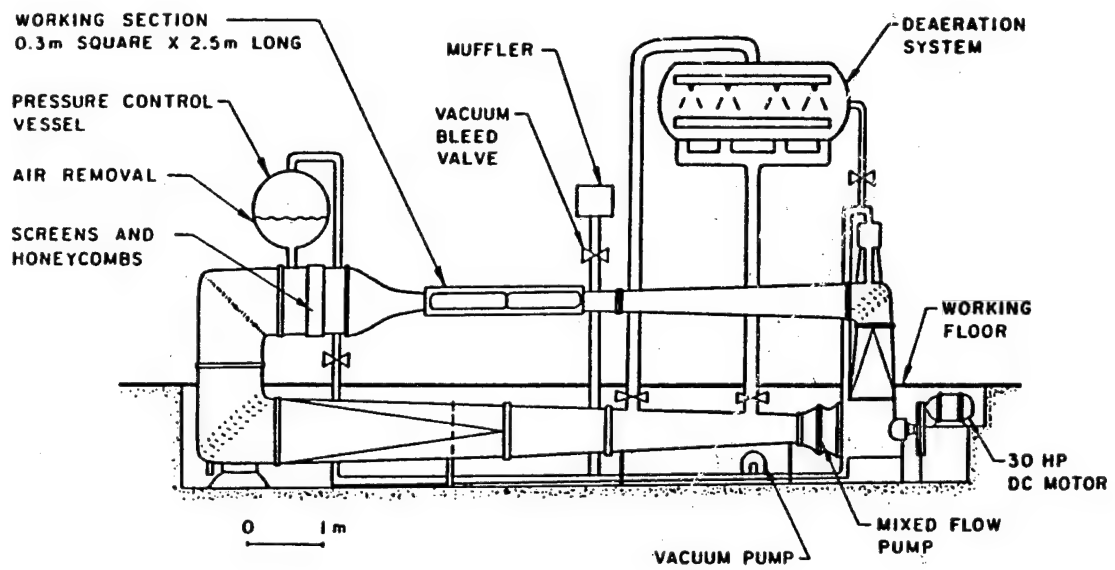


Figure 2.1: Caltech Low Turbulence Water Tunnel facility.

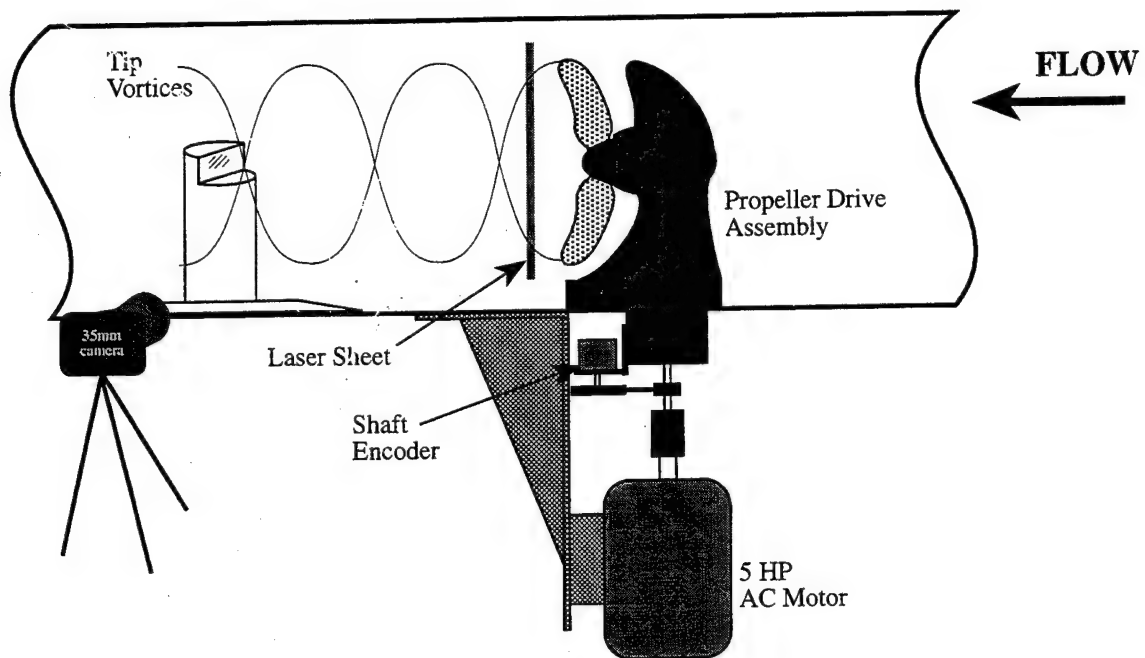


Figure 2.2: Propeller installed in the LTWT test section.

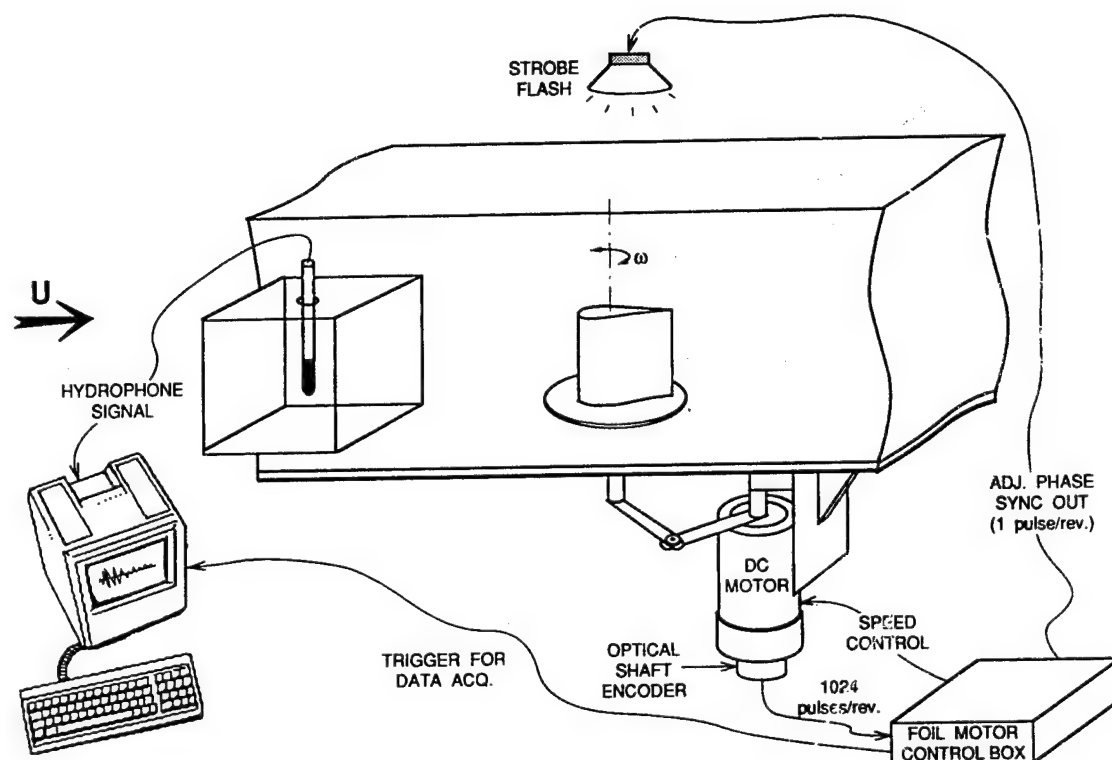


Figure 2.3: Oscillating hydrofoil in the water tunnel test section.

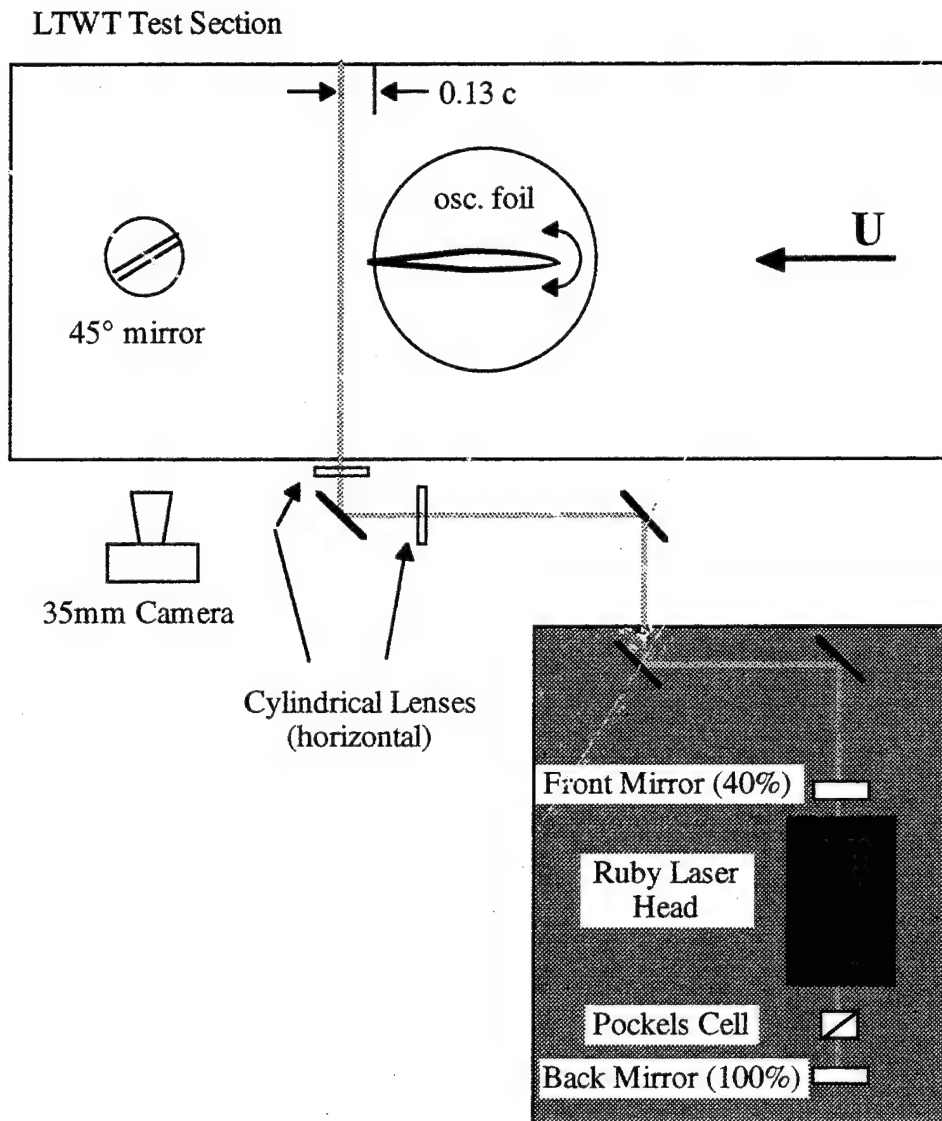


Figure 2.4: Particle Image Velocimetry setup.

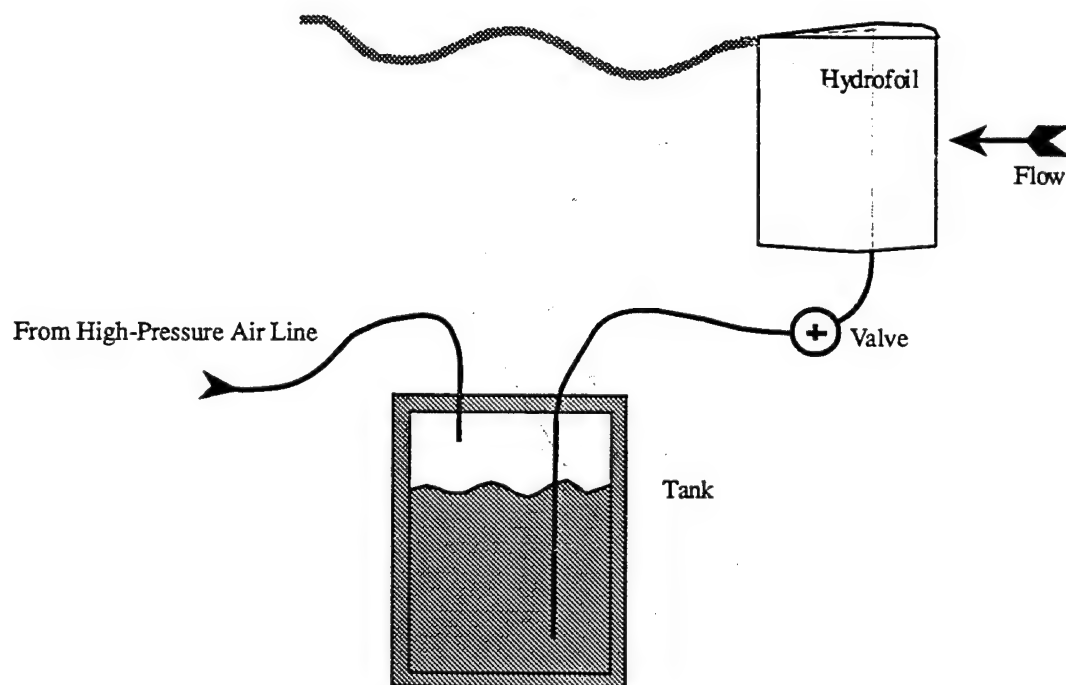


Figure 2.5: Particle injection system for the oscillating hydrofoil.

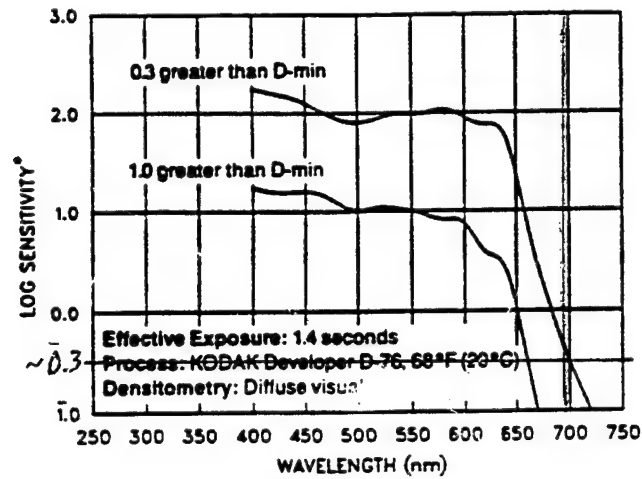
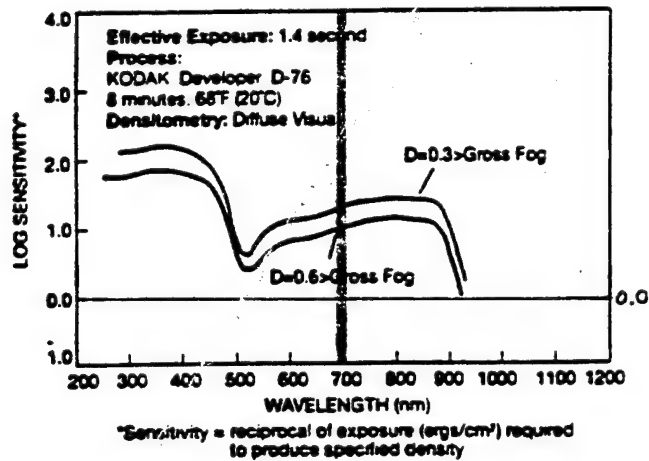
KODAK T-MAX P3200 Professional Film / 5054

KODAK High Speed Infrared Film / 4143, 2481


Figure 2.6: Sensitivity vs. wavelength charts for Kodak films.

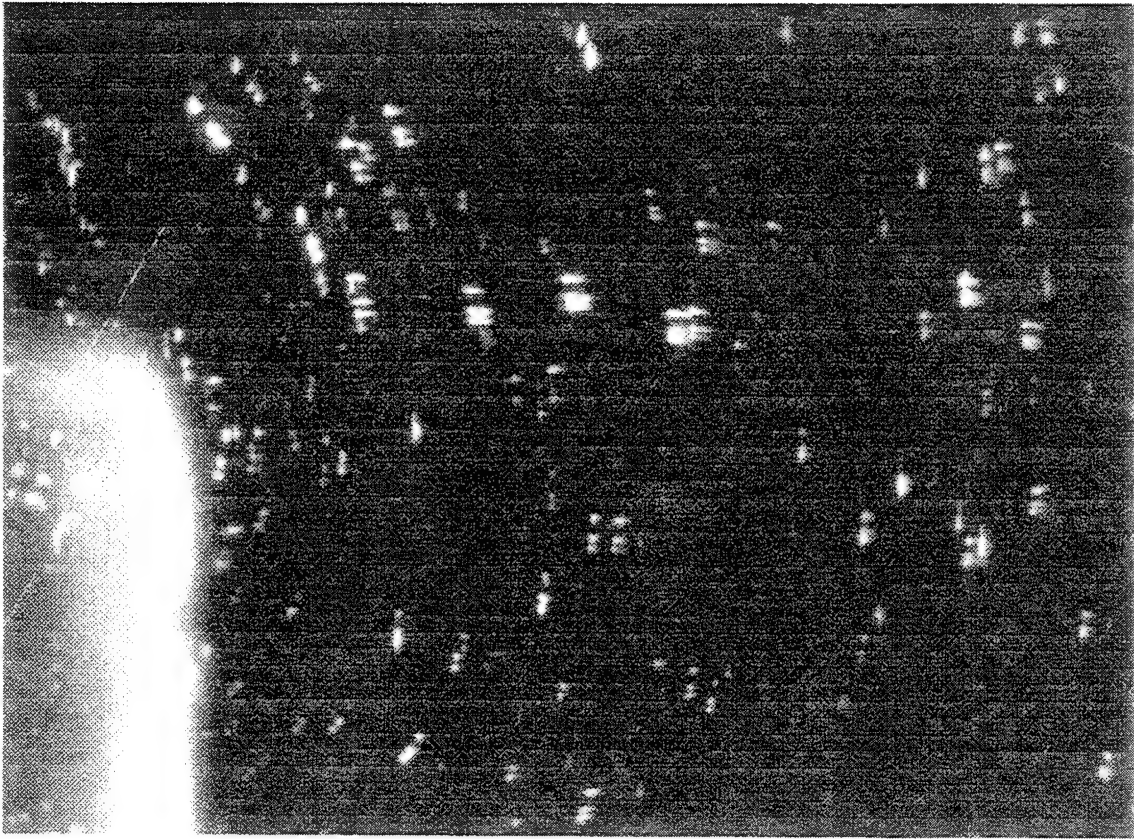


Figure 2.7: Portion of PIV image showing optical aberrations.

Camera LED Circuit Timing

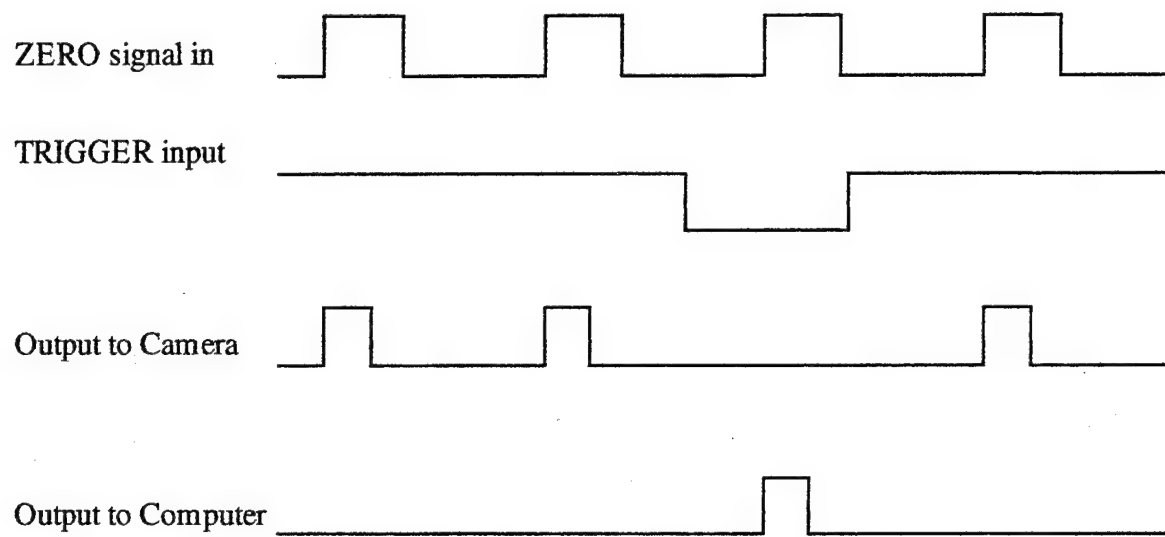


Figure 2.8: Movie camera LED trigger circuit timing.

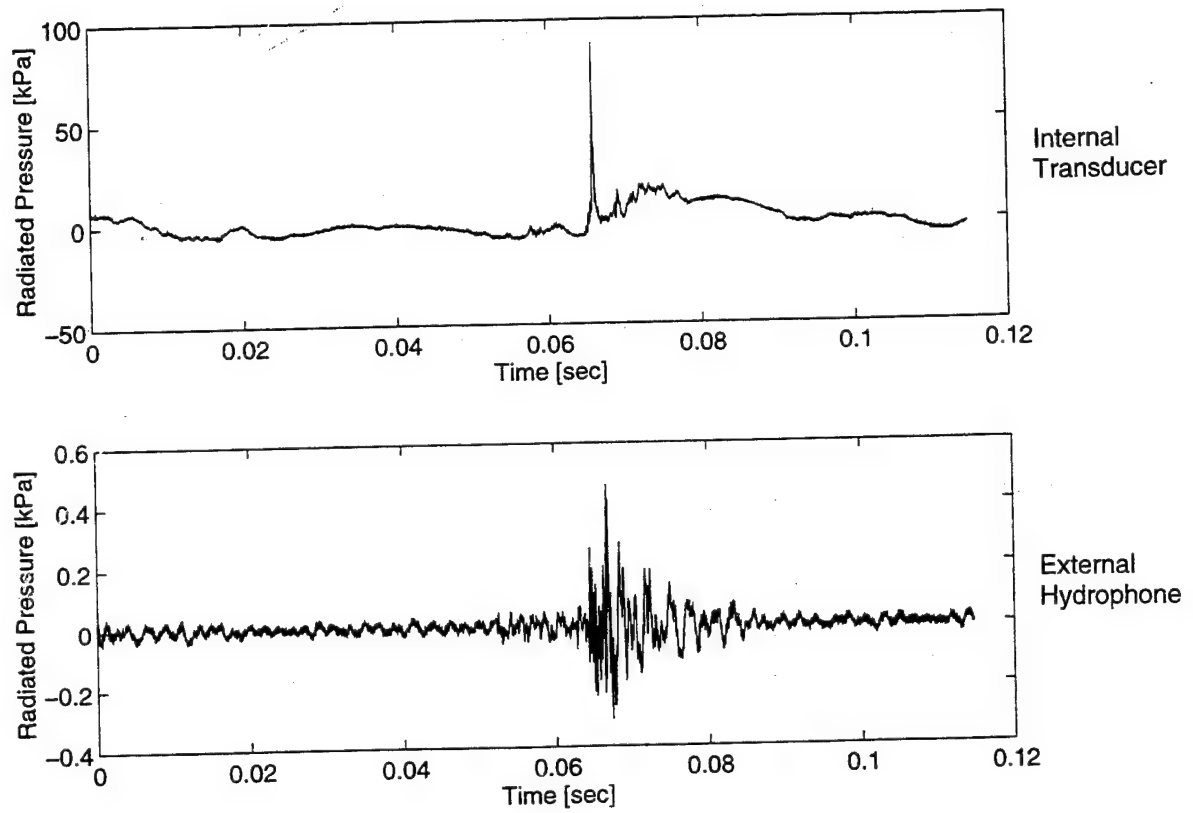


Figure 2.9: Comparison of acoustic signals from two methods. Top signal is taken from flush-mounted transducer within the test section, bottom signal is from hydrophone enclosed in lucite box outside test section.

Chapter 3 Yawed Propeller Experiments

As an application of unsteady tip vortex and cavitating flows, a commercial out-board propeller was mounted in the test section of the water tunnel and operated at various angles of yaw to the freestream flow. (The apparatus is described in detail in Appendix A.) This generated a sinusoidal variation in the inflow to each blade as it rotated through different regions of the flow. The effects of this variation on the tip vortex and blade cavitation characteristics are discussed in this chapter.

3.1 Experimental Procedures

In the current study, the propeller was yawed at angles ranging from -20° to 20° ; for each angle of yaw, the advance ratio $J = U/nd$ was varied between 0.3 and 0.7. At each set of conditions, the test section pressure was reduced until cavitation inception was observed in the tip vortex region. Still photography recorded the cavitation, using strobe lighting synchronized to the propeller rotation.

Note that since the propeller rotation speed n is kept constant in the present work, increasing the advance ratio J corresponds to an increase in inflow velocity normal to the propeller disc, as shown in Figure 3.1. This changes the angle of the resultant velocity vector relative to the propeller blade, and for a yaw angle of $\beta = 0^\circ$ always corresponds to reducing the effective angle of attack of the blade:

$$\alpha_{eff} = \alpha_0 - \tan^{-1} \frac{U_\infty}{2\pi nR}, \quad (3.1)$$

For steady flow, this reduced angle of attack leads directly to reduced lift, and

thus to a weaker tip vortex. Since the low-pressure core of the tip vortex is the location of cavitation inception, a weaker tip vortex (i.e. a higher pressure core) will require a lower ambient pressure in order to cavitate. Thus for higher advance ratios the cavitation number $\sigma = \frac{P_\infty - P_v}{\frac{1}{2}\rho U_\infty^2}$ required for inception should tend to be lower. This trend was corroborated by Sharma, *et al.* (1990) in their extensive study of cavitation and noise on propellers.

For non-zero angles of yaw, the effective angle of attack becomes more complicated, and changes with blade position as shown in Figure 3.2. Neglecting the propeller's induced velocity as well as any radial flow component, α varies as

$$\alpha_{eff} = \alpha_0 - \tan^{-1} \left[\frac{J \cos \beta}{\pi + J \sin \beta \cos \phi} \right]. \quad (3.2)$$

However, for small angles of yaw it is reasonable to assume that α_{eff} will be reduced for most blade positions as J is increased.

The overall effects of these variations may be estimated using two-dimensional blade element theory. Assuming a lift-curve slope of 2π , and a blade surface area of approximately 50cm^2 , the variation of blade loading with blade position ϕ is shown in Figure 3.3 for several values of β . Note that the variations are similar for both $\beta > 0$ and $\beta < 0$, except that the blade position of maximum loading shifts by half a rotation. It is also interesting that the mean loading on the blade section increases for both positive and negative yaw angles.

3.2 Cavitation Observations

In the current experiments, the helical shape of the tip vortex first became visible as a thin trail of small bubbles tracing the location of the vortex core. At slightly lower cavitation number, portions of this "bubble trail" often became shrouded in what appeared to be a "fog" of even smaller bubbles, entrained into the vortex flow around the core. As the cavitation number was decreased further, a tubular cavity eventually appeared in the vortex, either attached to the blade tip or at a short

distance (one to three chord lengths) from the tip. The cavity generally did not persist at first, but tended to disappear and reappear at irregular intervals until the cavitation number was decreased still further. Also, the surface of the cavity was sometimes rough enough to have the appearance of a thick cloud of bubbles rather than a single cavity. Figure 3.4 illustrates some of these observations.

The source of the “fog” of tiny bubbles just mentioned seemed to be the collapse of leading edge cavities on the blade. When the tip vortex cavitation was attached to the blade tip, it was often contiguous with a smooth narrow sheet cavity along the leading edge. The trailing edge of this sheet collapsed periodically into cloud cavitation, which was then entrained into the tip vortex flow. The bubbles created in this way appeared much smaller than those contained in the bubble trail at the vortex core, so that the core remained visually quite distinct from the surrounding fog of cloud cavitation.

This concurs with the study by Sharma, *et al.* (1990), where tip vortex cavitation was seen to occur first, then with reduced σ it “transformed from a thin trail of tiny bubbles into a twisted ribbon-like developed cavitation attached to the blade tip.” When the ambient pressure was reduced still further, the cavitation attached to the tip developed into sheet cavitation extending across the blade surface to an extent dependent on σ . They found these effects, in general, to occur simultaneously on all blades of the propeller.

As the yaw angle was varied in the current experiments, however, variations in the cavitation could be observed from one blade to another. At a yaw angle of $\beta = -20^\circ$, for example, cavitation tended to appear at roughly the same cavitation number on all three blades, and usually began as the simple “bubble-trail” variety. For $\beta = 0^\circ$, there was a slight but detectable difference in cavitation inception number between blades, though in appearance the cavitation was still similar. When the yaw angle was increased to $\beta = 20^\circ$, however, the differences between individual blades became quite striking. One blade in particular tended to cavitate quite readily with a thin bubble trail, while at the same cavitation number the

other two blades showed no cavitation. When the cavitation number was decreased sufficiently, one of the remaining blades began to show bubble-trail cavitation in the tip vortex, often with the faint "fog" of small bubbles clustered around the core. The third blade resisted cavitating until the cavitation number was very low; when it did cavitate, it immediately presented a continuous tubular cavity in the vortex core, sometimes attached to the blade tip and at other times appearing about one chord length from the tip. At its first appearance the tubular cavity was very intermittent, and the cavitation number had to be decreased still further before it became steady. These findings illustrate the very small but crucial variations in shape or surface quality between the blades of the propeller.

The study by Sharma, *et al.* (1990) included observations of cavitation on a propeller operating in a simulated hull wake. It was found that inception occurred at the "vertically top position," which in their case corresponded to the location of lowest J in the varying inflow. They noted that the non-uniform inflow changed the type of cavitation dramatically. What had once been steady tip vortex cavitation now became "cloud-type cavitation with violent bursts" as the pressure was reduced, and tip vortex cavitation, when present, was highly unsteady. Leading edge sheet cavitation was no longer smooth and clear, but now thick and frothy. The effect of the wake was especially noticeable as the blade passed through regions of low J and then out again (into higher J)—these variations seemed to force the cavitation to increase and decrease with a frequency dependent on the time of passage. When this frequency was sufficiently high, the effect was cavitation that collapsed violently with "cloud-like large scale structures." The photographs in Figure 3.5 seem to illustrate this, particularly in the case of $\beta = 20^\circ$. In the current experiment, the point of lowest J is at $\phi = 180^\circ$, at the bottom of the propeller disc, where the gearcase impedes the flow and interactions with the junction vortex between the gearcase and the test section floor may also contribute.

The effect of the gearcase wake in the current setup is evident in Figure 3.5. Photographs of the tip vortices under cavitating conditions show how this effect

changes with yaw angle. In the first photograph, $\beta = 0^\circ$; the tip vortex cavities are mostly smooth and stable for nearly one and one half full propeller revolutions. The kinks in the vortices near the test section floor indicate the influence of the collar vortex, formed where the gearcase meets the wall. When the yaw angle is increased to $\beta = 10^\circ$, as in the second photograph, the cavities can be seen to break down after only one full revolution, and the kinks near the wall appear more tangled, perhaps contributing directly to the early cavity breakoff. Finally, at $\beta = 20^\circ$ the vortex cavities break down very quickly, after only about three-fourths of a revolution as shown in the third photograph. Here the floor kinks appear to be directly involved in the vortex breakdown, and in fact persist long after the helical vortices have dissipated, taking on the appearance of cloud cavitation (a phenomenon known to contribute to particularly high levels of noise and erosion, see Bark and van Berlekom (1978) and Shen and Peterson (1980)) as they are convected downstream.

3.3 Cavitation Inception Results

Figure 3.6 shows the results of cavitation inception measurements for various yaw angles. For all yaw angles, the cavitation inception number can be seen to decrease monotonically with increasing advance ratio, J , as expected from the discussion in Section 3.1. On a propeller, the noise produced by cavitation occurs immediately with the appearance of visible tip vortex cavitation; many studies have shown it to increase rapidly with reduced cavitation number (i.e. reduced static pressure or increased velocity), until the cavitation is fully developed on the blade, at which point further reduction of σ has little discernible effect on the noise. Strasberg (1977) observed the values of σ at which this sudden jump in noise occurred for propellers in uniform flow, and graphed them for various slip ratios. The slip ratio, S , is a measure of the operating conditions of the propeller,

calculated from the relation

$$S = 1 - \frac{U_{\infty}}{n\Phi}, \quad (3.3)$$

where U_{∞} is the hull speed, n is the propeller rotation speed (in CPS), and Φ is the propeller pitch at radius $r = 0.7R_o$ (in units of length). In terms of the advance ratio J ,

$$S = 1 - J \frac{d}{\Phi}, \quad (3.4)$$

where d is the propeller diameter. Strasberg found an empirical relation which described the variation of σ with S for a large variety of propellers

$$\sigma = 1.9 \cdot e^{6.6 \cdot S} = 1.9 \cdot e^{6.6(1 - J \frac{d}{\Phi})}, \quad (3.5)$$

This curve is plotted on Figure 3.6 for comparison with the current results. It is somewhat higher than the present data, which might be due to a difference in total air content (TAC) of the water between Strasberg's experiments and the current work, but it clearly has the same general shape including a shallower slope at low J .

Note in Figure 3.6 that for the smaller yaw angles ($\beta = 0^\circ, 5^\circ$, and 10°), the data do not vary significantly either in slope or in magnitude. Then for $\beta = 15^\circ$ and 20° the curves appear to be slightly less steep, and for $\beta = -20^\circ$, the curve seems to shift slightly downward for all values of J . These small variations may be of some interest in a more detailed study, but it seems that there is little significant effect of propeller yaw angle on cavitation inception number. It is interesting to contrast this result with the striking differences observed in the type of cavitation with yaw angle; it appears that while the appearance of the cavitation may change significantly as the propeller yaw angle is varied, the cavitation will tend to appear at approximately the same conditions for all the yaw angles studied. Since the noise produced by the cavitation depends a great deal on the type of cavitation, the effect of yaw angle still promises to yield useful insights with further study.

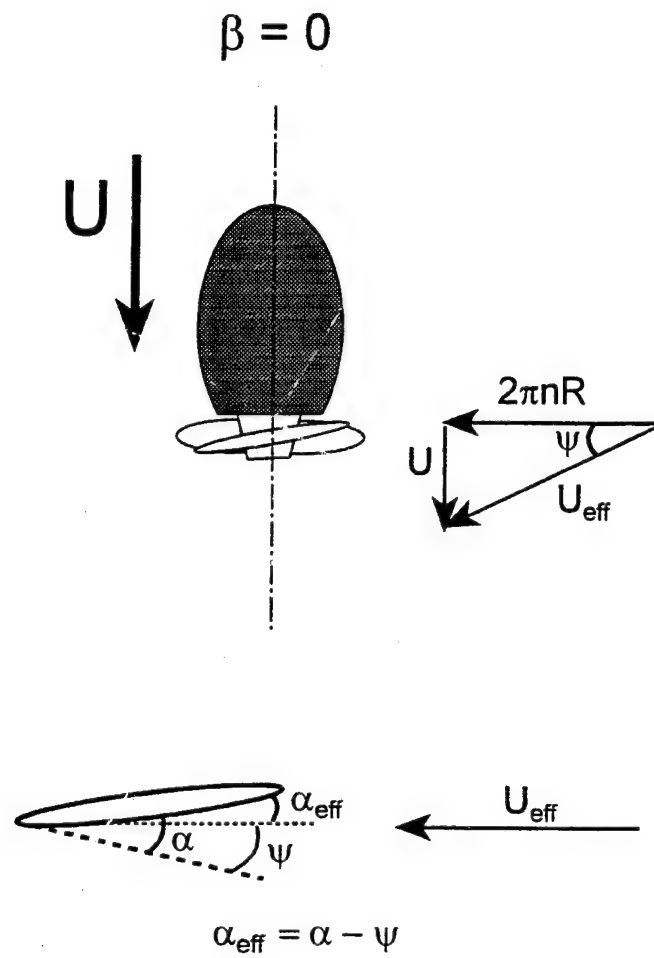


Figure 3.1: Geometry and notation for $\beta = 0^\circ$.

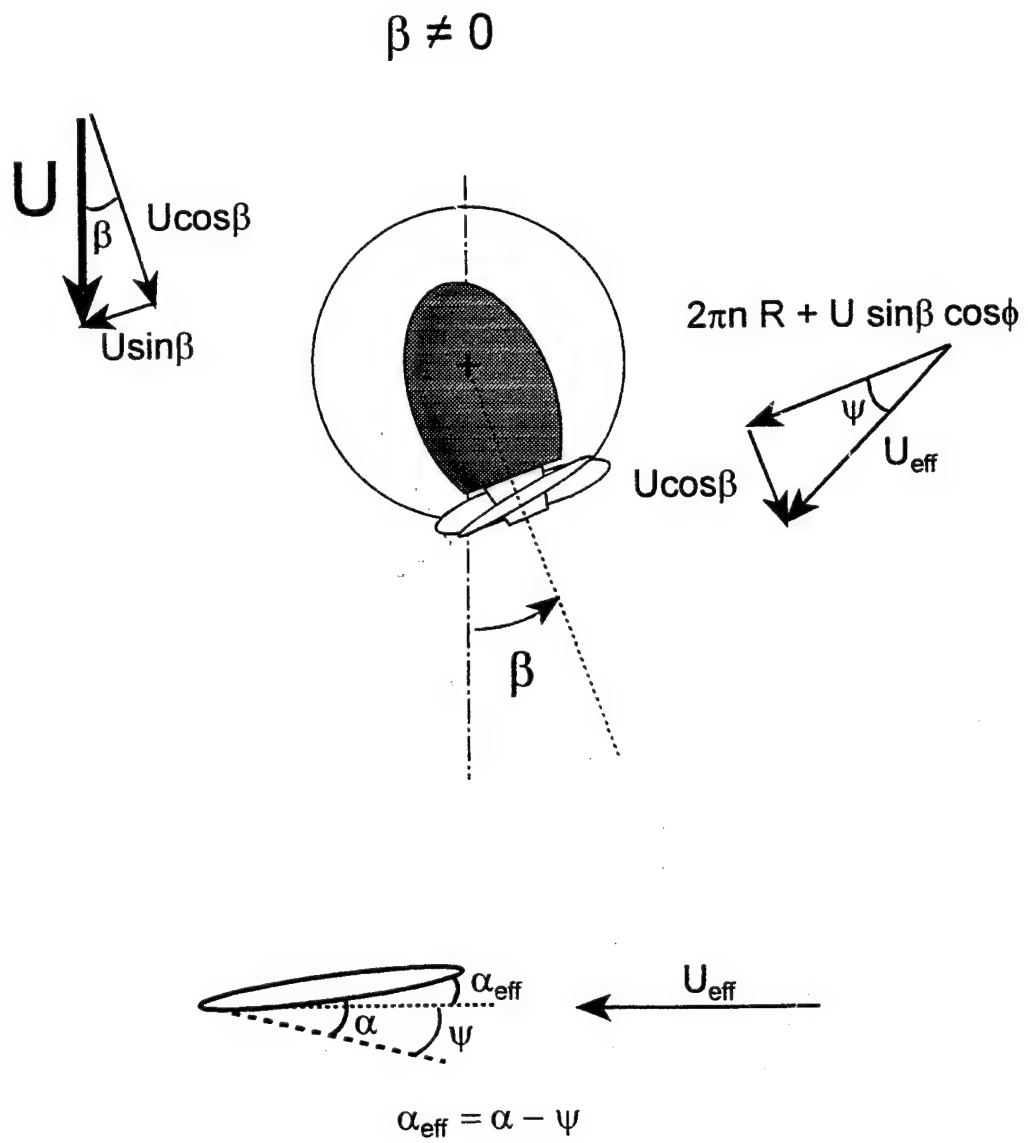


Figure 3.2: Geometry and notation for $\beta \neq 0^\circ$.

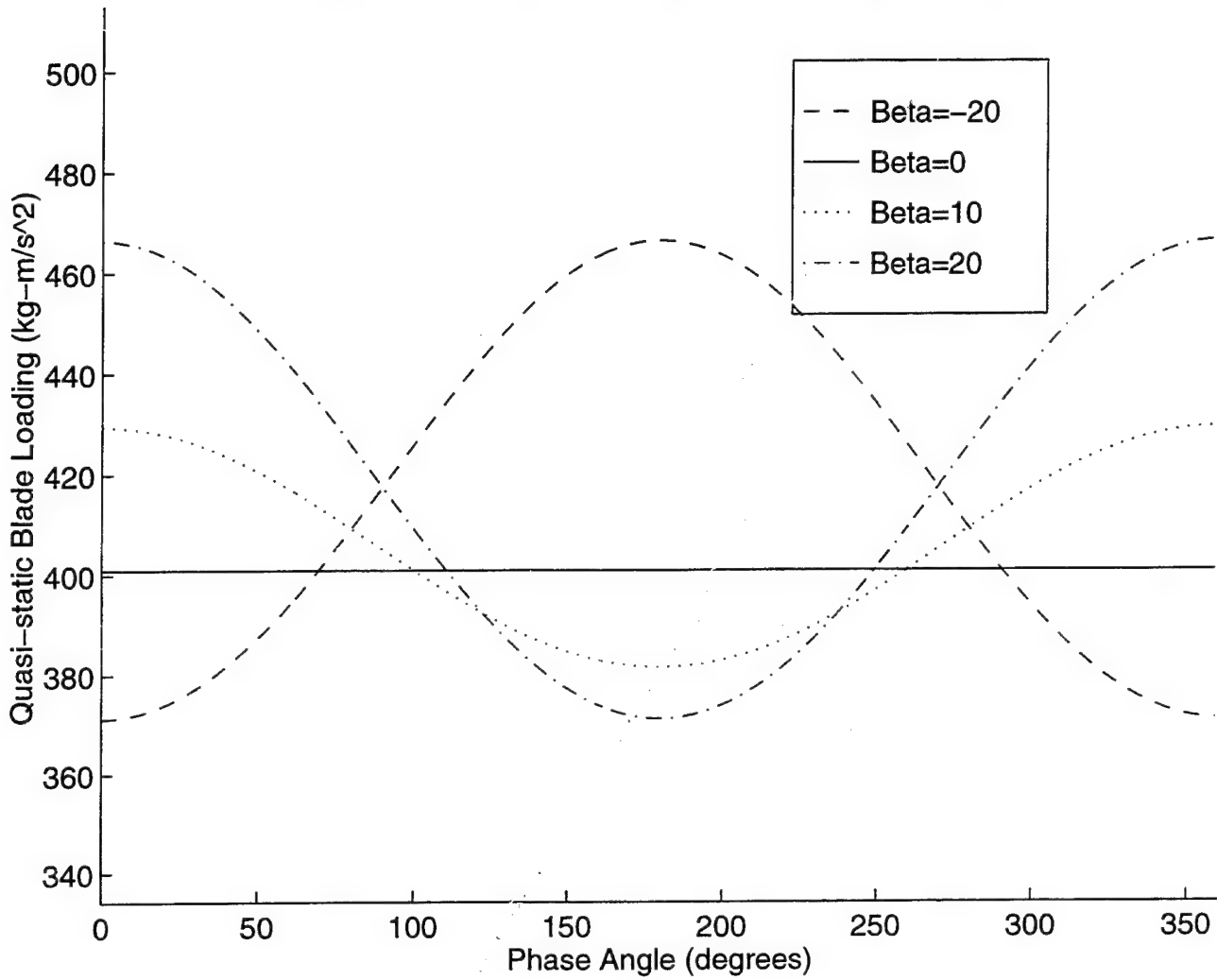
Quasi-static Blade Loading: $J=0.4$, Varying Yaw Angle

Figure 3.3: Variation in quasi-static blade loading with blade position (2D).

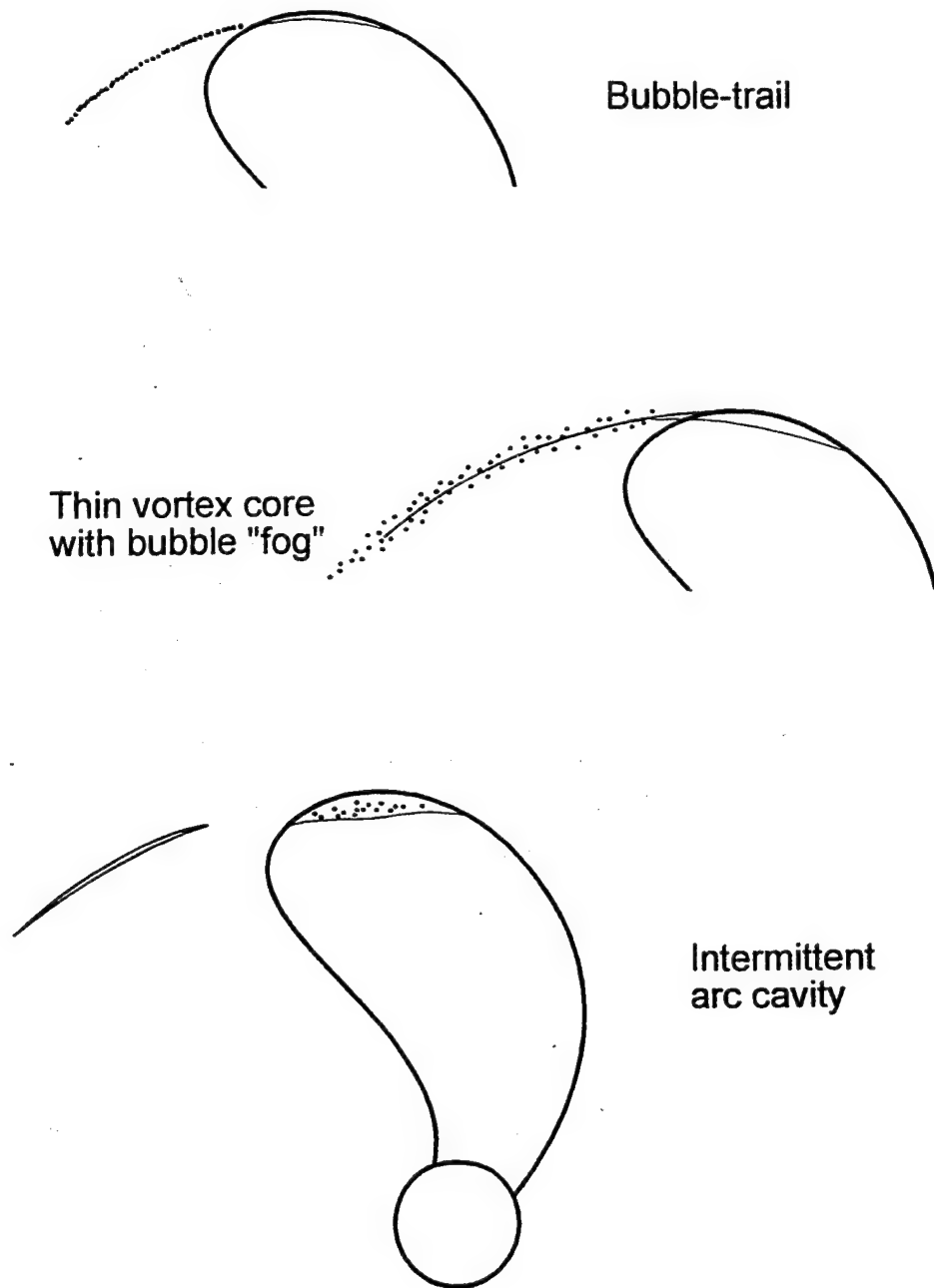


Figure 3.4: Types of cavitation observed near inception.

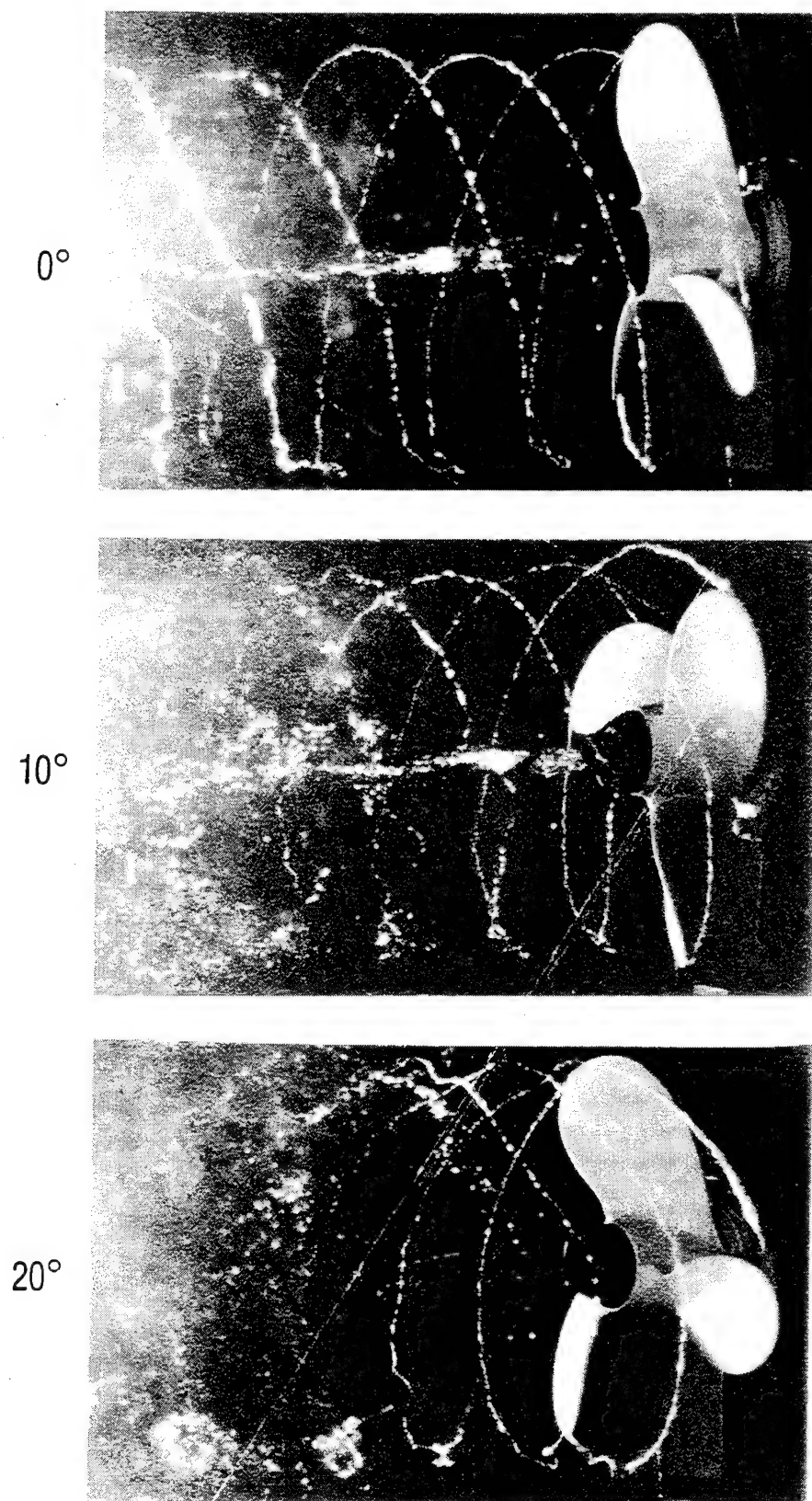


Figure 3.5: Photograph(s) of tip vortex cavitation. $\beta = 0^\circ, 10^\circ, 20^\circ$; $\sigma_T = 0.6$, $J = 0.4$.

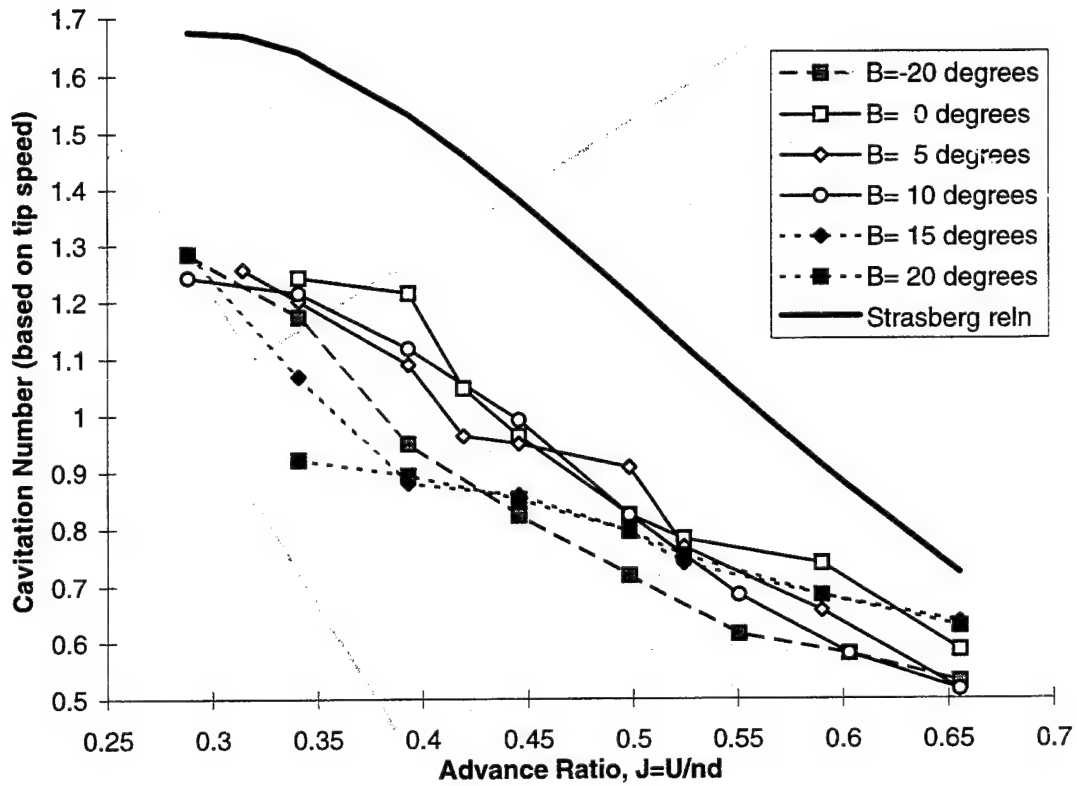


Figure 3.6: Tip vortex cavitation inception number σ_T as a function of advance ratio $J = \frac{U}{nd}$, for different values of β .

Chapter 4 Tip Vortex Studies

A hydrofoil oscillating sinusoidally in pitch was used to generate an unsteady tip vortex, not unlike what might appear on a propeller in a non-uniform inflow. The flow conditions were chosen to coincide with those of Hart (1993), who used the same oscillating hydrofoil setup to make LDV measurements of the unsteady wake. Hart (1993) examined not only the tip vortex on the oscillating foil but also spanwise vortices shed periodically by the foil, using LDV and photographic techniques. Though the flow quantities measured are somewhat different, there is enough overlap to provide a useful validation for the PIV technique.

4.1 Current Experiments

As described in Chapter 2, the encoder pulses from the foil oscillation mechanism were processed by the foil motor control unit so that a synchronization pulse could be output when the foil reached the selected phase angle. This pulse was then used to trigger the ruby laser to triple-pulse a light sheet that was directed across the test section, illuminating a plane normal to the freestream about 2 *cm* downstream of the trailing edge of the foil. A camera aimed at the side of the test section viewed the oncoming flow by means of a 45° mirror placed in the flow; the shutter was kept open during the three laser pulses so that the multiple particle images would be caught on a single exposure. This resulted in photographs containing three images of each particle that was caught in the laser sheet during the three pulses, such as may be seen in Figure 4.1.

The change in position of a given particle between images indicates the direction and magnitude of the particle's velocity in the plane of the laser sheet (the streamwise velocity component cannot be discerned). The first two laser pulses

were set 100 μsec apart, and the third pulse 200 μsec later, in order to preserve the direction of the velocity vector. There was a short delay between the trigger to the laser (which occurred precisely at the desired phase angle) and the first laser pulse, either 500 or 600 μsec depending on the particular image. This corresponds to a phase angle offset ranging from 0.9° to 2.16° depending on the oscillation frequency; this was considered negligible for the present dataset.

Up to eight different phase angles were captured in this manner, for each of two oscillation frequencies (5 Hz and 10 Hz); the corresponding reduced frequencies of oscillation, $k = \omega c / 2U_\infty$, are $k = 0.48$ and $k = 0.96$. PIV images were also acquired for three different foil positions at the same freestream velocity but without oscillation (" $k = 0$ "); for these runs the foil was adjusted by hand to the desired angle of attack: $\alpha = 0^\circ$, $\alpha = 5^\circ$, or $\alpha = 10^\circ$. In plotting the results, the $k = 0$ case was treated as though each static angle of attack was actually part of an oscillation cycle; thus $\alpha = 5^\circ$ and $\alpha = 0^\circ$ were repeated for phase angles of $\phi = 270^\circ$ and $\phi = 360^\circ$, respectively.

The negatives were developed, then scanned into a computer at 2168 dpi using a Nikon LS-3500 SR1 high-resolution film scanner. Once on the computer, the images were processed to remove background noise and to enhance the particles, as may be seen in Figure 4.2. The filtering algorithm¹ consisted of analyzing the image in small pieces, or "windows", 32 by 32 pixels at a time. The histogram of the pixel values in each window was adjusted so that the darkest 90% of the pixels were changed to black and the remaining pixel values were "stretched" across a larger range of the histogram to enhance the contrast.

Once filtered, the digitized images were analyzed using a particle-tracking algorithm written for Visual Numerics' PV-Wave². This program allows the user to view the image and to select likely pairs of particle images by hand; the program then calculates the distance (in pixels) between the centers of the selected items.

¹Author: G. Roth, Johns Hopkins University

²Author: G. Sridhar, Johns Hopkins University

Once the entire image has been analyzed in this fashion, the data can be converted to actual velocities by using known conversion factors for true distance and time: In this case, calibration photographs taken at the same time as the data provided the necessary information to convert pixel measurements to true distances, and the time of travel (either 100 or 200 μsec) was easily identified from image context.

The method described above results in a map of the velocity field at a given phase angle of the foil, at a given reduced frequency, as shown in Figure 4.3. Since the velocity vectors were obtained from naturally-occurring particle movements they will not be evenly spaced, and there are often patches of missing data due to non-uniform seeding of the flow. This can lead to difficulties in developing methods of analyzing the results, since statistical methods (which are usually the simplest to implement) require fairly dense data in order to produce valid results. As shall be discussed shortly, however, alternative methods may be devised to circumvent such difficulties.

The spanwise component of this velocity field can be compared directly with the spanwise velocities obtained by Hart (1993) using LDV; Figure 4.4 shows one such comparison. The LDV measurements shown were taken at a single spanwise location, but since the vortex core location is not precisely known in the Hart data it is not possible to choose the PIV vectors that correspond to the same spanwise location. Instead, the spanwise component of each measured velocity vector in the PIV image was plotted against its normal distance from the foil trailing edge. As can be seen in Figure 4.4, this introduces a great deal of apparent scatter in the data since the velocity magnitude drops off at spanwise locations far from the vortex core. Even so, it is clear that the Hart LDV data provide an envelope, or outer bound, on the PIV results.

4.2 Unsteady Vortex Characteristics

Some qualitative observations may be made simply by looking at the images.

- As observed by Stinebring, *et al.* (1989), the flow in the tip vortex region is mostly circumferential, but inboard of the vortex core on the suction side the flow may be seen to turn toward the midspan of the foil. This suggests that the spanwise velocity component induced by the finite-wing effect persists even downstream of the trailing edge.
- At small angles of attack some sort of secondary flow is visible, at about $y/c = 0.1$ inboard of the tip along the trailing edge. As can be seen in Figure 4.5, the movement is small enough that multiple particle images cannot be clearly distinguished, so the actual velocity field in this region remains unknown. The pattern, however, is reminiscent of Donaldson, *et al.* (1974), who showed how the trailing vortex sheet can roll up into several streamwise vortices, whose locations and strengths depend on the circulation distribution along the span of the foil. This secondary flow is evident only at low angles of attack, and only when the angle of attack is constant ($k = 0$) or increasing, suggesting that the flow field generated by the returning foil may suppress this secondary mechanism.

Other characteristics of the vortex can be measured directly on the images, using the scale of the images to extract actual distances. (In the case of the current dataset, the scale was approximately 34 pixels/mm.) Two items in particular may be of interest: the size of the vortex core and the distance from the center of the vortex to the trailing edge.

On each of the images, the vortex core stands out as a region of higher particle density, with a sharp discontinuity in that density between the core region and the outer vortex flow. This occurs because the particles are injected into the flow at the tip near the trailing edge, so nearly all are entrained into the core. (Particles in the outer flow and the freestream come mainly from early experimental runs, since no effort was made to filter them out.) Figure 4.6 shows how the core of the vortex (where the particles are most dense) changed size with phase angle and

with reduced frequency. The error bars indicate the range in diameter for the two images analyzed for each phase angle. It is interesting to note that the vortex diameter at the higher angles of attack appears to increase slightly with reduced frequency.

The vortex core size was also measured as the distance from the center of the vortex to the radius of maximum tangential velocity. As shall be seen later in this chapter, the latter method does not generate a clearly defined peak in most cases. This has the result that, although by eye a good guess can be made as to the radius at which the maximum tangential velocity is achieved, the error bars tend to be quite large, as can be seen in Figure 4.7 where the two methods are compared.

Plotting the change in vortex location (relative to the trailing edge) reveals slight changes with reduced frequency, as shown in Figure 4.8. The schematic in the figure describes how the measurement was made on the images. The vortex distance from the foil trailing edge increases and decreases along with the foil angle of attack, but it is significantly farther from the foil when the angle is increasing relative to when it is decreasing. Since the pitching axis of the foil is near the leading edge, increasing the angle of attack will move the trailing edge away from the tip vortex, which resides slightly on the suction side of the foil, and decreasing the angle will move the trailing edge back towards the vortex. It is also interesting to note the variations with reduced frequency: As the reduced frequency is increased, the distance from the vortex core to the trailing edge increases in the first half of the cycle (increasing α), but not in the second half. The maximum distance also appears not to change significantly with reduced frequency.

4.3 Unsteady Circulation Results

Perhaps the quantity of greatest interest in these experiments is the changing value of the circulation as the foil pitches through a single cycle. Circulation can be calculated from the velocity maps in two ways: Direct contour integration of the flow field

$$\Gamma = \oint \vec{V} \cdot d\vec{u} = \int_A \omega \cdot dA \quad (4.1)$$

is the most general method, as it makes few assumptions about the flow characteristics. On the other hand, it is more sensitive to errors in individual velocity vectors and it generally requires a fairly dense data set in order to find a reasonable contour over which to integrate.

For the current dataset, which has already been seen to be quite irregular, a special method was devised to calculate the contour integral. First, the dataset was displayed on the computer screen in the form of markers indicating the locations of the velocity vectors. Then a contour was defined by the user selecting a series of these data points with the computer mouse; each segment of the contour was displayed as a line segment on the screen connecting successive data points. The integration was performed by calculating the dot product of each line segment vector with the velocity vector corresponding to the initial point of the line segment. The circulation was then the accumulated sum of these dot products around the contour. Figure 4.9 shows the display at the end of this calculation routine; the circulation value calculated from this contour was $0.137m^2/s$.

A circulation profile for the same image was constructed by taking successively larger contours, all containing the origin, as shown in Figure 4.10. Figure 4.11 illustrates how the circulation increased with increasing contour size. A^* is a non-dimensional contour area, in this case defined as $A^* = \frac{\pi}{4}(d/D)^2$ where d is the approximate diameter of the contour and D is the vortex diameter as observed on the original image. This type of abscissa was suggested in Shekarriz, *et al.* (1991) as a useful one because it allows the slope of the curve to represent the

mean local vorticity. Note in particular the distinct change in the slope as the contours become larger than the diameter of the vortex core (i.e. where $(d/D) > 1$ and thus $A^* > \frac{\pi}{4}$). This reflects the transition in the flow regime from the solid body rotation of the vortex core to the viscous diffusion region outside the core, as described in Shekarritz, *et al.* (1991).

In order to compare circulation values for different phase angles consistently, contours in each image were selected to follow the circumference of the vortex core region as closely as possible. Since the circulation curve levels off somewhat outside the core, this should provide a reasonable estimate of the circulation.

Another way to gain a rough estimate of the circulation is to assume the conditions of a circular vortex in inviscid flow; it then follows that the tangential velocity outside the core region of the vortex should follow the Rankine velocity profile $V(r) = \Gamma/2\pi r$. Plotting the magnitude of the velocity vector against its distance from the vortex center, and fitting the outer portion of the resulting data set (i.e. the region where $r \geq d/2$ where d is the measured vortex core diameter) to a curve C/r for some constant C , we may calculate an approximate measure of $\Gamma = C \cdot 2\pi$. (The vortex center locations can be found within a few pixels by examining the images visually, as discussed previously.) A typical data set, with its best curve fit, is shown in Figure 4.12. The calculated circulation was $0.140\text{m}^2/\text{s}$, or within about 2% of the value obtained using the contour integration routine.

To compare the relative accuracies of these two calculation methods, see Figure 4.13 where the results for the $k = 0.48$ case are plotted together. Clearly the two methods show very good agreement; for the sake of consistency, subsequent plots in this chapter will use only the contour integration results.

Figure 4.14 shows the variations in circulation with phase angle, plotted along with calculated results for two-dimensional foils. The highest curve represents the circulation on a stationary two-dimensional foil at each angle of attack represented by the phase angles on the axis (assuming a lift curve slope of 2π), and the next

highest curve shows the calculations of Theodorsen (1935) and Garrick (1936) for a pitching two-dimensional foil. The peak circulation on the finite-span oscillating foil is less than both of the curves based on two-dimensional theory, due to the effects of the finite span: Both the spanwise component of the velocity near the foil surface (caused by the same pressure imbalance that produces the lift) and the downwash induced by the tip vortex flow at the tip of the foil decrease the effective angle of attack and the effective inflow velocity, leading to a decrease in the circulation. The steady circulation at the maximum angle of attack of 10 degrees, for example, is about 0.41 as compared to the experimental value of 0.14 seen in the plot.

In the unsteady 2D calculations of Theodorsen and Garrick, the peak circulation is reduced to about $0.25 \text{ m}^2/\text{s}$. This curve, calculated from theory for a flat-plate airfoil, actually goes slightly negative near $\phi = 350^\circ$; this is a result of the kinematic change in the foil angle of attack due to the oscillation. There is also a clear phase shift between the static circulation peak and the peak in the Theodorsen curve; both of these effects have been discussed fully in Hart (1993). There is no clear phase shift in the experimental data, but the coarse resolution of the data points makes it difficult to say with certainty where the actual peak value of the circulation may lie.

The circulation results gained here were also compared to calculations made by Hart (1993) based on LDV measurements of the unsteady foil wake. From the jumps in streamwise velocity across the trailing edge, he calculated the variation with phase angle of the time derivative of spanwise circulation. For comparison with the present work, the circulation gradients were integrated to obtain the curve shown in Figure 4.15. Since this calculation does not include the steady value of Γ , an arbitrary constant was added—in this case equal to the value of the minimum PIV circulation. The figure shows that the shapes of the two curves agree fairly well in phase, even considering the few points in the current dataset. It is hard to discuss the relative magnitudes of the two curves since the magnitude

of the Hart data contains this arbitrary constant, but the apparent reduction in magnitude could be attributed to the fact that at the position of the laser sheet in the current experiments ($x/c = 0.13$) not all of the spanwise circulation has yet rolled up into the tip vortex.

Figures 4.16 and 4.17 show similar comparisons with the two-dimensional theories and with the integrated Hart results for the case of $k = 0.96$. Here again the sparseness of the current data makes it difficult to make any detailed comments on the relative phase of the different curves, but the relative magnitudes show the same trends as for the $k = 0.48$ case. It would be very interesting to examine the apparently significant differences in magnitude between the Hart results and the current calculations for $k = 0.96$; perhaps a later study will make more detailed measurements.

Circulations for all three reduced frequencies (including $k = 0$) are re-plotted together in Figure 4.18. The peak circulation seemed to increase slightly as the reduced frequency was increased from $k = 0$ to $k = 0.48$, then it decreased significantly as the reduced frequency was increased further to $k = 0.96$. The latter trend was also observed by Hart (1993) in his study of tip vortex cavitation inception on the oscillating foil; the cavitation inception number decreased with reduced frequency up to about $k = 2$, then began to increase again as forces on the foil begin to be dominated by added mass effects. Since the cavitation number is based on the local pressure of the fluid, and the pressure is proportional to the square of the vortex tangential velocity (as mentioned in Chapter 1), it makes sense that the circulation should show the same trend as the cavitation inception number—and in fact Hart's LDV results reflect this as well.

It would also be advantageous to calculate the effects of unsteady flow on cavitation inception in the tip vortex; this unfortunately needs a more detailed understanding of the vortex structure than may be gained from these preliminary results. This information, however, could be extracted from future data sets if the PIV system were used to take velocity measurements at a greater number of

phase angles and at several downstream locations.



Figure 4.1: PIV image showing tip vortex on foil; $k = 0.48$, $\phi = 180^\circ$.

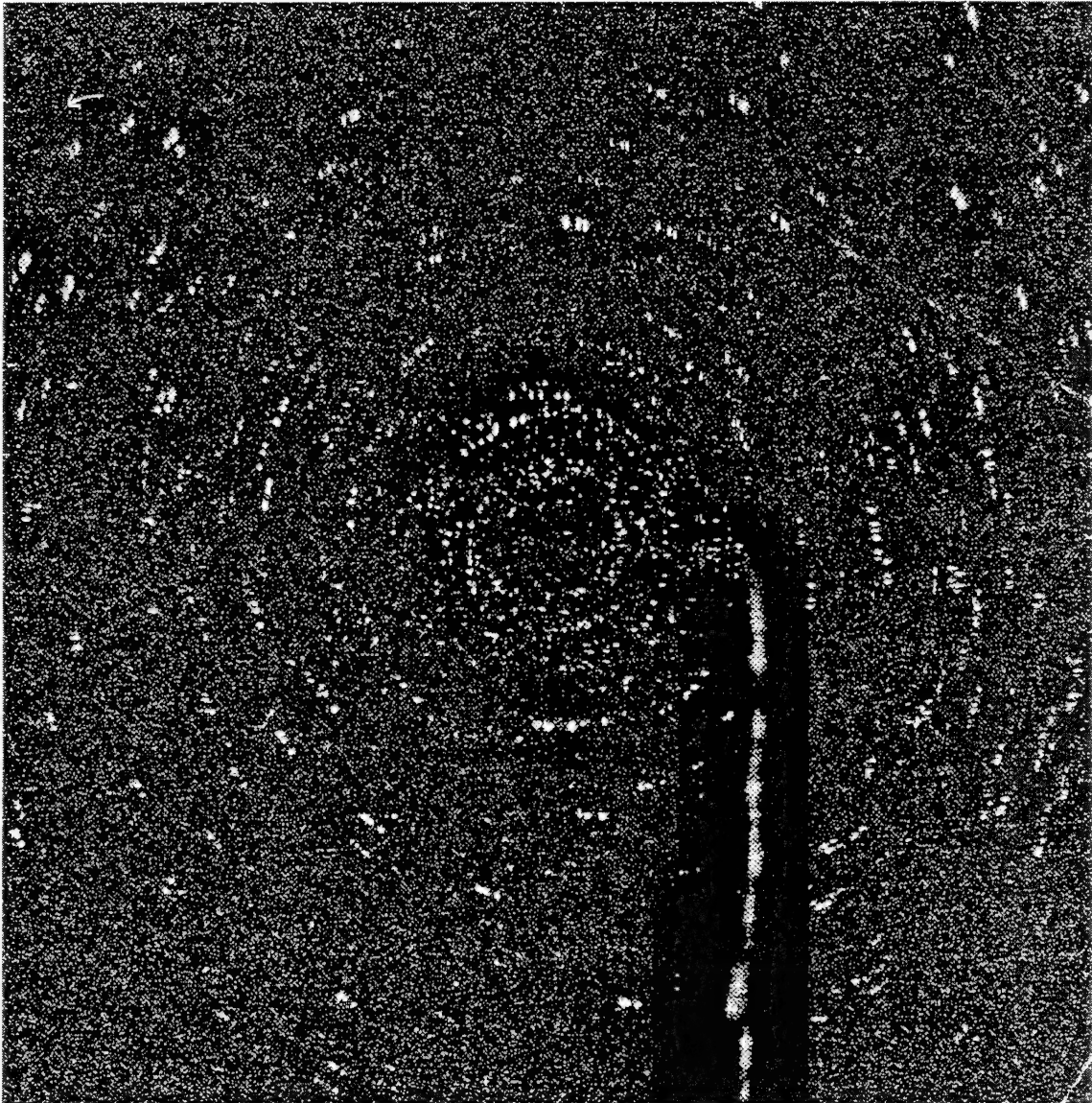


Figure 4.2: Filtered PIV image; $k = 0.48$, $\phi = 180^\circ$.

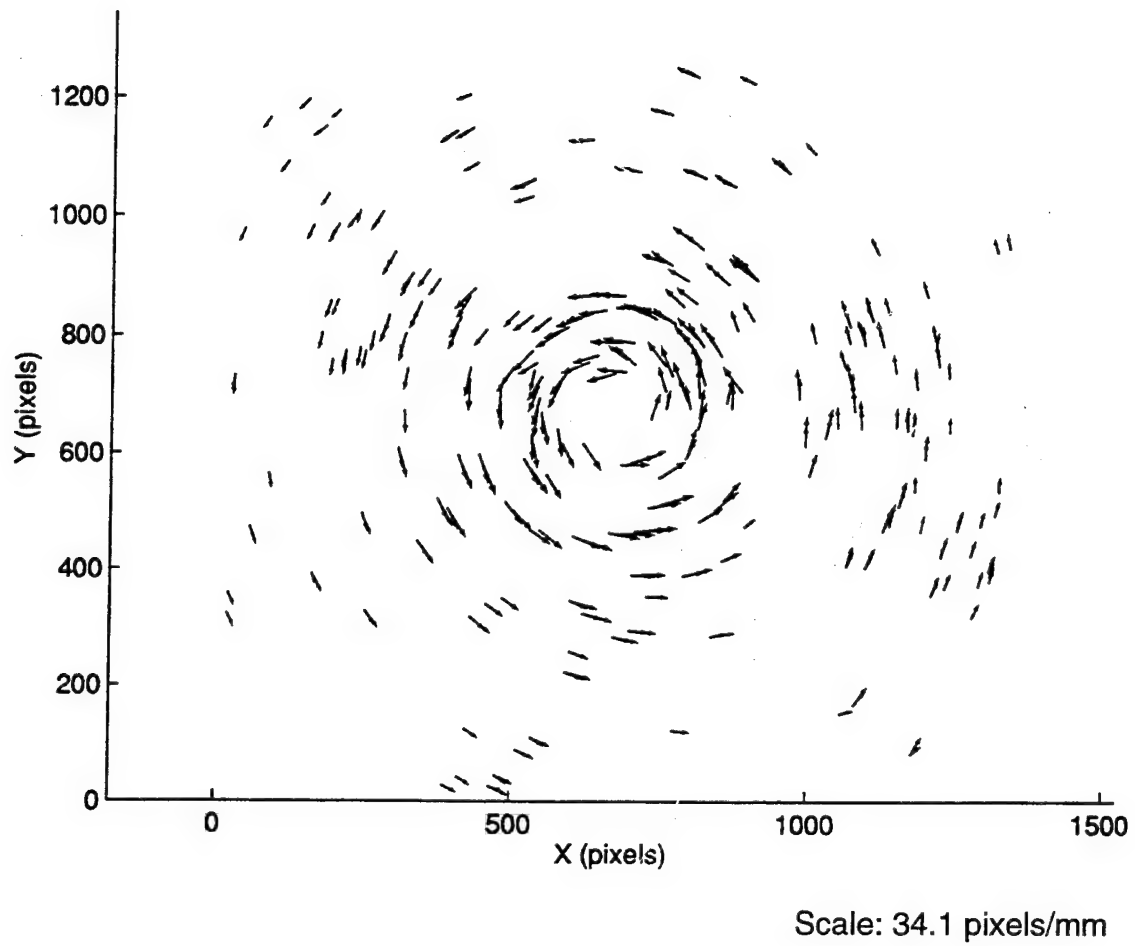


Figure 4.3: Vector map calculated from same image; $k = 0.48$, $\phi = 180^\circ$.

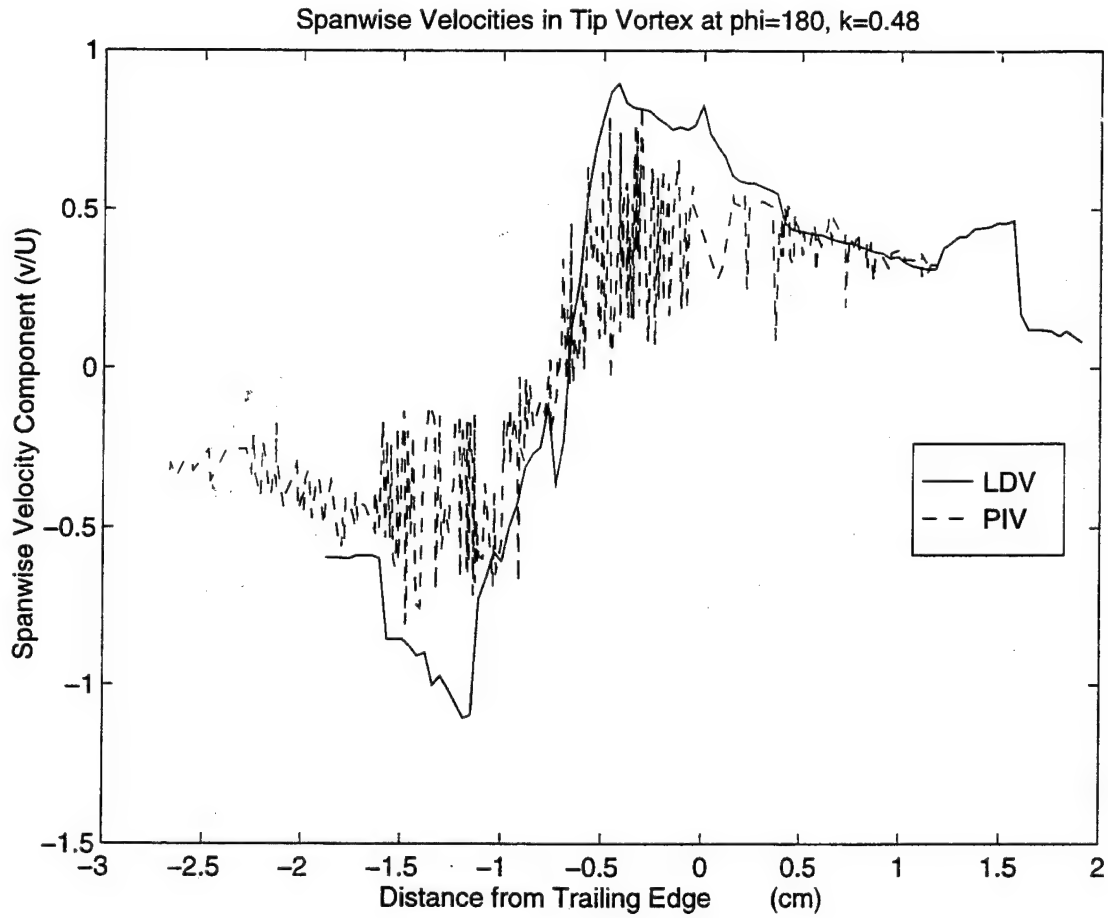


Figure 4.4: Comparison of spanwise velocity components, present data and data from Hart (1993); $k = 0.48$, $\phi = 180^\circ$.

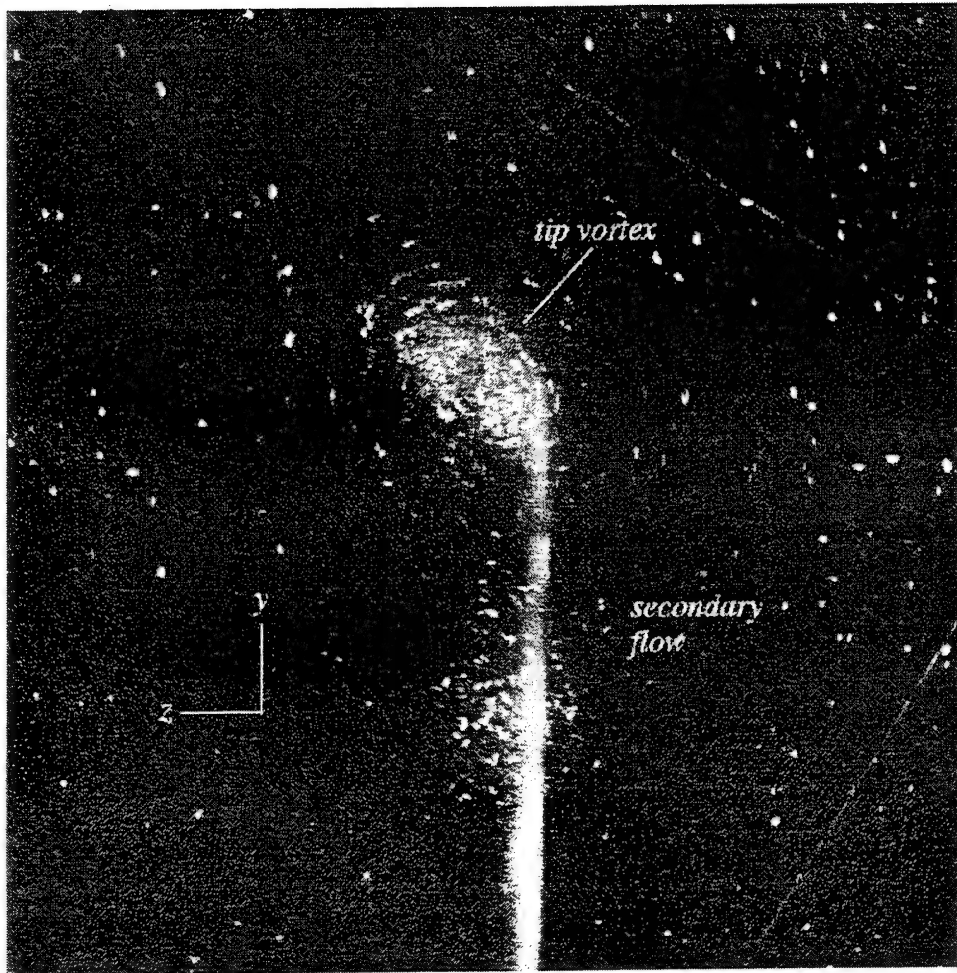


Figure 4.5: PIV image showing secondary flow; $k = 0$, $\phi = 0^\circ$.

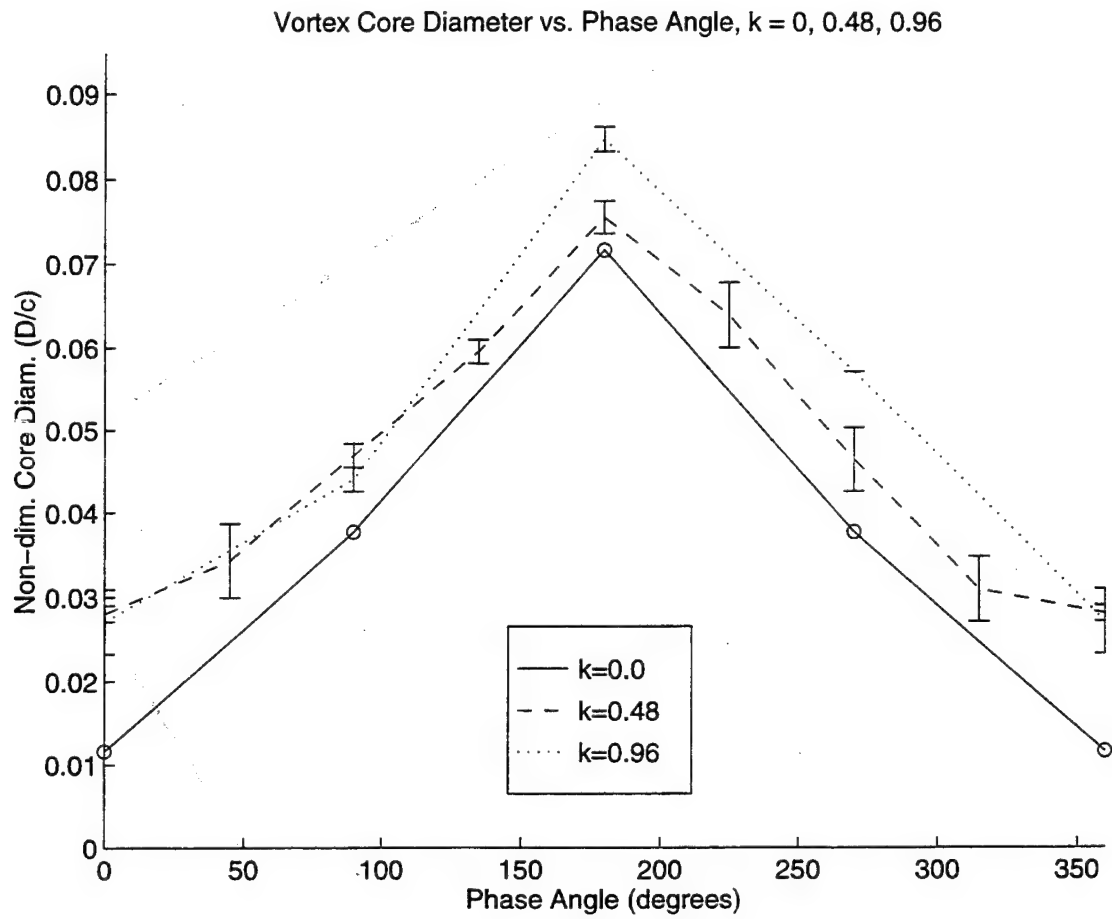


Figure 4.6: Change in vortex core diameter with phase angle; $k = 0, 0.48, 0.96$.

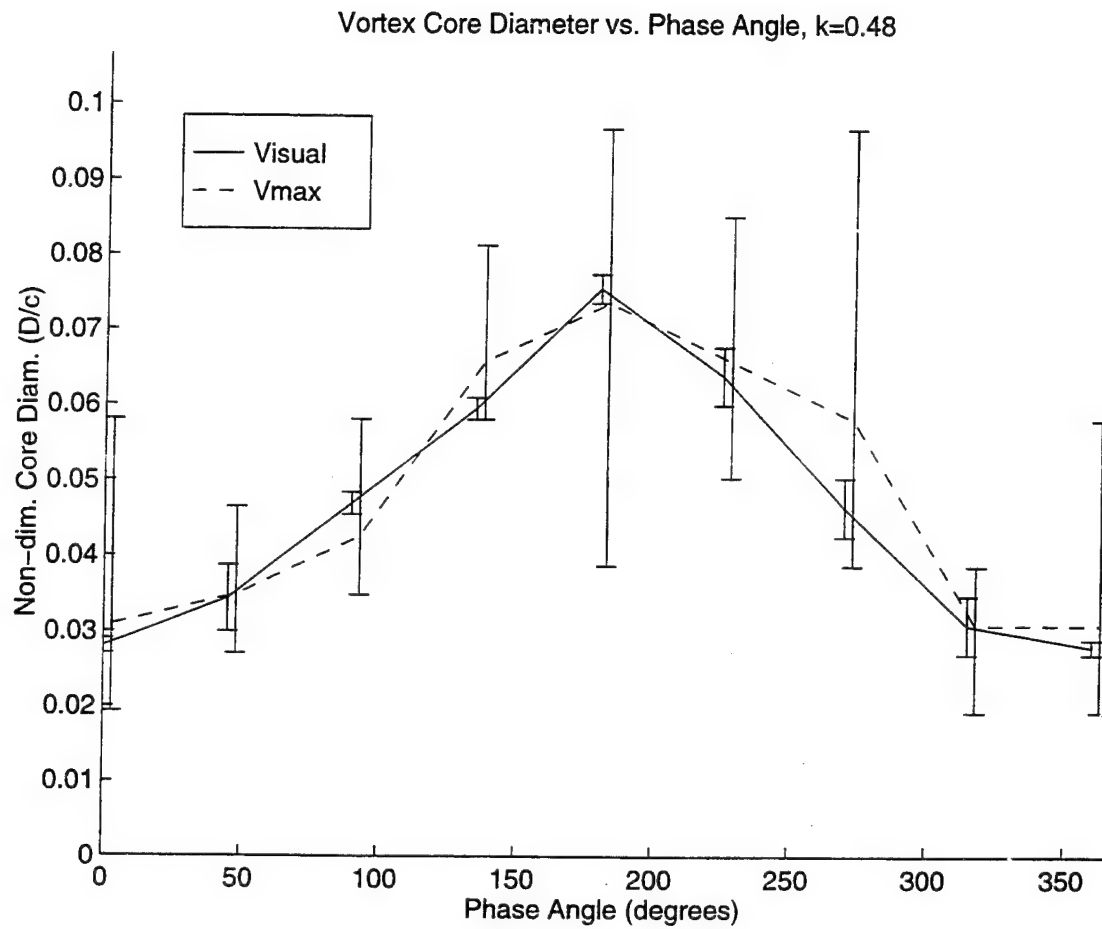


Figure 4.7: Comparison of two methods of measuring vortex core diameter; $k = 0.48$. (Phase angles of V_{max} results are artificially offset to the right for clarity.)

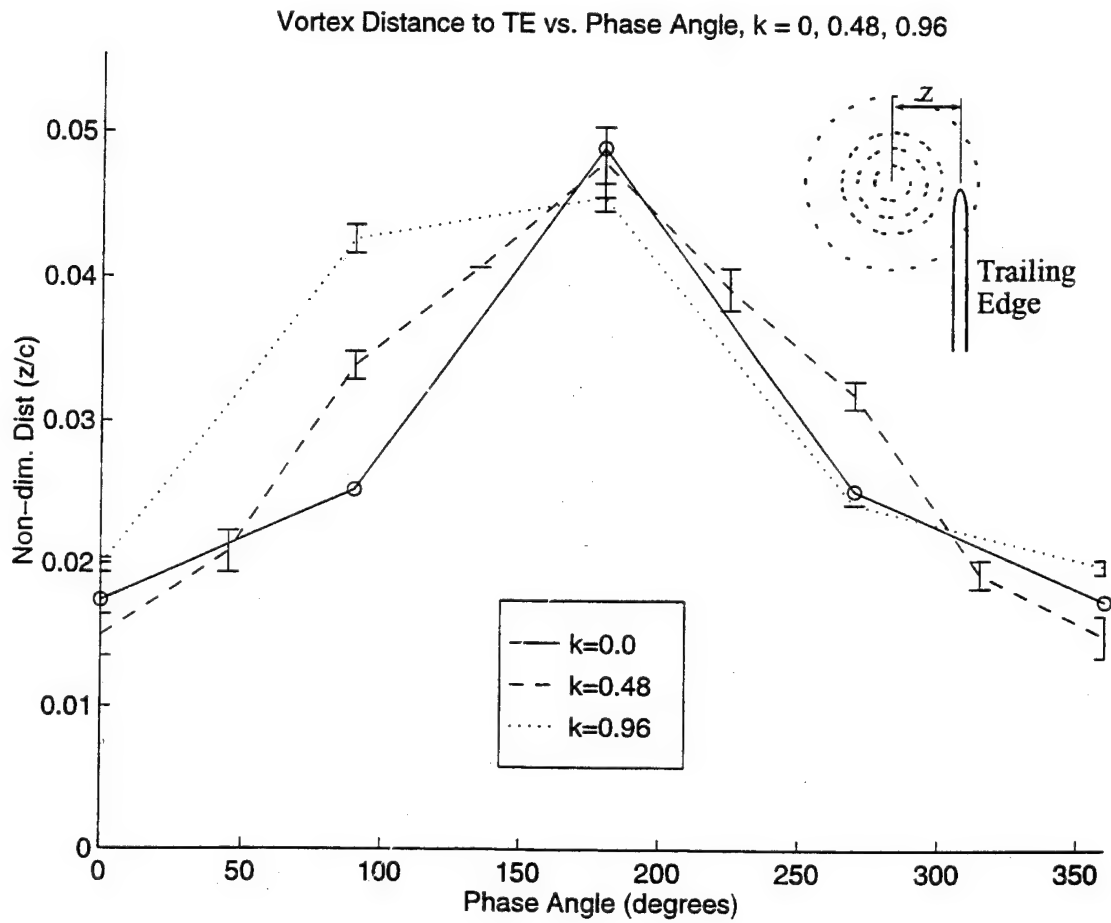
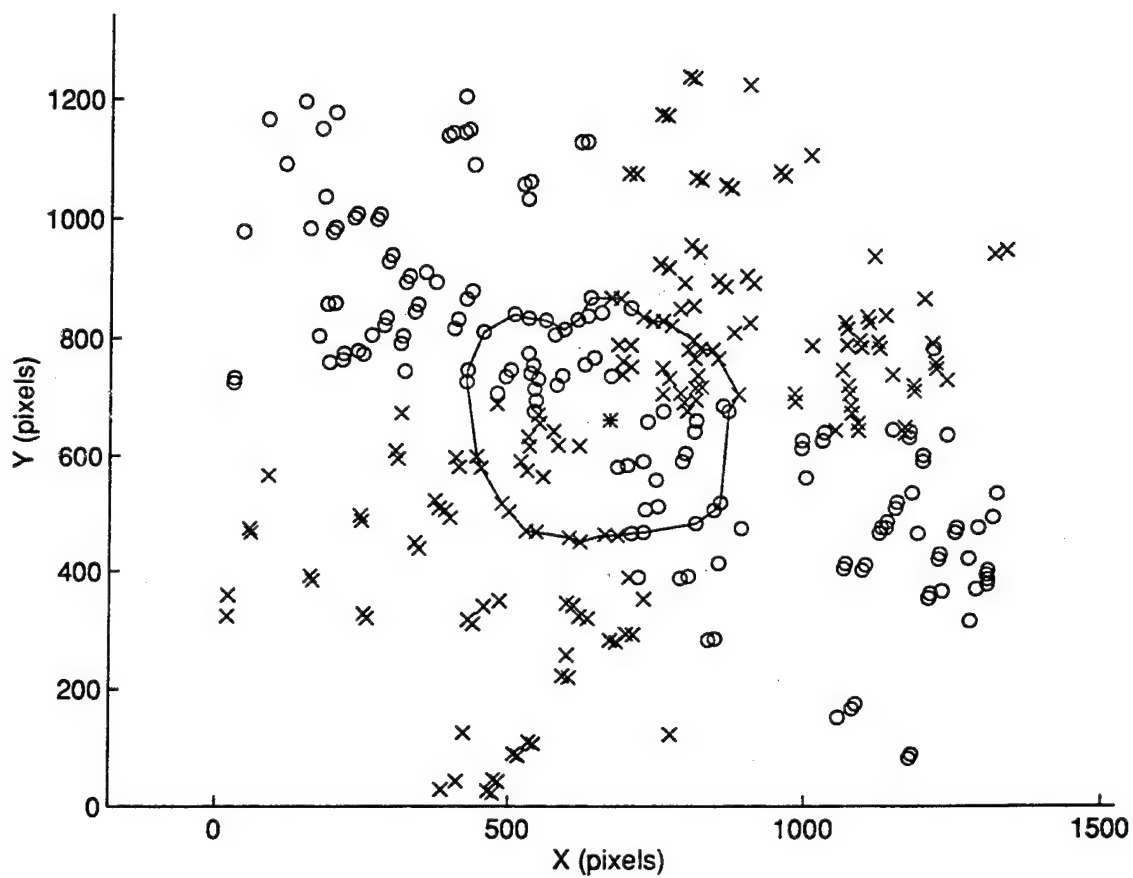


Figure 4.8: Change in vortex distance from trailing edge; $k = 0, 0.48, 0.96$.



Scale: 34.1 pixels/mm

Figure 4.9: Example of interactive contour; $k = 0.48, \phi = 180^\circ$.

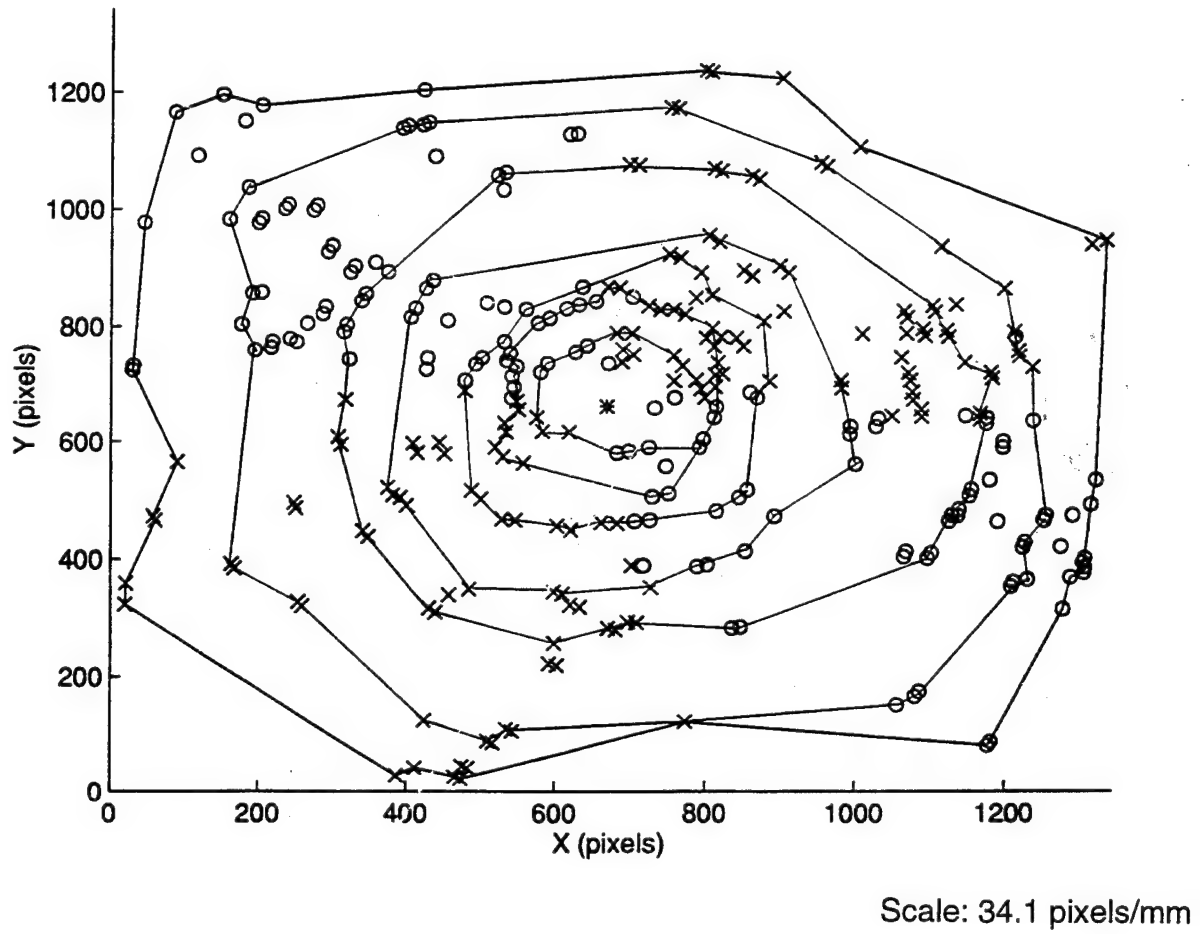


Figure 4.10: Contours used for circulation profile; $k = 0.48, \phi = 180^\circ$. (Note that axis scales are unequal.)

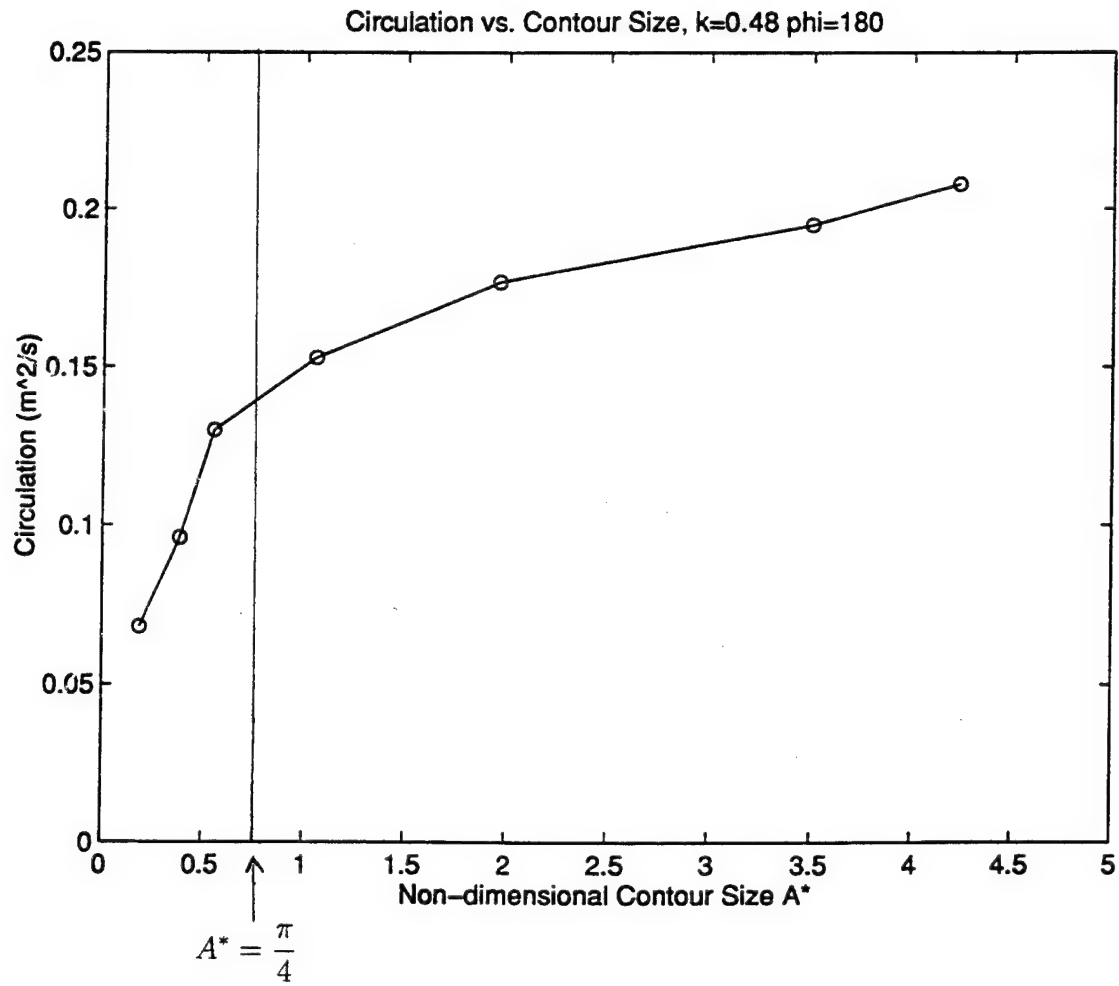


Figure 4.11: Circulation profile; $k = 0.48$, $\phi = 180^\circ$. $A^* = \frac{\pi}{4}(d/D)^2$

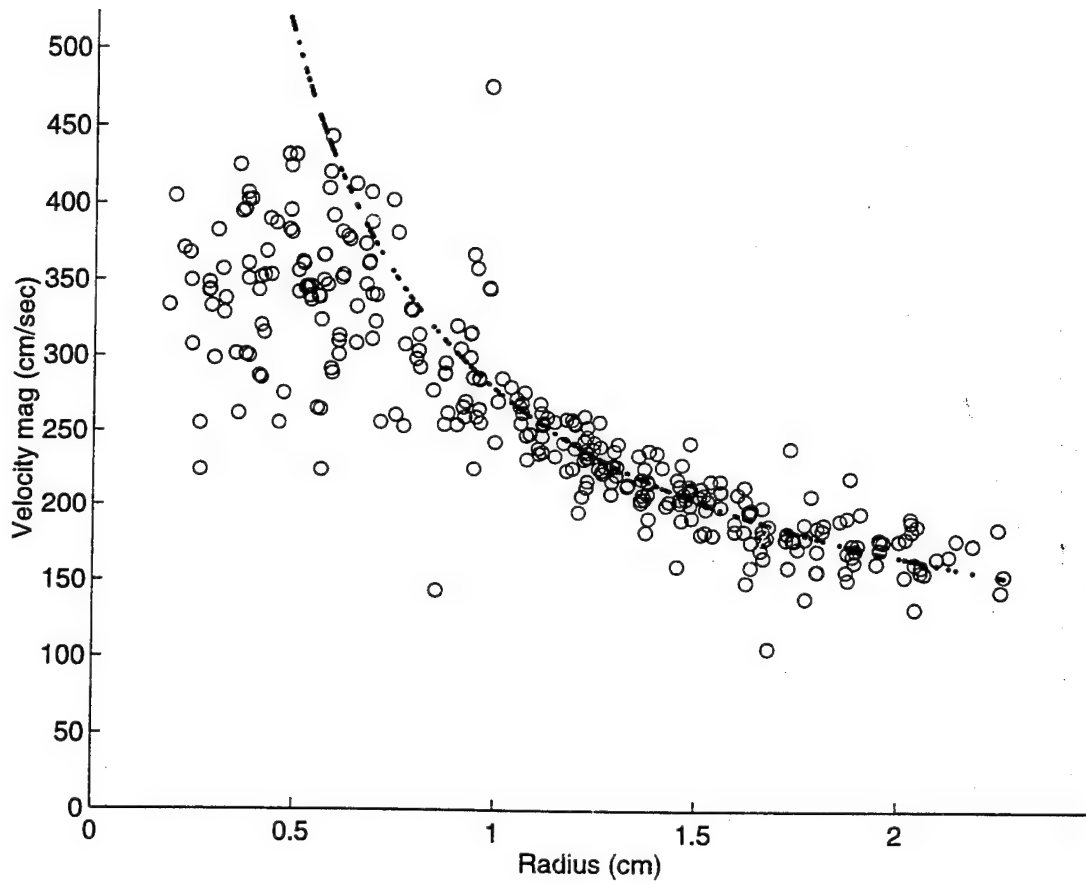


Figure 4.12: Data plotted as V vs. R . Curve is best fit to $V = C/r$; $k = 0.48$, $\phi = 180^\circ$.

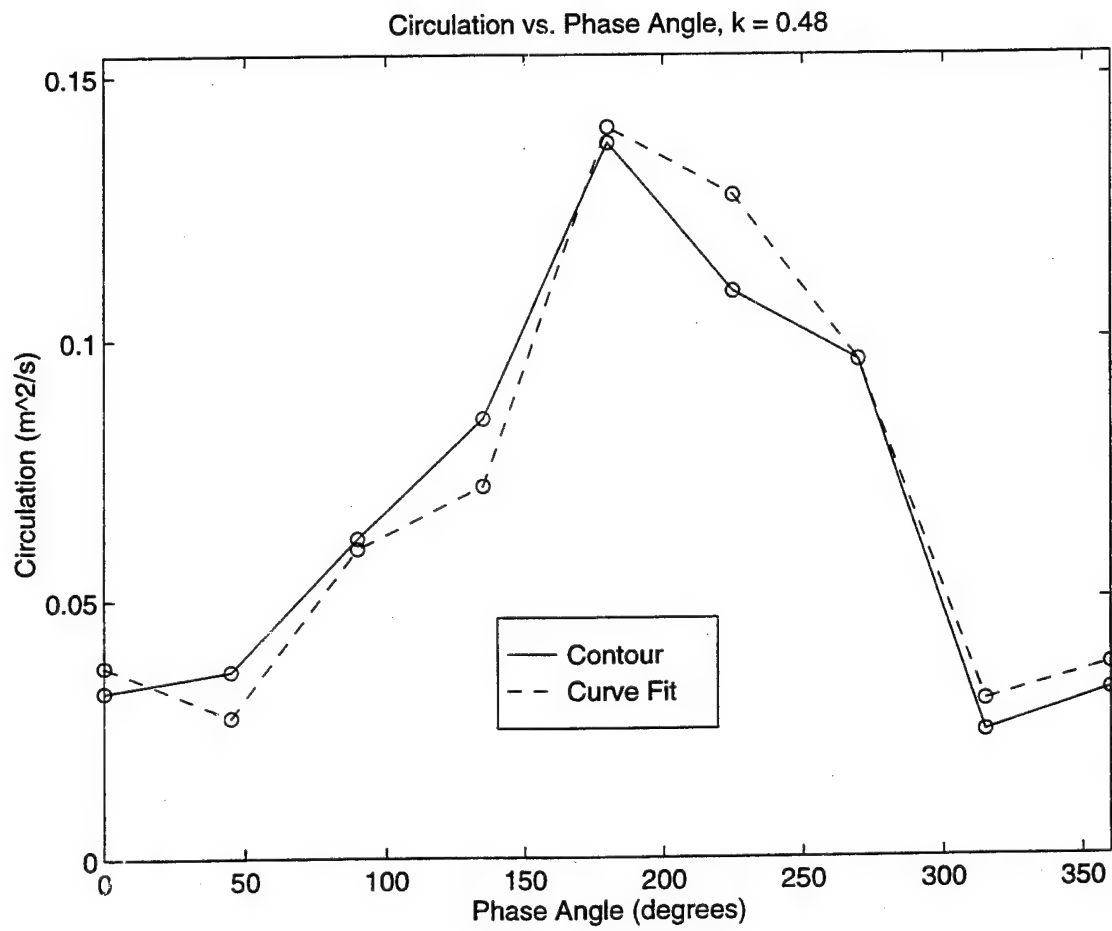


Figure 4.13: Comparison of contour integral and curve fit methods; $k = 0.48$.

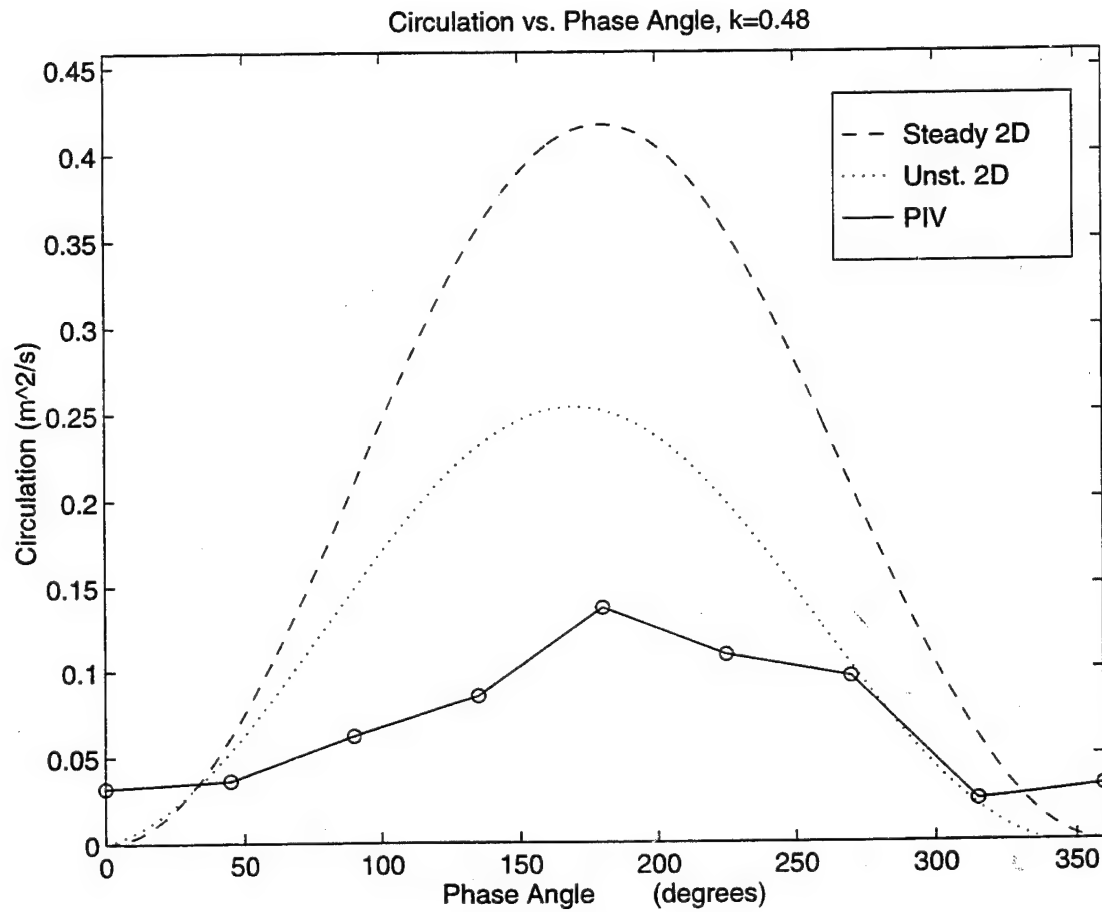


Figure 4.14: Circulation vs. phase angle, compared with 2D calculations; $k = 0.48$.

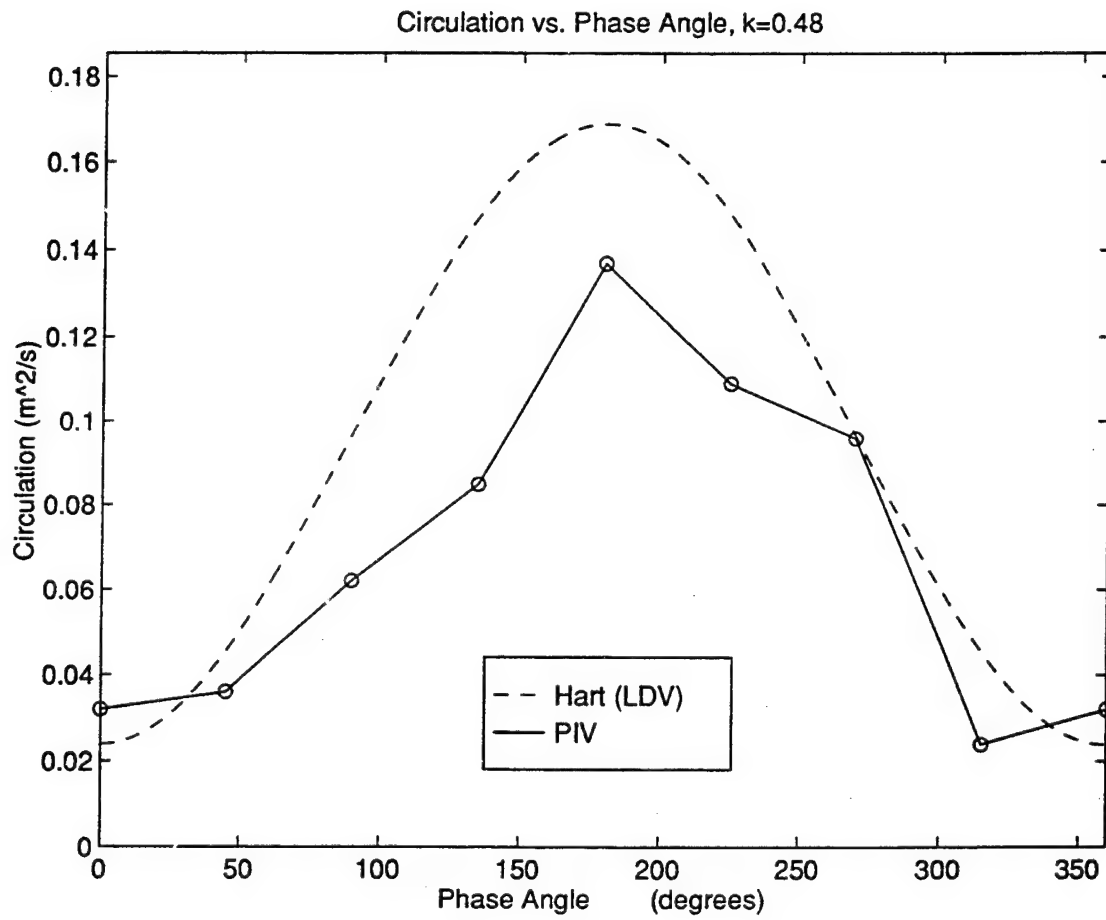


Figure 4.15: Circulation vs. phase angle, compared with Hart (1993) results; $k = 0.48$

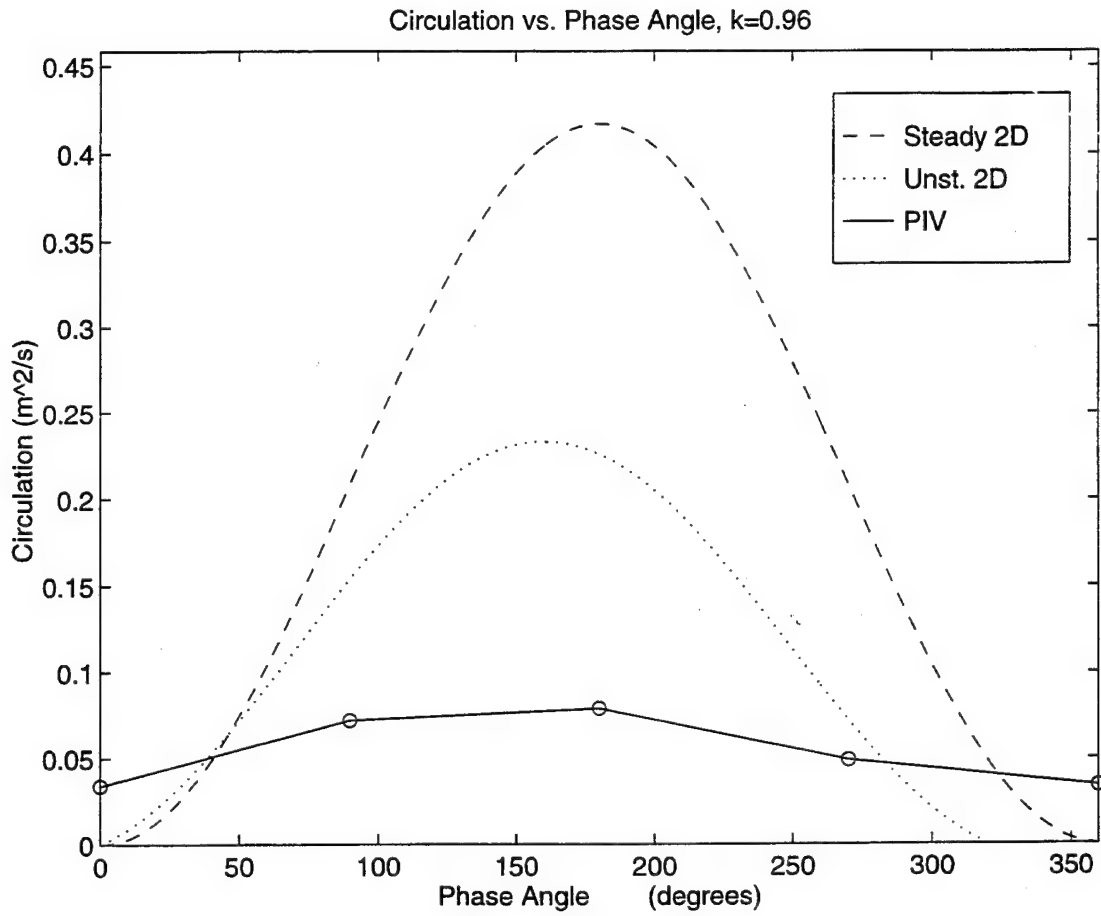


Figure 4.16: Circulation vs. phase angle, compared with 2D calculations; $k = 0.96$

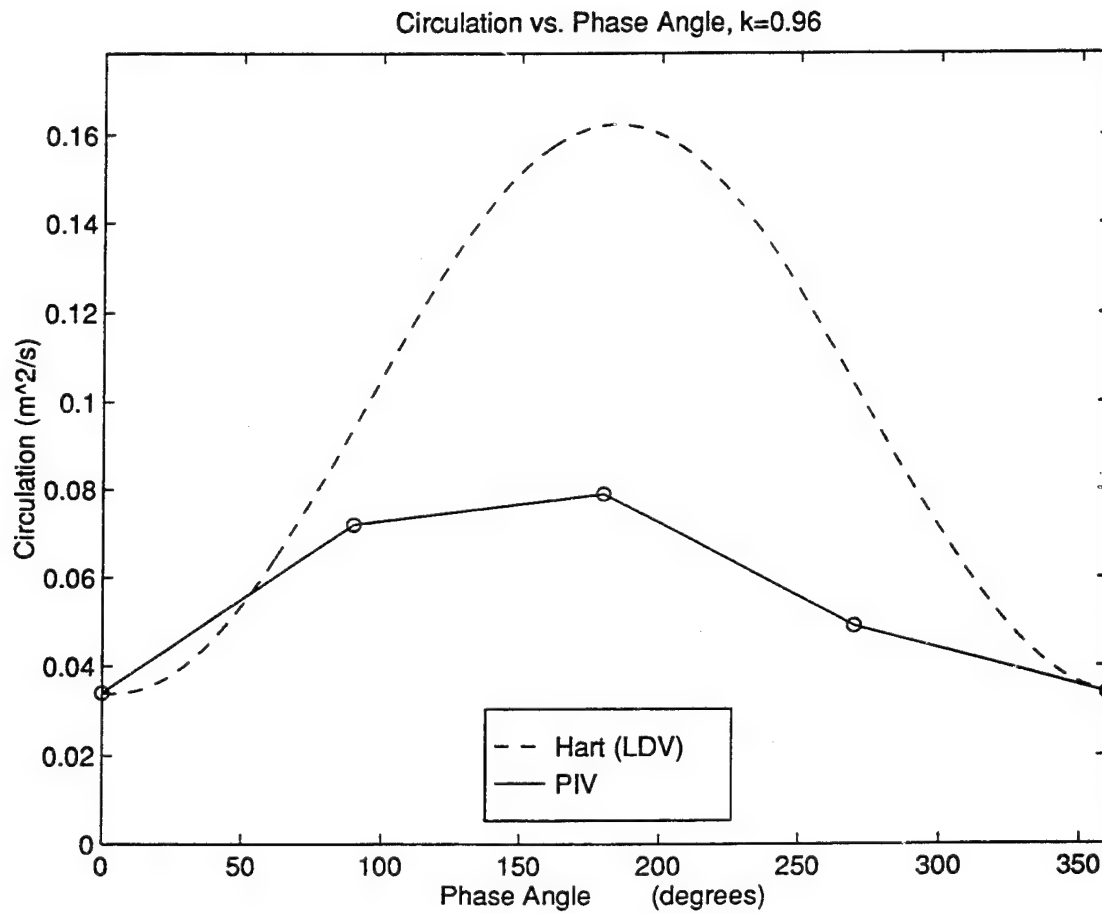


Figure 4.17: Circulation vs. phase angle, compared with Hart (1993) results; $k = 0.96$

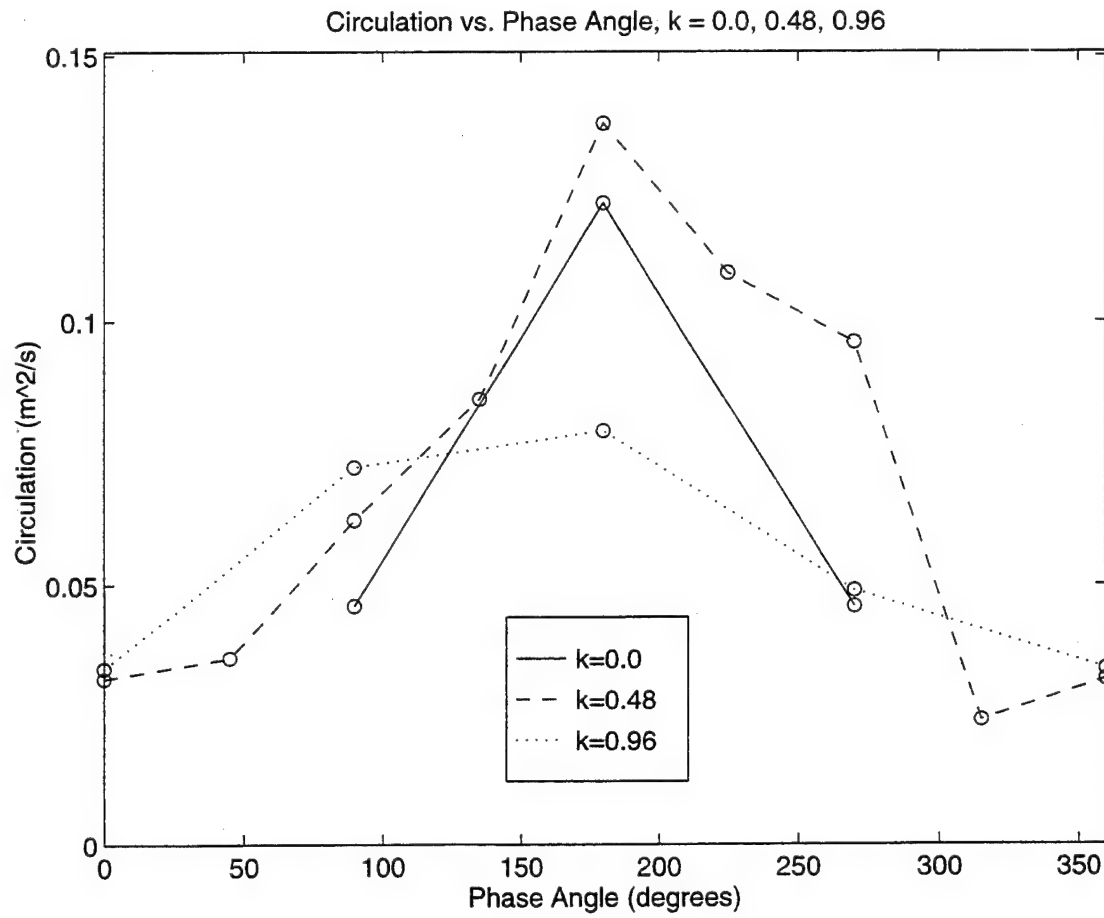


Figure 4.18: Circulation vs. phase angle; $k = 0.0, 0.48, 0.96$.

Chapter 5 Cloud Cavitation

As several researchers have pointed out (Strasberg (1977), Sharma, *et al.* (1990)), the noise from unsteady cavitation generally exceeds that of cavitation in a steady flow. The greater amplitude noise is of some concern, since it often accompanies more serious vibration problems and possibly damaging erosion. Since nearly all real flows are inherently unsteady it becomes desirable to investigate the source of this noise; identifying the flow mechanisms that produce the greatest noise is an important first step in developing ways to mitigate these effects.

The experiments described in this chapter were part of an ongoing research effort that seeks to study the cyclic cavitation process in order to determine the mechanisms responsible for cavitation noise. As described in Chapter 2, the oscillating hydrofoil apparatus was used to generate cavitation on the suction side of the foil, and photographs and high-speed movies of the cavitation were correlated with the acoustic signals produced by the cavitation. This discussion will include both detailed observations of the cavitation cycle on the oscillating foil and the conclusions drawn as to the possible causes of the various features found in the acoustic signals. One major limitation of the observations, however, is that both the photographs and motion pictures view the foil only in planform, so that the depth of the cavitation phenomena (normal to the foil surface) cannot be determined. It is hoped that future studies will include simultaneous views from two different angles for a more three-dimensional understanding of the flow.

5.1 Cavitation Cycle

Figure 5.1 demonstrates how, for one particular set of flow conditions, the cavity size changes during one oscillation cycle. Also displayed are letters which indicate

the average phase angles at which certain identifiable events were seen to occur. (See Section 2.3 for a definition of phase angle.) These events are best identified by the following chronology, which is illustrated schematically in Figure 5.2 and photographically in Figure 5.3. (Note that, while the photographs in Figure 5.3 are representative of the phenomena described here, they are not all taken with the same conditions.) As the phase angle increases from $\phi = 0^\circ$ and reaches about $\phi = 100^\circ$ (point A), the tip vortex cavity begins to form just upstream of the trailing edge. Shortly thereafter, around $\phi = 130^\circ$ (point B), a few travelling bubbles may be seen near the leading edge. Some of these collapse quickly or are swept downstream, but a small number adhere to the leading edge itself and begin to elongate in the downstream direction. (The photograph in Figure 5.3 labelled "B/C" illustrates this stage of the cavity development.) Soon these attached bubbles coalesce into a single attached cavity (point C). The cavity is mostly clear and smooth except for a few specks of froth in the closure region. (This is shown in a slightly more advanced state in photograph "D" of Figure 5.3.) Often, these frothy regions occur where two bubbles have just coalesced while forming the cavity, suggesting some link between the coalescence and the initial breakdown into bubbles.

Another interesting feature usually evident in the cavity is a crescent-shaped area in the closure region, seen in the photos labelled "G" and "E" in Figure 5.3. It appears to "enclose" the frothy regions—that is, it curves smoothly into the froth—but it is not immediately evident whether this crescent is filled with vapor or with reentrant flow. Its appearance is reminiscent of the leading-edge vortex schematic of Freymuth, *et al.* (1986b), reproduced in Figure 5.4; viewing the cavity from other angles would be necessary in order to understand the role of this crescent in the cavitation process.

The cavity continues to grow in size as the angle of attack increases. At point D, it has reached its maximum extent along the leading edge of the foil, but it continues to extend downstream; Point F indicates the phase angle at which it

attains its maximum projected area over the foil surface. The frothy regions seem to travel along the crescent closure region of the cavity, from the tip and root of the leading edge towards the region of the cavity that is closest to the trailing edge, or "maximum point." (Interestingly, the passage of the bubbles along the crescent does not generally seem to perturb its smooth surface.) The usual result is one large frothy area at the most downstream point of the cavity, which begins to extend upstream towards the leading edge in a "finger" shape. This stage in the cycle is sketched in detail by Bark and van Berlekom (1978) for several values of k (with $\sigma = 0.76$). It was also noted by Bark (1985) who called this formation "MAXP" (for "maximum point distortion"), and observed that it appeared to be related to the subsequent breakoff of a subcloud as described below.

Close examination of the footage taken during the current experiments revealed the following: The region from which the MAXP extends consists partly of froth that has collected from the outer portions of the cavity (i.e. near the tip and base), and travelled along the crescent; the edge of the bubbly region then curves sharply upstream towards the leading edge as shown in Figure 5.5. From within this bubbly portion of the cavity, a sub-section of the froth may begin to protrude away from the foil surface (point E, see also photograph "E" in Figure 5.3), often sending out tendrils of bubbly vortex loops that make it look like a tangled ball of string. This "subcloud" may be any shape, but is often fairly spherical (as in the "ball of string" formation). It is difficult from the planform view to be certain, but it appears that the froth is thickening considerably; the formation of the subcloud may be due to the outer flow breaking off a portion of this froth as a separate structure.

Meanwhile, as the MAXP approaches the leading edge, either of two things may happen:

- The froth may expand all the way to the leading edge, and tear away the entire cavity. In this case, the previously smooth cavity surface becomes striated and then disintegrates into tiny bubbles as it detaches from the

surface.

- The froth may reach almost to the leading edge, and then appear to retract from it slightly. The smooth leading edge cavity is then split, with the downstream portion being torn away by the froth and usually convected into a large cloud of small bubbles along with the froth. A narrow remainder of the smooth cavity remains attached to the leading edge for a moment longer, before dissolving into fairly sparse bubbles which quickly disappear.

In either case, point "G" denotes the point at which the smooth portion of the cavity begins to detach from the leading edge; several researchers (such as Franc and Michel (1988)) have speculated that this detachment occurs as a result of laminar separation of the boundary layer. Kita, *et al.* (1994) found that the tip vortex flow tended to suppress boundary layer separation; the PIV results discussed in Chapter 4 show that the tip vortex is fairly weak by this stage of the process, which may also contribute to the detachment of the cavity.

By this time the subcloud is usually fully detached from the frothy region (point H), and has begun to convect downstream, at a rate somewhat smaller than the freestream velocity (as noted by Kubota, *et al.* (1989)). The remainder of the cavity then collapses into a second cloud (point I; see also photograph "T" in Figure 5.3), which is, in general, less coherent than the subcloud. It is swept downstream following the last traces of the collapsed subcloud. In some cases, the cloud generated by the collapse of the main cavity disappears while the subcloud is still extant (point J). Meanwhile, the tip vortex cavity, which had become thick as the cavity was growing, now begins to elongate and become thinner, and soon detaches (marked by point K; the corresponding photograph "K" in Figure 5.3 shows that the subcloud has nearly reached the trailing edge of the foil at this point). Both clouds may collapse nearly simultaneously, or at clearly distinct phase angles in the oscillation cycle, depending on the conditions of the flow. When they collapse separately, the acoustic signature may reflect

this by showing two distinct sound bursts in the collapse region of the cycle (see next section). Finally, point L indicates the phase angle at which the foil surface becomes completely clear of bubbles. The cycle then repeats itself.

In Figure 5.6, cavity sizes for four different cavitation numbers are plotted. The cavity size and the growth process change with cavitation number. For the purposes of the present measurements, the cavity was considered not to exist until the initial travelling bubbles and isolated small attached cavities finished coalescing into a single coherent cavity attached to the leading edge. Then, when the cavity began to break up during the collapse phase, the whole projected area of cavity and froth was counted in the cavity area until the subcloud was fully detached, at which point the "cavity size" was considered to include only the remaining attached cavity but not the subcloud. Thus the cavity area curve will tend to decrease sharply when the subcloud breaks off.

The reduced frequency is $k = 0.74$ for all four cases in Figure 5.6. As might be expected, the maximum cavity size increases as the cavitation number is decreased, but it is also interesting to note how the shapes of the curves change with σ : In all cases, a single coherent attached cavity is achieved at approximately the same phase angle, but the maximum cavity area occurs much later for the lower cavitation numbers. At $\sigma = 1.34$, the cavity size decreases rapidly during collapse as a result of the formation and breakoff of a large subcloud. In contrast, no distinct subcloud was observed at $\sigma = 1.53$. Furthermore, at the two lowest cavitation numbers ($\sigma = 0.88$ and $\sigma = 1.15$) there is a marked, sudden increase in the cavity area just before the maximum is reached; this seems to mark the beginning of an explosive pre-collapse phase. Figure 5.6 also depicts graphically the phase lag noted by Hart (1993) between the motion of the foil and the extent of the attached cavity. He noted that this phase lag increased as the reduced frequency of oscillation increased; this will also be seen shortly as the present results are discussed.

Figure 5.7 presents the average phase angles at which the identified events

occur during the cavitation cycle, and shows how those occurrence times change with cavitation number. (Phase angle values were averaged over ten cycles each for all cases except $\sigma = 1.53$.) Arrows are drawn through the markers to clarify the direction of change. In general, the changes are not surprising. At lower σ , the cavitation (including the tip vortex cavity) tends to begin earlier and to last longer. In a few cases, however, there is unexpectedly little variation with σ . For example, while travelling bubble cavitation occurs earlier at lower cavitation numbers, the point at which it coalesces into a single coherent cavity attached to the leading edge is reasonably constant, as is the phase angle at which the cavity first reaches its maximum extent along the leading edge. There is also remarkable consistency in the phase angle at which the subcloud (for cases where one appears) first becomes clearly discernible. From the arrows, it seems clear that events D and E (maximum leading edge extent and formation of subcloud) represent a sort of climax of the cavitation process: Events before this point get earlier with decreasing cavitation number, and events after it get later. This suggests that the major effect of cavitation number is to "stretch" the cavity, both spatially and temporally, with the subcloud formation marking the apex of the cavitation cycle.

One motion picture sequence was taken at a lower reduced frequency. Figure 5.8 compares the cavity size variations for the two different reduced frequencies at the same cavitation number. Event times are included in the figure in order to illustrate how they changed with reduced frequency. It is interesting to note that the cavity size increases only slightly for the lower reduced frequency, and it begins and ends at nearly the same phase angle. The shapes of the curves, however, are strikingly different for the two values of k shown. On the $k = 0.56$ curve, beginning at point D (the point in the cycle where the cavity has reached its maximum extent along the leading edge of the foil), the cavity area suddenly increases sharply as the cavity expands in the downstream direction. Examining the movie footage it appears that, unlike the $k = 0.74$ case where the froth is mostly contained within the smooth curve of the closure region, the $k = 0.56$ cav-

ity has froth that extends beyond the basic cavity shape, reaching downstream and sometimes even ejecting a few bubbly vortex tendrils before breaking off a large subcloud. For these conditions, it appears that the frothy, collapsing portion of the cavity reaches further upstream before the main cavity begins to detach from the leading edge (see relative positions of events G and H), in contrast to the higher reduced frequency case where the cavity detaches from the leading edge and collapses to meet the frothy region. The end product of this collapse is two clouds; the large subcloud and the cloud-like remains of the collapsed main cavity are both convected downstream and dissipate at approximately the same rate.

In addition, it should be noted that nearly all the events indicated by the letters in the figure may be seen to occur later for the lower reduced frequency, not only those associated with the growth of the cavity but also those associated with its collapse. (The exception to this pattern is event H indicating the breakoff of the subcloud, which occurs earlier due to the collapse of the main cavity as described above.) This concurs with the increasing phase lag observed by Hart (1993), as mentioned previously. It is interesting to contrast, however, with the changes with cavitation number shown in Figure 5.7, where the cavitation process began earlier for decreasing cavitation number, but ended later. Changes in the process with decreasing cavitation number, then, seem to be guided by the greater tendency toward cavitation; changes with decreasing reduced frequency, however, appear to be driven more by the phase lag introduced by the coupling of the fluid with the oscillation of the foil.

5.2 Cavitation Acoustics

The violence with which cavitation collapses is well documented (Bark and van Berlekom (1978); Kato (1985); Ye, *et al.* (1989); Soyama, *et al.* (1992)), and, in fact, the noise is readily apparent to the most casual visitor to the facility. Figure 5.9 shows typical raw data from a single oscillation cycle of the hydrofoil

for the conditions noted in the caption, acquired from the externally-mounted hydrophone as described in Chapter 2. (The sinusoidal curve represents the foil angle of attack, increasing from $\alpha = 0^\circ$ to $\alpha = 10^\circ$ and then back to $\alpha = 0^\circ$.) Even without filtering out the various mechanical resonances inherent in the facility, some of the features of the cavitation noise are evident. Standing out from the background noise, a large high-amplitude, high-frequency burst may be seen between phase angles of 340° and 355° ; that is, in the last 3% of the oscillation cycle, just before the foil returns to zero angle of attack. Less prominent, but still visible, is a low-amplitude high-frequency burst at around $\phi = 130^\circ$, where the angle of attack is about 8° and increasing. Using a digital high-pass filter algorithm (as discussed in Section 2.5.2) most of the non-cavitation noise was then filtered out of the data, resulting in signals such as the one that appears in Figure 5.10.

The acoustic signals were analyzed in two ways. First, the overall "noise level," or acoustic intensity, was calculated for each set of conditions, in order to gain a perspective on the variations of the noise with reduced frequency and cavitation number. Second, the shapes of the individual signals were correlated with high speed motion pictures of the cavitation, in the hopes of identifying features in the cavity growth and collapse process which are responsible for the various features in the acoustic signature.

The measured acoustic intensity, p_A , is defined by

$$(p_A)^2 = \frac{1}{T} \int_0^T (p(t) - \bar{p})^2 dt, \quad (5.1)$$

and a dimensionless intensity is then defined as

$$p_A^* = \frac{p_A \mathcal{R}}{\frac{1}{2} U^2 c}, \quad (5.2)$$

where \mathcal{R} is the distance from the cavitation to the hydrophone, ρ is the density of water, U is the freestream velocity, and c is the foil chord length. The quantity p_A^* provides a normalized measure of the strength of the noise produced by the

cavitation. Figure 5.11 shows how this variable changed with reduced frequency, for three different values of cavitation number. (Here it should be noted that the acoustic intensity was calculated using unfiltered data.) The peaks in acoustic intensity corresponded very consistently with conditions under which the cavitation was heard to make a loud report or “bang” during collapse.

Each curve in Figure 5.11 contains two peaks, marked with arrows. As the reduced frequency increases, the value of the acoustic intensity is seen to increase, then decrease, then increase again; this may be related to qualitative changes in the cavity collapse process for certain ranges of reduced frequency. These peaks tend to increase in magnitude, and, for the cavitation numbers shown, also appear to shift toward lower reduced frequencies, with decreasing cavitation number. Between the cavitation numbers of about 1.3 and 1.5, there are distinct changes in the cavitation: The size of the cavity increases by almost 100% (from 1/4 chord to 1/2 chord) as the cavitation number is reduced, and the “ball of string” subcloud formation now appears during the collapse phase, detaching from the main cavity and travelling separately downstream. This is in contrast to the higher cavitation number process, where the cavity collapses into a crescent-shaped frothy region which dissipates quietly. At the lower cavitation numbers (depending on reduced frequency) a “bang” can be heard as the cavitation collapses, suggesting that the existence of a distinct subcloud during collapse may be associated with the “bang.” The higher cavitation number sequence does sometimes evidence tangled vortex tendrils within the frothy region, but there is no clear detachment of a separate formation. This would satisfactorily explain the very low acoustic intensities for $\sigma = 1.45$ as shown in the figure.

The presence of two peaks is not easily resolved, however. A single acoustic peak would reflect the observations of Stern (1986) and Hart (1993) that the cavitation response of greatest amplitude (i.e. the largest cavities) occurs when the forcing frequency of the foil matches the natural shedding frequency of the attached cavities. Two possible scenarios come to mind:

- One of the peaks may be an artifact of the experimental setup (this seems unlikely since such resonance would not explain the shift with cavitation number).
- There may be flow mechanisms which can increase the noise output other than the extent of the attached cavity. For example, the formation of the subcloud seems to be more dependent on the shape of the cavity than on its size.

It is also interesting to note that later experiments by Reisman, *et al.* (1994) using the same foil but with a larger mean angle of attack, did not find the same trends. The result is that the noise does not increase monotonically with decreasing cavitation number, but exhibits a more complex relationship which is not well understood at this time. The higher angle of attack tends to increase the total cavity size (for $\sigma = 0.9$ the sheet cavity not only covered the entire foil surface but extended beyond the trailing edge); this may alter the cavitation number at which the noise peaks.

The acoustic signals were also compared with the results obtained from the motion picture sequences. Figure 5.10 shows an oscillation cycle from one of the five cases examined (the acoustic data here has been high-pass filtered as described earlier), along with a curve showing the corresponding cavity area for the same cycle. Event times are also indicated. The distance between markers on the cavity area curve represents the time between one movie frame and the next (approximately 2 msec). The time required for the cavitation sound to travel from the trailing edge of the foil to the hydrophone is approximately 1/6 of the time between frames, which on the scale of the graph is negligible. Thus the fact that the main burst in the acoustic signal begins at the same phase angle as event I (see corresponding photo in Figure 5.3) means that the collapse of the cavity itself does not seem to contribute directly to the noise produced by the cavitation.

In fact, the cavity size curve clearly shows that the main cavity ceases to exist

as a coherent attached cavity almost as soon as the burst begins. The events contained within the main burst are I, K, and J: main cavity turned to froth, tip vortex cavity detached, and main cavity dissipated leaving subcloud, respectively. Since it is unlikely that the detachment of the tip vortex is a major contributor to the acoustic signal, we are forced to conclude that it is the process of dissipation of the remaining froth that creates the major burst of noise in this cycle. This agrees with the observation of Shen and Peterson (1980) that "the peak amplitude of the noise occurs after the sheet cavitation has disappeared," and indeed they make the same conclusion about the source of the noise. At point J the main cavity is completely gone, leaving only the subcloud visible; the remaining portion of the burst thus may correspond to the subcloud beginning to collapse as it is swept to the trailing edge of the foil. Note that the subcloud does not fully clear the trailing edge until point L, but that the burst amplitude drops off as the foil again nears zero angle of attack.

It is interesting to compare the results for the noise from this type of cavitation with previous results for single travelling bubbles. Figure 5.12, from Reisman, *et al.* (1994), illustrates the approximate relations between cloud cavitation noise, the impulses observed by Kuhn de Chizelle, *et al.* (1994) for single travelling bubbles, and the impulse magnitudes predicted by the Rayleigh-Plesset equation for a spherical bubble. From this figure, it is evident that the noise generated by cloud cavitation is several orders of magnitude larger than the sound level resulting from single travelling bubble cavitation. The impulses generated by some clouds are even greater than the theoretical prediction for a single spherical bubble of the same maximum volume. The figure suggests that clouds can be even more effective noise sources than single bubbles of the same volume. A possible explanation for this is the formation of an inwardly propagating shock wave within the collapsing cloud as originally suggested by Mørch (1980, 1981) and recently demonstrated theoretically by Wang and Brennen (1994). One particularly interesting result in the latter paper is that the overall size of the cloud may not change much during

the collapse process (as the shock is propagating). Rather, the shock induces changes in the sizes of individual bubbles within the cloud as it passes, with the radius of the cloud itself remaining nearly constant. It was noted during the current experiments that the clouds associated with the greatest acoustic noise do persist longer than other clouds; while this neither confirms nor disproves the propagating-shock theory, it is clear that the production of a distinct subcloud is related to the production of greater cavitation noise.

The source of the smaller high-frequency burst in the acoustic signal of Figure 5.10, occurring just after $\phi = 120^\circ$, is less easily discerned. Unfortunately the resolution of the high-speed movies is not sufficient to determine unequivocally what action in the cavitation caused the noise; one movie frame occurs just before the middle of the burst, the other just after the burst ends. The only change between the two frames is the disappearance of a few travelling bubbles on the surface of the foil. This leads to the speculation that the collapse of some of these travelling bubbles may have generated this small burst.

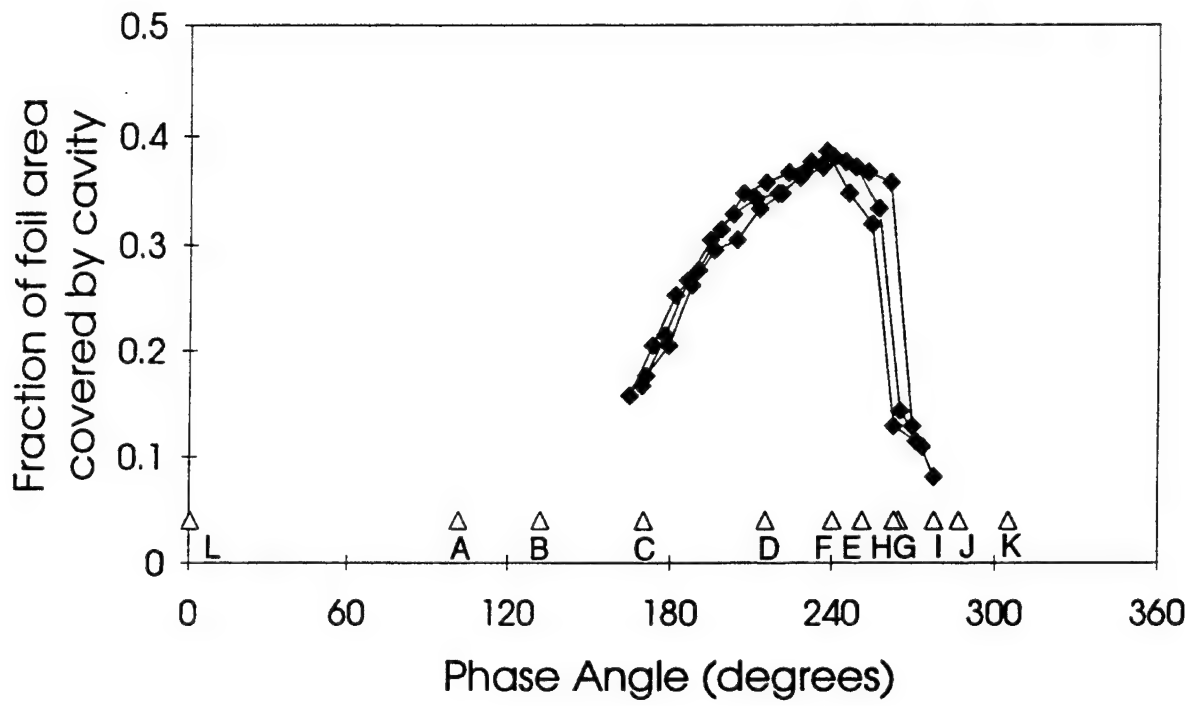


Figure 5.1: Cavity size plotted against phase angle, for reduced frequency $k = 0.73$ and cavitation number $\sigma = 1.34$.

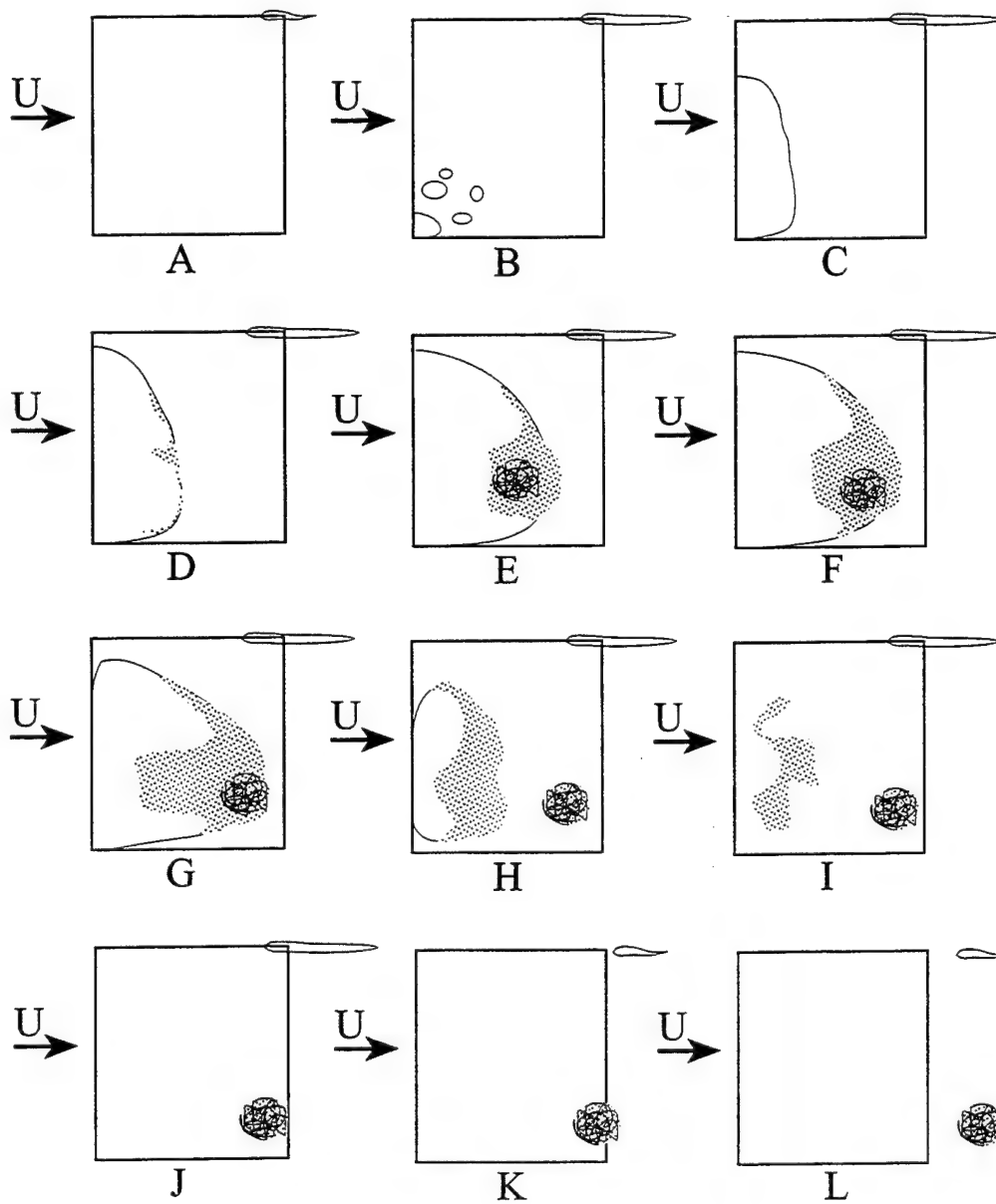
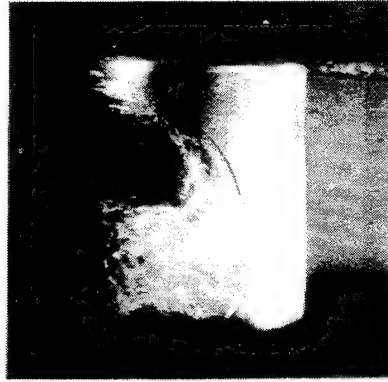


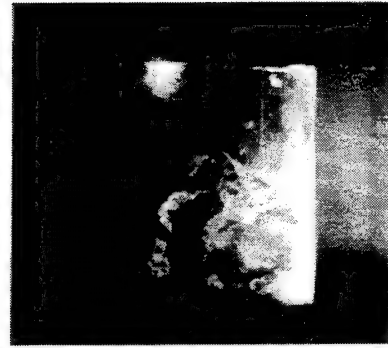
Figure 5.2: Schematic representation of selected events in a typical cavitation cycle. See next figure for photographs.



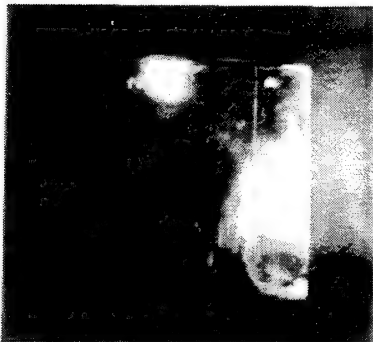
D. ($\sigma = 1.15$, $k = 0.74$)



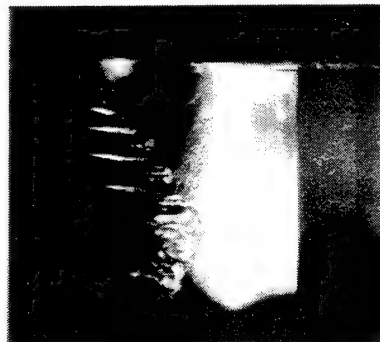
G. ($\sigma = 1.15$, $k = 0.74$)



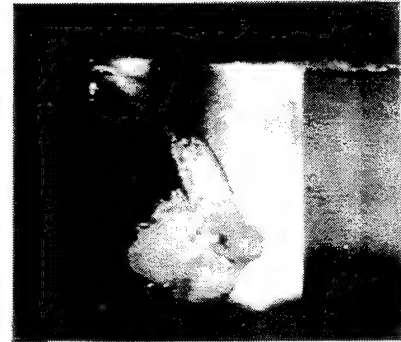
I. ($\sigma = 1.15$, $k = 0.74$)



K. ($\sigma = 1.15$, $k = 0.74$)



B/C. ($\sigma = 0.88$, $k = 0.75$)



E. ($\sigma = 0.88$, $k = 0.75$)

Figure 5.3: Photographs of selected events in the cavitation cycle.

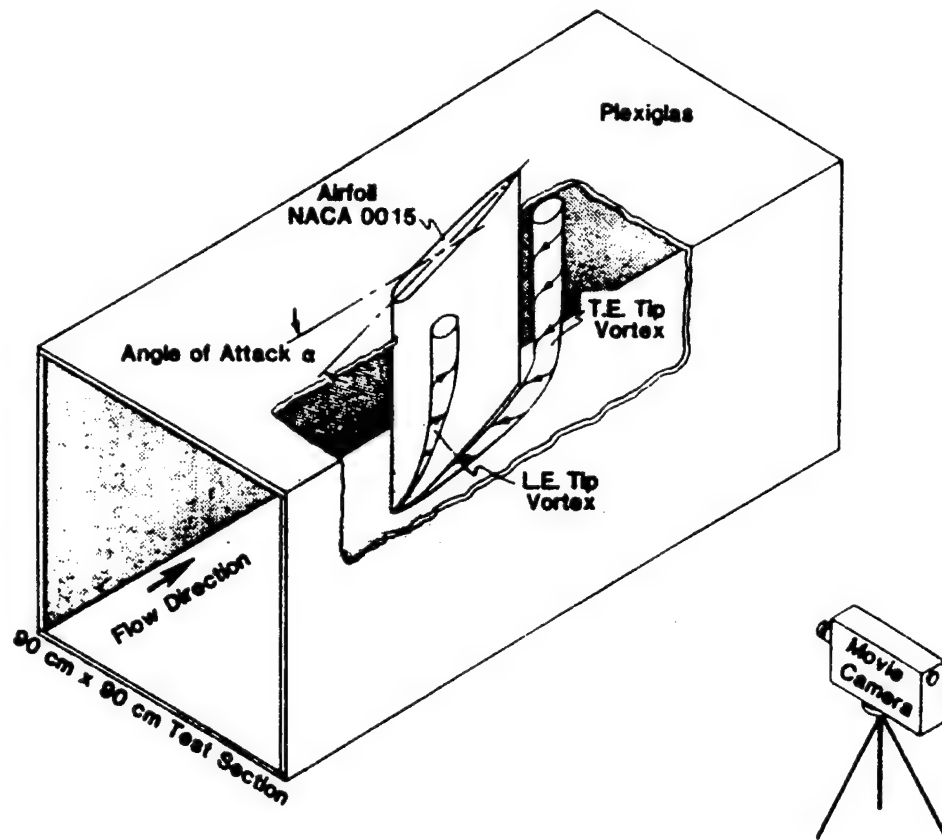


Figure 5.4: Schematic of starting and leading-edge vortices, from Freymuth, *et al.* (1986b).

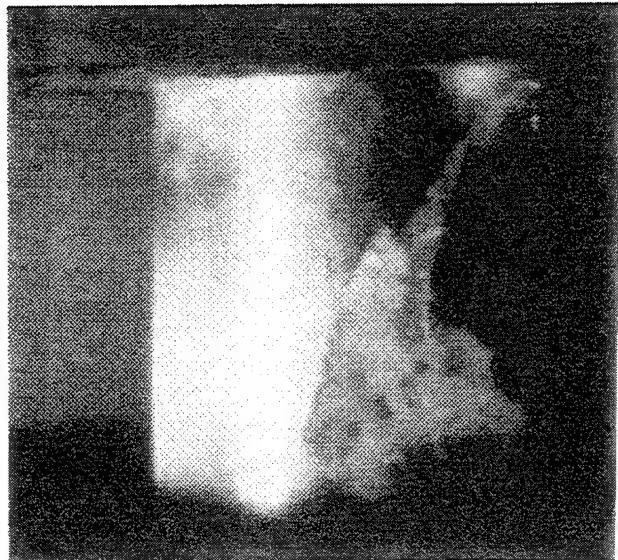
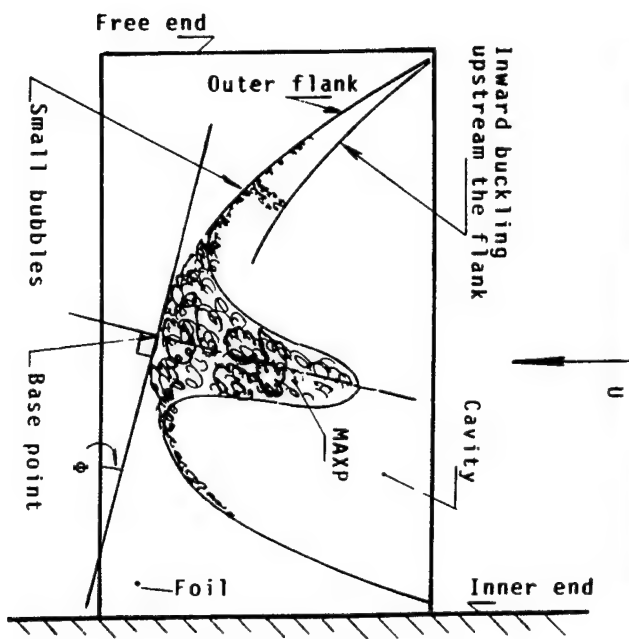


Figure 5.5: Formation of MAXP distortion—Sketch from Bark (1985) and photograph from current experiments.

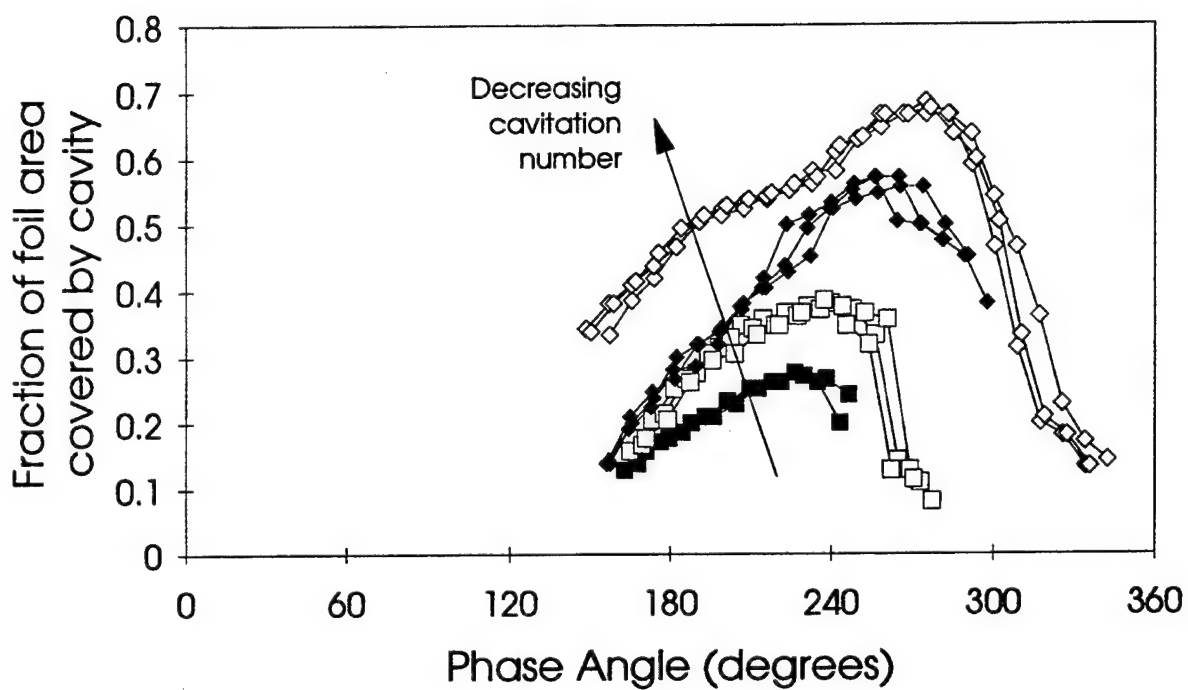


Figure 5.6: Cavity area plotted against phase angle, for reduced frequency $k = 0.74$ and four cavitation numbers. ($\blacksquare \sigma = 1.53$, $\square \sigma = 1.34$, $\blacklozenge \sigma = 1.15$, $\diamond \sigma = 0.88$)

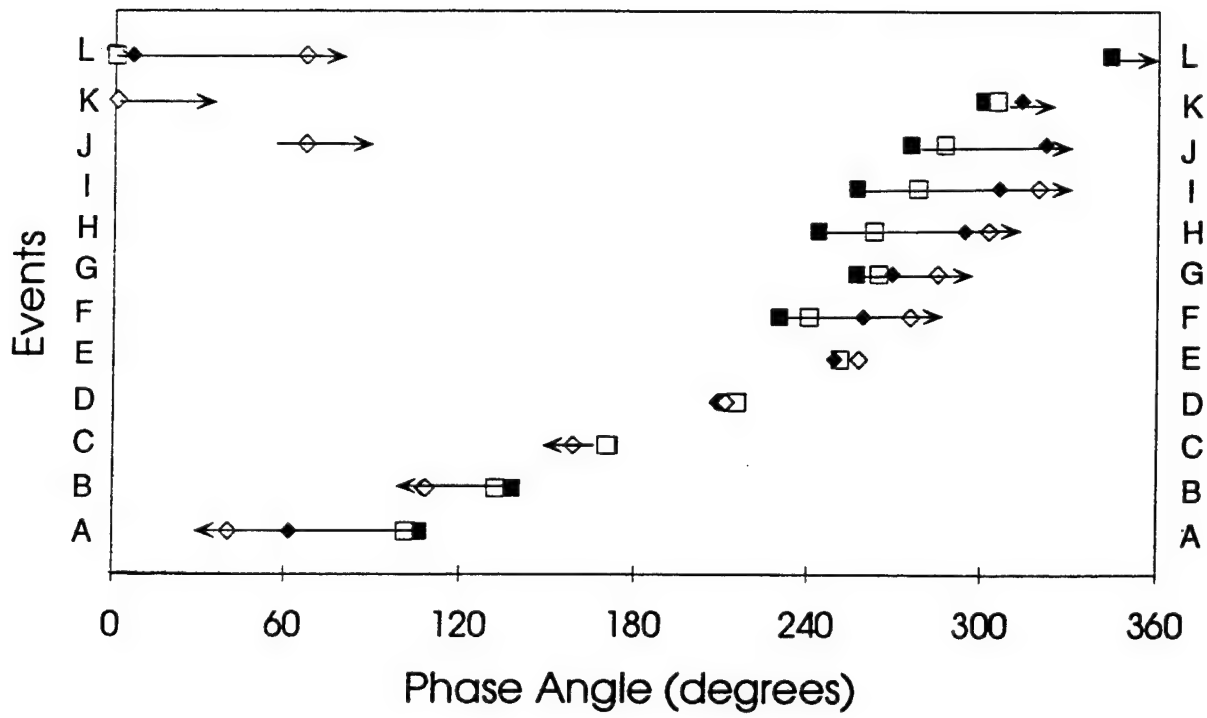


Figure 5.7: Phase angles of selected events in cavitation cycle, for reduced frequency $k = 0.74$ and four cavitation numbers. (\blacksquare $\sigma = 1.53$, \square $\sigma = 1.34$, \blacklozenge $\sigma = 1.15$, \diamond $\sigma = 0.88$)

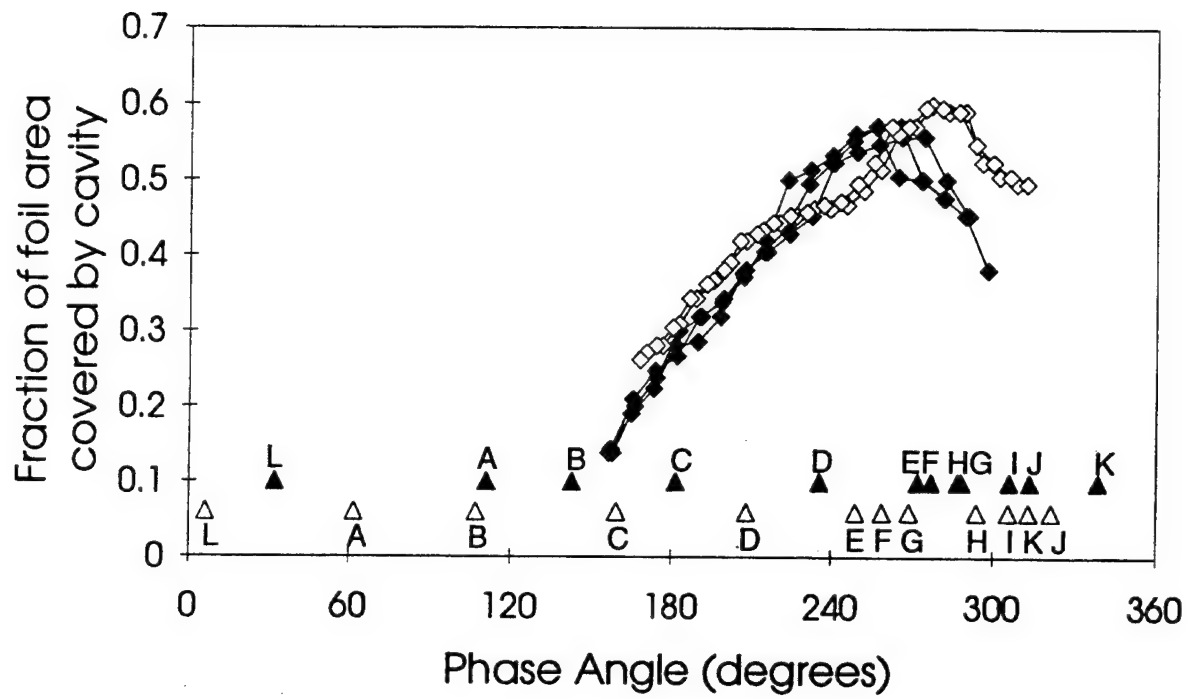


Figure 5.8: Cavity size plotted against phase angle, for cavitation number $\sigma = 1.15$ and two reduced frequencies. ($\diamond \blacktriangle k = 0.56$, $\blacklozenge \triangle k = 0.74$)

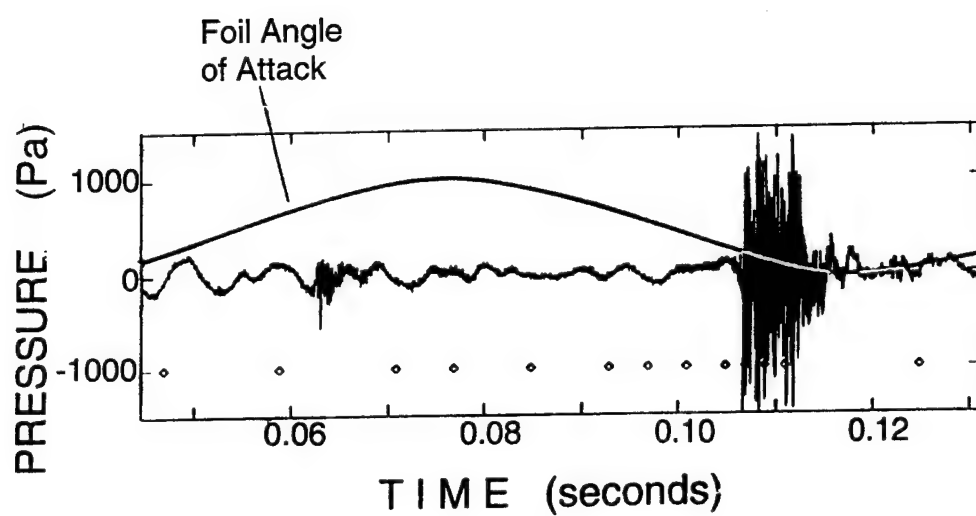


Figure 5.9: Raw acoustic signal from hydrophone, for one cycle with cavitation number $\sigma = 1.15$ and reduced frequency $k = 0.74$.

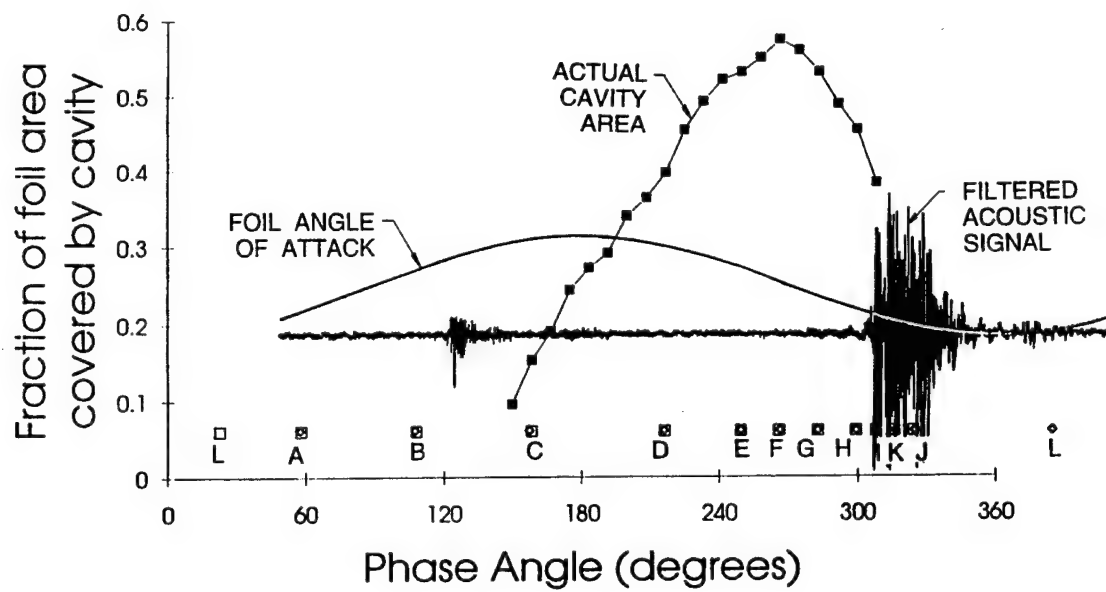


Figure 5.10: Plot of filtered acoustic signal, with cavity size and foil angle curves.

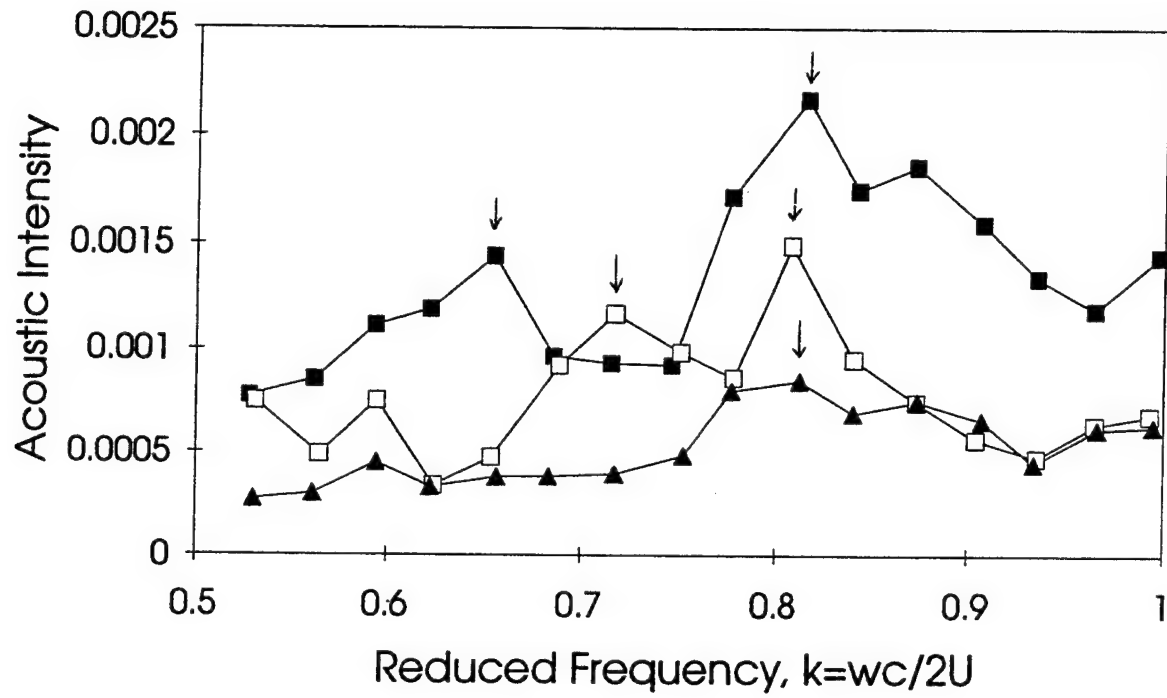


Figure 5.11: Changes in acoustic intensity, p_A^* , with reduced frequency for three cavitation numbers. ($\blacktriangle \sigma = 1.45$, $\square \sigma = 1.16$, $\blacksquare \sigma = 0.85$)

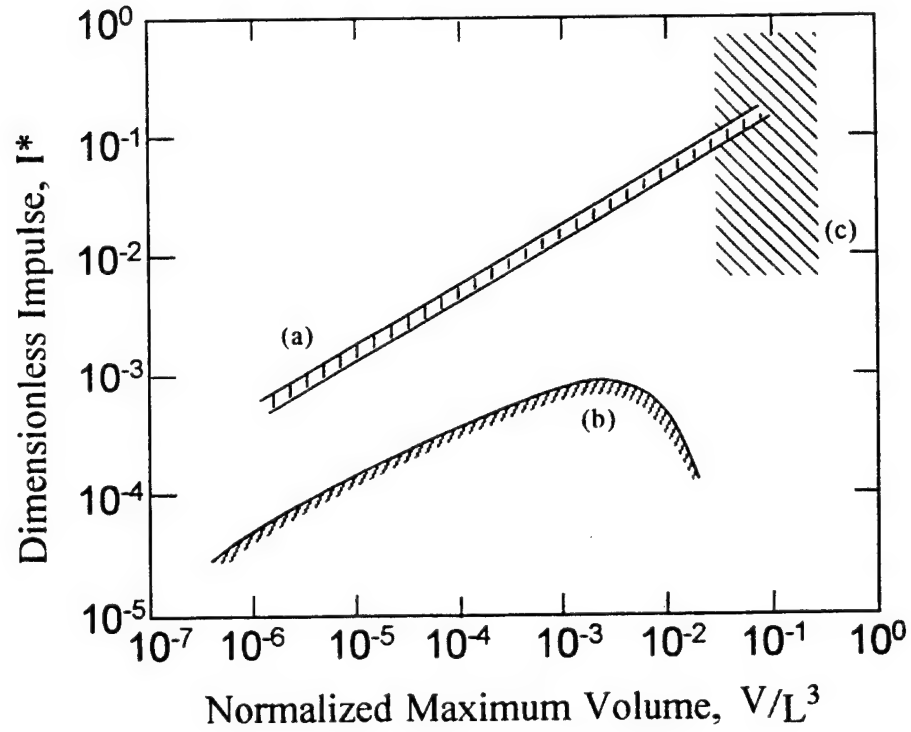


Figure 5.12: Acoustic impulse magnitude ranges as a function of the maximum bubble or cloud volume, from Reisman, *et al.* (1994). (a) Rayleigh-Plesset spherical bubble model for the same conditions as (b) and (c); (b) single travelling bubble cavitation from Kuhn de Chizelle, *et al.* (1994); (c) cloud cavitation results from Reisman, *et al.* (1994).

Chapter 6 Conclusions

Several aspects of unsteady lifting surface flows have been investigated using a variety of techniques. These flows are inherently very complicated, even in the simplified models used in these experiments, but a number of significant results were obtained nonetheless. Studies of cavitation inception on a yawed propeller illustrated the great sensitivity of the flow to non-uniformity of the inflow. Measurements of the tip vortex flow on an oscillating hydrofoil showed a dependence of the vortex strength on reduced frequency. Observations and acoustic analysis of surface cavitation on the hydrofoil demonstrated that the greatest noise from the cavitation cycle comes well after the sheet cavity has collapsed, apparently related to the collapse of cloud cavitation.

More detailed conclusions from each study are listed below:

6.1 Yawed Propeller Experiments

Stroboscopic photography was used to examine the effects of an angled inflow on propeller cavitation.

- Simple two-dimensional linear theory suggests that the effect of a non-zero yaw angle in an otherwise uniform inflow should be a sinusoidal variation in the blade loading. This effect should be the same for $\beta > 0$ or $\beta < 0$ except for a 180° phase shift.
- Photographs of fully cavitating tip vortices on the propeller illustrate clear variations with yaw angle, which are not the same as those suggested by the two-dimensional linear theory. For $\beta \neq 0$, kinks in the helical vortex cavities indicate the interaction of the vortices with the collar vortex formed

at the base of the gearcase, and at higher (positive) angles of yaw the kinks become tangled and appear to hasten vortex breakdown at those locations.

- Observations of cavitation inception for all yaw angles show the expected trend of decreasing σ_i with increasing advance ratio J . Varying the yaw angle seems to have very little effect on cavitation inception number, however.
- Comparison of experimental results with the empirical relation developed by Strasberg (1977) shows very good agreement in slope with only a small shift upwards in σ_i . This may simply be due to a higher total air content in the water used in the Strasberg experiments from which the relation was derived.

6.2 Unsteady Hydrofoil Tip Vortex

Particle Image Velocimetry (PIV) was used to examine the tip vortex flow on the oscillating hydrofoil, at one location just downstream of the trailing edge.

- Observations of the resulting images showed some interesting features, even before quantitative measurements were made.
 - As observed by Stinebring, *et al.* (1989) on a stationary foil, the flow in the tip vortex region is mostly circumferential but inboard of the vortex core on the suction side the flow clearly turns toward the midspan of the foil.
 - A secondary flow was visible at very low angles of attack, possibly a secondary vortex shed by the trailing edge, though it is unclear exactly where it is formed.
 - The vortex core diameter increases and decreases with the foil angle of attack, but the overall size appears to increase slightly with reduced frequency.

- The vortex location, measured as the distance from the foil trailing edge, increases and decreases with the foil angle of attack as well, but it is significantly farther from the foil when the angle is increasing relative to when it is decreasing. With increased reduced frequency, the distance is increased over the first half of the oscillation cycle (increasing α), but the maximum distance does not appear to change.
- The circulation was calculated using contour integration, using a special technique designed for the irregular data obtained from the PIV images. The circulation profile obtained by using successively larger contours accurately reflects the solid body rotation in the vortex core as well as the viscous diffusion region outside it.
- Despite the apparent ellipticity of the vortex in some of the images, reasonable results were also obtained by fitting the velocity magnitudes outside the core to the formula for a (circular) Rankine vortex: $V(r) = \Gamma/2\pi r$
- The circulation data calculated in this manner were compared to both steady and unsteady two-dimensional airfoil theories, and also to results obtained by Hart (1993) on the same oscillating finite-span foil using LDV techniques. There was good agreement in phase as well as the anticipated reduction in circulation due to three-dimensional effects.

6.3 Surface Cavitation Studies

Observations were made of the process of cavitation on the surface of the oscillating hydrofoil, including certain variations with cavitation number and reduced frequency.

- Changes in the cavitation process with decreasing cavitation number seem to be guided by the greater tendency toward cavitation; changes with reduced

frequency, however, appear to be driven more by the phase lag introduced by the coupling of the fluid with the oscillation of the foil.

- A high-frequency, high-amplitude burst was seen to occur in the cavitation acoustic signal, apparently after the collapse of the main cavity. From high-speed movies, it seems that this burst coincides with the existence of cloud cavitation during the collapse process. This concurs with several other studies on both hydrofoils and propellers, suggesting that cloud cavitation is a greater source of cavitation noise than either tip vortex or sheet cavitation.
- Numerical work by Wang and Brennen (1994) suggests that an inwardly-propagating shock wave within the cloud would explain some of the features of the acoustic signal; the current work supports their result, but does not confirm it. Their study also notes that the size of the cloud may not change significantly during the passage of the shock, which is also supported in the observations discussed in this thesis.
- Both Stern (1986) and Hart (1993) observe that the cavitation response of greatest amplitude (i.e. largest cavities) occurs when the forcing frequency of the foil matches the natural shedding frequency of the attached cavities. In the present study, however, there seems to be more than one noise peak with increasing k for the same σ . The source of the second peak is not currently known.

Bibliography

- Acosta, A. J., Katz, J., , and O'Hern, T. J. (Feb. 1983). Microbubbles and cavitation. Div. E&AS Report E261.2, California Institute of Technology.
- Adrian, R. J. (1991). Particle-imaging techniques for experimental fluid mechanics. *Ann. Rev. Fluid Mech.*, Vol. 23, pp. 261–304.
- Arndt, R. E. A. and Dugue, C. (1992). Recent advances in tip vortex cavitation research. In *Proc. Intl. Symp. on Propulsors and Cavitation*, pp. 142–149.
- Arndt, R. E. A., Higuchi, H., and Ikohagi, T. (1986). Tip vortex cavitation. In *Proc. Intl. Symp. on Propeller and Cavitation*, pp. 376–382, Wuxi, China.
- Arndt, R. E. A. and Maines, B. H. (1994). Vortex cavitation: A progress report. In *Proc. ASME Symp. on Cavitation and Gas-Liquid Flow in Fluid Machinery and Devices*, Vol. 190, pp. 99–117.
- Avellan, F., Dupont, P., and Ryhming, I. (1988). Generation mechanism and dynamics of cavitation vortices downstream of a fixed leading edge cavity. In *17th ONR Symp. on Naval Hydrodynamics*, pp. 317–329.
- Bark, G. (1985). Developments of distortions in sheet cavitation on hydrofoils. In *Proc. ASME Intl. Symp. on Jets and Cavities*, pp. 215–225.
- Bark, G. and van Berlekom, W. B. (1978). Experimental investigations of cavitation noise. In *Proc. 12th ONR Symp. on Naval Hydrodynamics*, pp. 470–493.
- Betz, A. (1919). Schraubenpropeller mit geringstem energieverlust. *K. Ges. Wiss. Göttingen Nachr. Math.-Phys. Klasse*, pp. 193–217.
- Betz, A. (1933). Behavior of vortex systems. Technical Memorandum 713, National Advisory Committee for Aeronautics.

- Brockett, T. E. (1981). Lifting surface hydrodynamics for design of rotating blades. In *Proc. SNAME Propellers '81*, pp. 357-378.
- Donaldson, C., Snedeker, R. S., and Sullivan, R. D. (1974). Calculation of aircraft wake velocity profiles and comparison with experimental measurements. *J. Aircraft*, Vol. 11, No. 9, pp. 547-555.
- E., W. C. and Gharib, M. (1991). Digital particle image velocimetry. *Experiments in Fluids*, Vol. 10, pp. 181-193.
- El-Ramly, Z. and Rainbird, W. J. (1977). Flow survey of the vortex wake behind wings. *J. Aircraft*, Vol. 14, No. 11, pp. 1102-1108.
- English, J. W. (1992). Observations and speculations on propeller cavitation induced vibration excitation. In *Proc. IMechE Conf. on Cavitation*, pp. 231-238.
- Franc, J. P. and Michel, J. M. (1988). Unsteady attached cavitation on an oscillating hydrofoil. *J. Fluid Mech.*, Vol. 193, pp. 171-189.
- Francis, T. B. and Katz, J. (1988). Observations on the development of a tip vortex on a rectangular hydrofoil. *J. Fluids Eng.*, Vol. 110, pp. 208-215.
- Freymuth, P. (1988a). Propulsive vortical signature of plunging and pitching airfoils. *AIAA J.*, Vol. 26, No. 7, pp. 881-883.
- Freymuth, P. (1988b). Three-dimensional vortex systems of finite wings. *J. Aircraft*, Vol. 25, No. 10, pp. 971-972.
- Freymuth, P. (1989). Visualizing the connectivity of vortex systems for pitching wings. *J. Fluids Eng.*, Vol. 111, pp. 217-220.
- Freymuth, P., Bank, W., and Palmer, M. (1984). Vortices around airfoils. *American Scientist*, Vol. 72, pp. 242-248.

- Freymuth, P., Finaish, F., and Bank, W. (1985). Three-dimensional vortex patterns in a starting flow. *J. Fluid Mech.*, Vol. 161, pp. 239–248.
- Freymuth, P., Finaish, F., and Bank, W. (1986a). Visualization of wing tip vortices in accelerating and steady flow. *J. Aircraft*, Vol. 23, No. 9, pp. 730–733.
- Freymuth, P., Finaish, F., and Bank, W. (1986b). The wing tip vortex system in a starting flow. *Zeitschrift für Flugwissenschaften und Weltraumforschung*, Vol. 10, pp. 116–118.
- Freymuth, P., Finaish, F., and Bank, W. (1987). Further visualization of combined wing tip and starting vortex systems. *AIAA J.*, Vol. 25, No. 9, pp. 1153–1159.
- Fruman, D. H. (1994). Recent progress in the understanding and prediction of tip vortex cavitation. In *The Second Intl. Symp. on Cavitation*, pp. 19–29.
- Gad-el Hak, M. and Ho, C.-M. (1986). Unsteady vortical flow around three-dimensional lifting surfaces. *AIAA J.*, Vol. 24, No. 5, pp. 713–721.
- Garrick, I. E. (1936). Propulsion of a flapping and oscillating airfoil. Report 567, National Advisory Committee for Aeronautics.
- Gates, E. M. (1977). *The Influence of Freestream Turbulence, Freestream Nuclei Populations, and a Drag-Reducing Polymer on Cavitation Inception on Two Axisymmetric Bodies*. Ph.D. thesis, Cal. Inst. of Tech.
- Goldstein, S. (1929). On the vortex theory of screw propellers. *Proc. R. Soc. London, Ser. A*, Vol. 123, pp. 440–465.
- Greeley, D. S. and Kerwin, J. E. (1982). Numerical methods for propeller design and analysis in steady flow. *Trans. SNAME*, Vol. 90, pp. 415–453.
- Green, S. I. (1988). *Tip Vortices—Single Phase and Cavitating Flow Phenomena*. Ph.D. thesis, Cal. Inst. of Tech.

- Green, S. I. and Acosta, A. J. (1991). Unsteady flow in trailing vortices. *J. Fluid Mech.*, Vol. 227, pp. 107-134.
- Hart, D. P. (1993). *Cavitation and Wake Structure of Unsteady Tip Vortex Flows*. Ph.D. thesis, Cal. Inst. of Tech.
- Hart, D. P., Brennen, C. E., and Acosta, A. J. (1990). Observations of cavitation on a three-dimensional oscillating hydrofoil. In *ASME Cavitation and Multiphase Flow Forum*, Vol. 98, pp. 49-52.
- Hsu, C. C. (1991). Studies of scaling of tip vortex cavitation inception on marine lifting surfaces. *J. Fluids Eng.*, Vol. 113, pp. 504-508.
- ITTC (1993). Report of the cavitation committee. In *Proc. 20th ITTC*.
- Kato, H. (1985). On the structure of cavity: New insight into the cavity flow: A summary of the keynote speech. In *Proc. of the ASME Intl. Symp. on Jets and Cavities*, Vol. 31, pp. 13-19.
- Kato, H., Takasugi, N., and Yamaguchi, H. (1992). Numerical analysis of a cavitating hydrofoil with finite span. In *Intl. Symp. on Propulsors and Cavitation*, Hamburg, Germany.
- Katz, J. and Bueno Galdo, J. (1989). Effect of roughness on rollup of tip vortices on a rectangular hydrofoil. *J. Aircraft*, Vol. 26, No. 3, pp. 247-253.
- Kerwin, J. E. (1986). Marine propellers. *Ann. Rev. Fluid Mech.*, Vol. 18, pp. 367-403.
- Kita, Y., Koumoto, H., Hirose, K., and Yamamoto, K. (1994). Flat plate wing standing on a wall covered with a thick boundary layer (wing characteristics under the effects of side wall boundary layer and wing tip vortex). *JSME Intl. J., Series B*, Vol. 37, No. 2, pp. 355-362.

- Knapp, R. T. (1955). Recent investigations of the mechanics of cavitation and cavitation damage. *Trans. of the ASME: J. Basic Eng.*, pp. 1045–1054.
- Kubota, A., Kato, H., Yamaguchi, H., and Maeda, M. (1989). Unsteady structure measurement of cloud cavitation on a foil section using conditional sampling. *J. Fluids Eng.*, Vol. 111, pp. 204–210.
- Kuhn de Chizelle, Y., Ceccio, S. L., and Brennen, C. E. (1995). Observations, scaling and modelling of travelling bubble cavitation. *J. Fluid Mech.*, Vol. 293, pp. 99–126.
- Lawrence, H. R. and Gerber, E. H. (1952). The aerodynamic forces on low aspect ratio wings oscillating in an incompressible flow. *J. Aero. Sci.*, pp. 769–781.
- Lerbs, H. W. (1952). Moderately loaded propellers with a finite number of blades and an arbitrary distribution of circulation. In *Proc. SNAME*, Vol. 60, pp. 73–117.
- Maeda, M., Yamaguchi, H., and Kato, H. (1991). Laser holography measurement of bubble population in cavitation cloud on a foil section. In *Proc. ASME Symp. on Cavitation*, Vol. 116, pp. 67–75.
- Maines, B. H. and Arndt, R. E. A. (1993a). Bubble dynamics of cavitation inception in a wing tip vortex. In *ASME FED Forum on Cavitation and Multiphase Flow*, Vol. 153, pp. 93–97.
- Maines, B. H. and Arndt, R. E. A. (1993b). Viscous effects on tip vortex cavitation. In *ASME FED Intl. Symp. on Cavitation*.
- McCormick, B. W., J. (1962). On cavitation produced by a vortex trailing from a lifting surface. *J. Basic Eng.*, pp. 369–379.
- McCroskey, W. J. (1982). Unsteady airfoils. *Ann. Rev. Fluid Mech.*, Vol. 14, pp. 285–311.

- McKenney, E. A. (1994). Effects of yaw on propeller cavitation inception. In *Proc. ASME Cavitation and Multiphase Flow Forum*, pp. 83-87.
- McKenney, E. A. and Brennen, C. E. (1994). On the dynamics and acoustics of cloud cavitation on an oscillating hydrofoil. In *Proc. ASME Symp. on Cavitation and Gas-Liquid Flow in Fluid Machinery and Devices*, pp. 195-202.
- McKenney, E. A. and Hart, D. P. (1993). Experimental determination of bound circulation and shed vorticity induced by an oscillating hydrofoil. In *Proc. ASME Cavitation and Multiphase Flow Forum*, pp. 87-91.
- Moore, D. W. (1974). A numerical study of the roll-up of a finite vortex sheet. *J. Fluid Mech.*, Vol. 63, No. 2, pp. 225-235.
- Mørch, K. A. (1980). On the collapse of cavity cluster in flow cavitation. In *Proc. First Intl. Conf. on Cavitation and Inhomogeneities in Underwater Acoustics*, Vol. 4, pp. 95-100. Springer Series in Electrophysics.
- Mørch, K. A. (1981). Cavity cluster dynamics and cavitation erosion. In *ASME Cavitation and Polyphase Flow Forum*, pp. 1-10.
- Noordzij, L., van Oossanen, P., and Stuurman, A. M. (1977). Radiated noise of cavitating propellers. In *ASME FED Symp. on Noise and Fluids Engineering*, pp. 101-108.
- O'Hern, T. J. (1987). *Cavitation Inception Scale Effects: I. Nuclei Distributions in Natural Waters; II. Cavitation Inception in a Turbulent Shear Flow*. Ph.D. thesis, Cal. Inst. of Tech.
- Pogozelski, E. M., Shekariz, A., Katz, J., and Huang, T. T. (1993). Three-dimensional near field behavior of a tip vortex developing on an elliptic foil. Paper 93-0865, AIAA.

- Prandtl, L. (1921). Application of modern hydrodynamics to aeronautics. 7th annual report, NACA.
- Reisman, G., McKenney, E., and Brennen, C. (1994). Cloud cavitation on an oscillating hydrofoil. In *Proc. 20th ONR Symp. on Naval Hydrodynamics*, pp. 78-89.
- Sears, W. R. (1938). A contribution to the airfoil theory for non-uniform motion. In *Proc. 5th Intl. Conf. Appl. Mech.*, Vol. 80, pp. 483-487.
- Sharma, S. D., Mani, K., and Arakeri, V. H. (1990). Cavitation noise studies on marine propellers. In *J. Sound and Vibration*, Vol. 138, pp. 255-283.
- Shekarritz, A., Fu, T. C., Katz, J., and Huang, T. T. (1993). Near-field behavior of a tip vortex. *AIAA J.*, Vol. 31, No. 1, pp. 112-118.
- Shekarritz, A., Fu, T. C., Katz, J., Liu, H. L., and Huang, T. T. (1991). Quantitative visualization of junction and tip vortices using particle displacement velocimetry. Paper 91-0269, AIAA.
- Shekarritz, A. and Fu, T. C., Katz, J., Liu, H. L., and Huang, T. T. (1992). Study of junction and tip vortices using particle displacement velocimetry. *AIAA J.*, Vol. 30, No. 1, pp. 145-152.
- Shen, Y. and Peterson, F. B. (1978). Unsteady cavitation on an oscillating hydrofoil. In *Proc. 12th ONR Symp. on Naval Hydrodynamics*, pp. 362-384.
- Shen, Y. T. and Peterson, F. B. (1980). The influence of hydrofoil oscillation on boundary layer transition and cavitation noise. In *Proc. 13th ONR Symp. on Naval Hydrodynamics*, pp. 221-241.
- Soyama, H., Kato, H., and Oba, R. (1992). Cavitation observations of severely erosive vortex cavitation arising in a centrifugal pump. In *Proc. Third IMechE Intl. Conf. on Cavitation*, pp. 103-110.

- Sparenberg, J. A. (1959). Application of lifting surface theory to ship screws. *Proc. K. Ned. Akad. Wet.*, Vol. 62, No. 5, pp. 286–298.
- Spreiter, J. R. and Sacks, A. H. (1986). The rolling up of the trailing vortex sheet and its effect on the downwash behind wings. *J. Aero. Sci.*, Vol. 18, No. 1, pp. 21–32, 72.
- Stern, F. (1989). Comparison of computational and experimental unsteady cavitation on a pitching foil. *J. Fluids Eng.*, Vol. 111, pp. 290–299.
- Stinebring, D. R., Farrell, K. J., and Billet, M. L. (1989). The structure of a three-dimensional tip vortex at high reynolds numbers. In *Proc. of the 22nd ATTC*, pp. 3–12.
- Strasberg, M. (1977). Propeller cavitation noise after 35 years of study. In *ASME FED Symp. on Noise and Fluids Engineering*, pp. 89–99.
- Theodorsen, T. (1935). General theory of aerodynamic instability and the mechanism of flutter. Report 496, National Advisory Committee for Aeronautics.
- von Kármán, T. and Sears, W. R. (1938). Airfoil theory for non-uniform motion. *J. Aero. Sci.*, Vol. 5, No. 10, pp. 379–390.
- Wang, M.-H. (1985). *Hub Effects in Propeller Design and Analysis*. Ph.D. thesis, Mass. Inst. of Tech.
- Wang, Y.-C. and Brennen, C. E. (1994). Shock wave development in the collapse of a cloud of bubbles. In *ASME FED Cavitation and Multiphase Flow Forum*, Vol. 194.
- Yamaguchi, H., Tanaka, M., and Kato, H. (1991). A numerical study on mechanism of vortex generation downstream of a sheet cavity on a two-dimensional hydrofoil. In *ASME FED Cavitation and Multiphase Flow Forum*, Vol. 109, pp. 27–34.

- Ye, Y. P., Kato, H., and Maeda, M. (1989). On correlation of cavitation erosion and noise on a foil section. In *Intl. Workshop on Cavitation*, pp. 68–75, Wuxi, Jiangsu, China.
- Yongsong, G. (1986). On cavitating core radius and cavitation inception of tip vortex trailing from a hydrofoil. In *Proc. Intl. Symp. on Propeller and Cavitation*, pp. 231–234, Wuxi, China.

Appendix A Appendix: Propeller Facility

A new facility was designed and constructed in order to study the effects of yaw angle on the flow about a propeller. The propeller drive was installed in the LTWT test section as shown in Figure 2.2. This apparatus provides a variety of functions to accommodate a range of experiments. The 8.5-inch diameter propeller is a right-handed, three-bladed model. Both the propeller and its right-angle gearcase were obtained from the lower end of a Johnson 6-HP marine outboard motor, as shown in the photograph in Figure A.1. They are now driven by a 5-HP Baldor AC motor (controlled by a programmable inverter unit from Sabina Electric) located outside the test section. The motor is capable of up to 3450 RPM; this corresponds to a propeller rotation speed of approximately 1550 RPM due to the gear ratio within the gearcase. For the current study, however, the propeller rotated at 1060 RPM. The angle of the propeller with respect to the freestream was set via a taper-lock bushing. It could be adjusted easily between experiments, allowing the propeller to be yawed up to 20° from the freestream direction. A photograph of the assembly, outside the test section, is shown in Figure A.2.

A.1 Propeller Specifications

The propeller currently used in the facility is a commercial outboard unit with three plano-convex blades. Approximate measurements were made of several key parameters of the propeller design, since specifications were not available from the manufacturer. A photograph of the propeller, along with a sketch describing some of these parameters, is shown in Figure A.3. Table A.4 lists some of the

measured quantities.

A.2 Propeller Timing Unit

A shaft encoder is geared to the drive shaft so that it matches the propeller gearcase ratio and provides electronic signals (1440 pulses/rev) to indicate the angular position and motion of the propeller blades. An electronic circuit was designed and built to process the encoder pulses and provide synchronization pulses at desired intervals (once per rotation or once per blade), useful for triggering other equipment such as a laser sheet, strobe flashes, or a computer data acquisition system. The unit also calculates and displays the rate of rotation of the propeller. A diagram of this circuit is shown in Figure A.5, and a detailed operating description follows here:

The encoder (BEI model L25) has two outputs, one giving 1440 pulses per revolution and the other only one pulse per revolution. Both of these are forwarded to the front panel as "1440" and "ZERO" outputs respectively.

In addition, there is a "SYNC" output which can be configured in a variety of ways. Normally there is one pulse on the "SYNC" output per revolution of the propeller, offset from the "ZERO" pulse as indicated by four thumbwheels on the front panel. The number shown by the thumbwheels is the number of "1440" pulses that the circuit will delay between receiving the "ZERO" pulse from the encoder and sending a pulse to the "SYNC" output. This offset does not take effect, however, until the "SET ANGLE" button is pressed to indicate that the desired number is now showing on the thumbwheels. There is also a front panel switch (marked "1/3") that allows the user to choose whether the circuit will produce one "SYNC" pulse per revolution of the propeller, or three pulses equally spaced in the cycle—in case triggering is desired once per blade, for example. (If a propeller with other than three blades is used, the circuit may easily be modified to accommodate the new number of blades.)

The "SYNC" output line may optionally be gated via a button labelled "TRIGGER" on the front panel. If the switch marked "SINGLE/CONT." is set to "CONT.," the "SYNC" output is generated every revolution of the propeller as described previously. If the switch is set to "SINGLE," then the "SYNC" output will be generated only once, and only during the first revolution after the trigger button is pressed. (This is useful, for example, for strobe photography where only a single trigger to the flash is desired.) There is also an input marked "EXT. TRIG.," such that a switch closure of the contacts will produce the same effect as pressing the trigger button.

Finally, the rotational speed of the propeller is shown on an LED display on the front panel, either in CPS or RPM (switch selectable). This portion of the circuit is shown in Figure A.6.

A.3 Facility Design

The propeller apparatus was designed specifically to mount in the same test section floor plate as the oscillating foil apparatus. The propeller gearcase was cut so that the propeller shaft would coincide with the centerline of the test section. Then a disc was mounted to the open end of the gearcase, both to seal the oil cavity and to fit into the recess in the floor plate. The shift rod was shortened so that only a small section was accessible for possible future reverse operation of the propeller transmission. A new collar shaft was machined to replace the one that would normally attach to the disc to oscillate the foil; it was designed to house the propeller drive shaft and provide the capability for changing the yaw angle of the propeller from outside the test section.

Figure A.7 and following contain the technical drawings from which the assembly was machined and constructed.

A.4 Propeller Disassembly Instructions

To remove the propeller assembly from the LTWT test section, follow these instructions. (To install in the test section, reverse the order of the steps.)

1. Remove from test section:

- (a) Remove propeller: Straighten cotter pin and remove. Remove black plastic cone and shear pin. Slide propeller off shaft. Retain and store all parts.
- (b) Slide encoder belt off of gears, leave on top of motor. Remove encoder bracket (with encoder and large gear attached) and store with bolts, making sure gear will not be damaged. (Remove gear if necessary.)
- (c) Remove lift hole plug. (Place on shelf over workbench, with similar plugs.) Install lift ring, adjust with overhead crane to tension.
- (d) Unbolt aluminum bracket and remove.
- (e) Roll cart underneath test section, with one end open. (Make sure ends are attached at lower set of holes, so that propeller will fit under test section.) Place under bottom plate so that motor will line up with hole in cart bottom. Reattach open end of cart.
- (f) Lower plate onto cart. Remove lift ring and move crane out of the way. Roll cart to desired disassembly location.

2. Dismount motor:

- (a) Loosen couplings on motor shaft.
- (b) Support motor by lift or crane, remove bolts holding bracket to plate. (Leave motor attached to bracket.) Remove couplings, retain and store. Store motor/bracket unit (keep cord attached).

3. Remove propeller subassembly:

- (a) Remove small encoder gear and belt. Store.
- (b) Remove six screws bolting propeller base to collar. Lift propeller, making sure drive shaft does not come out of gearcase (otherwise oil will leak out).
- (c) If gearcase disassembly is desired:
 - i. First remove drive shaft, holding propeller unit upside down.
 - ii. Turn unit upright over receptacle and allow oil to drain (remove or loosen oil fill screw to speed draining process).
 - iii. When oil is drained, remove six bolts from bottom of propeller base, and back out screw in edge of base holding shift rod in place.
 - iv. Gently pry base off of gearcase (now adhered only with Form-A-Gasket), watching carefully that shift rod does not get bent.
 - v. Remove shift rod. Retain and store all parts, including O-rings.

4. Remove collar:

- (a) Turn plate upside down if desired. (Make sure no extra water or oil from propeller unit will drip during process.)
- (b) Loosen taper-lock bushing. Remove six bolts holding bushing block (access sixth bolt behind smaller vernier plate). Remove taper-lock bushing and block.
- (c) Unbolt and remove Fafnir ("bulkhead") bearing. Collar should now remove easily (in fact if plate is upside down it may have already started to fall out). Save bearing and bolts for re-installation in foil assembly.
- (d) Retain and store all parts.



Figure A.1: Propeller and Gearcase.

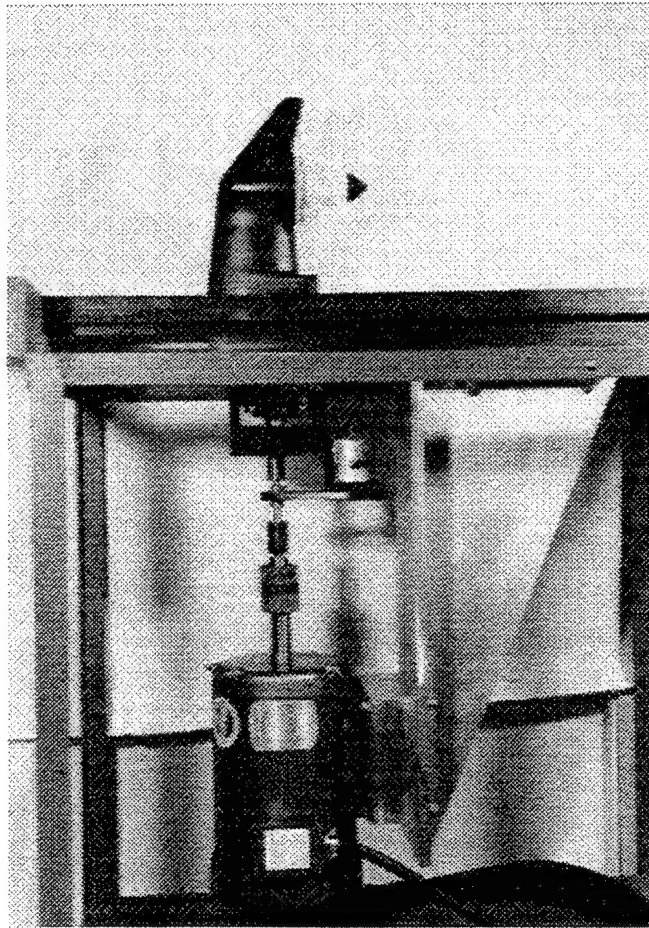


Figure A.2: Yawed propeller assembly, outside test section.

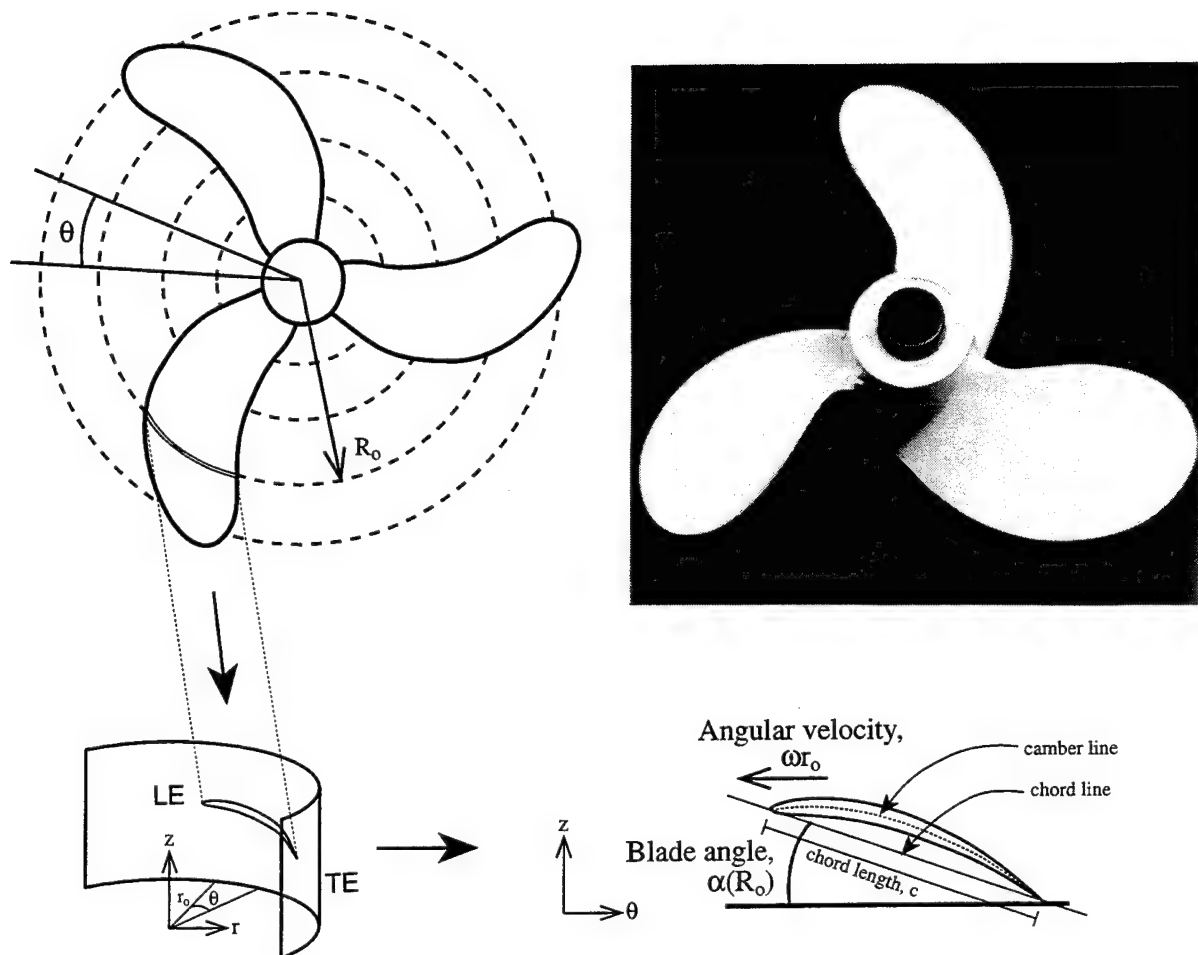


Figure A.3: Blade section notation.

R/Ro	Arclength	Heights (inches)		α
	(inches)	LE	TE	(degrees)
0.27	1.71	1.827	3.54	45.05
0.37	1.91	2.08	3.608	38.66
0.46	2.15	2.232	2.71	34.5
0.55	2.34	2.39	3.73	29.8
0.64	2.53	2.47	3.7	25.9
0.74	2.52	2.592	3.655	22.9
0.84	2.42	2.654	3.56	20.5
0.92	2.23	2.75	3.444	17.3

Figure A.4: Propeller blade measurements.

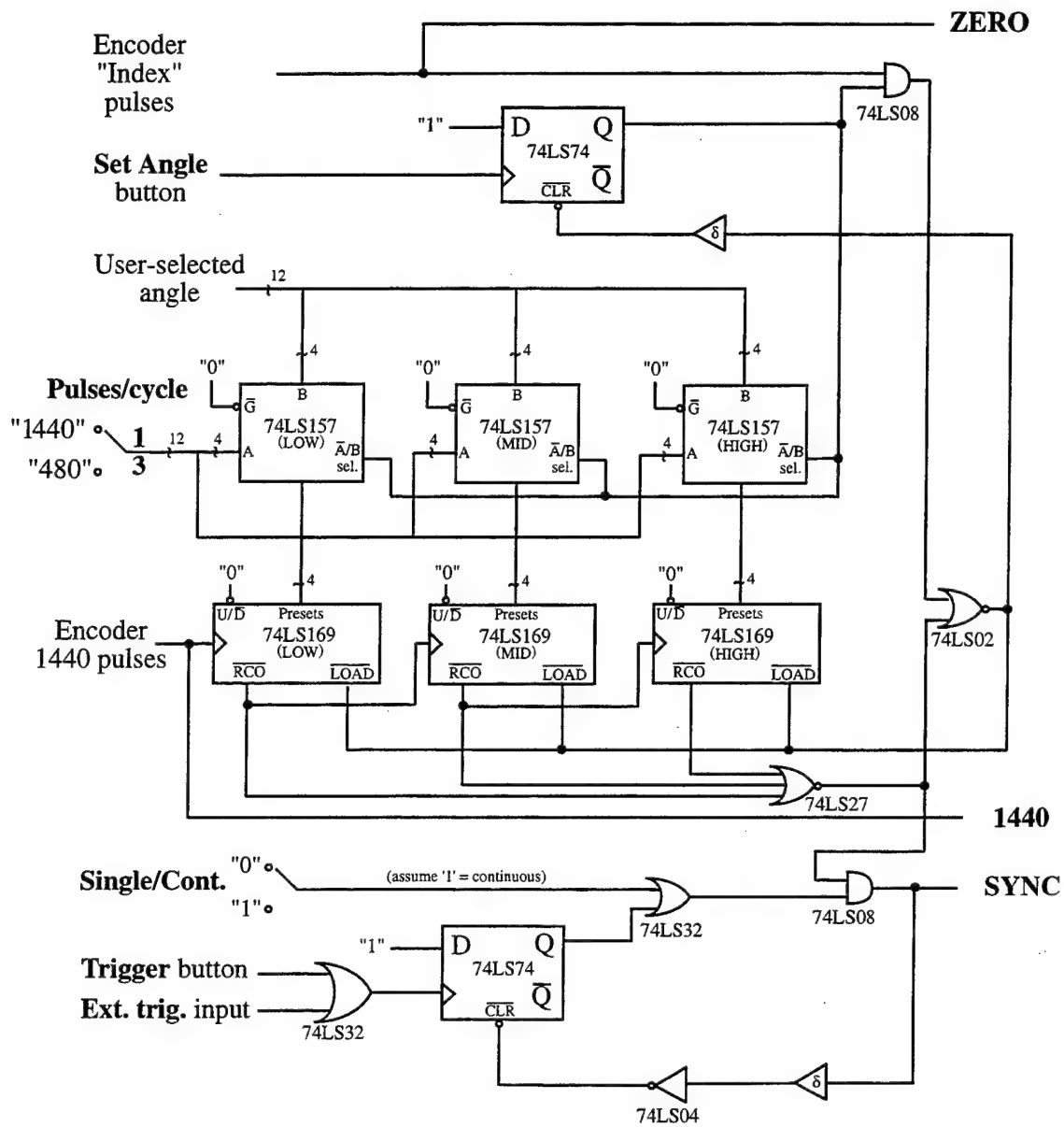


Figure A.5: Encoder circuit schematic.

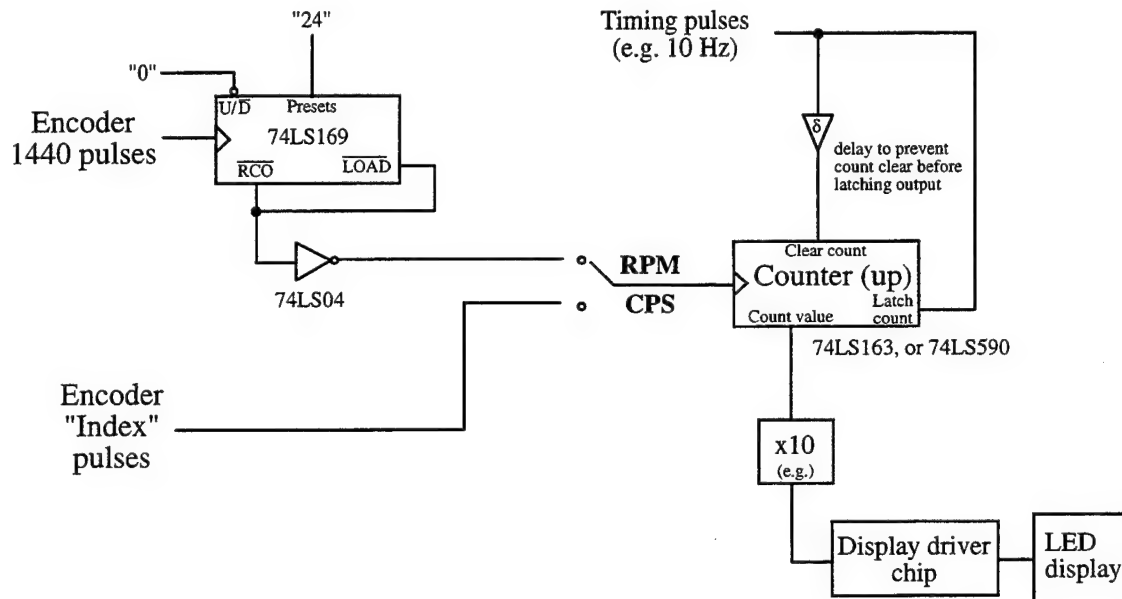


Figure A.6: Frequency display circuit schematic.

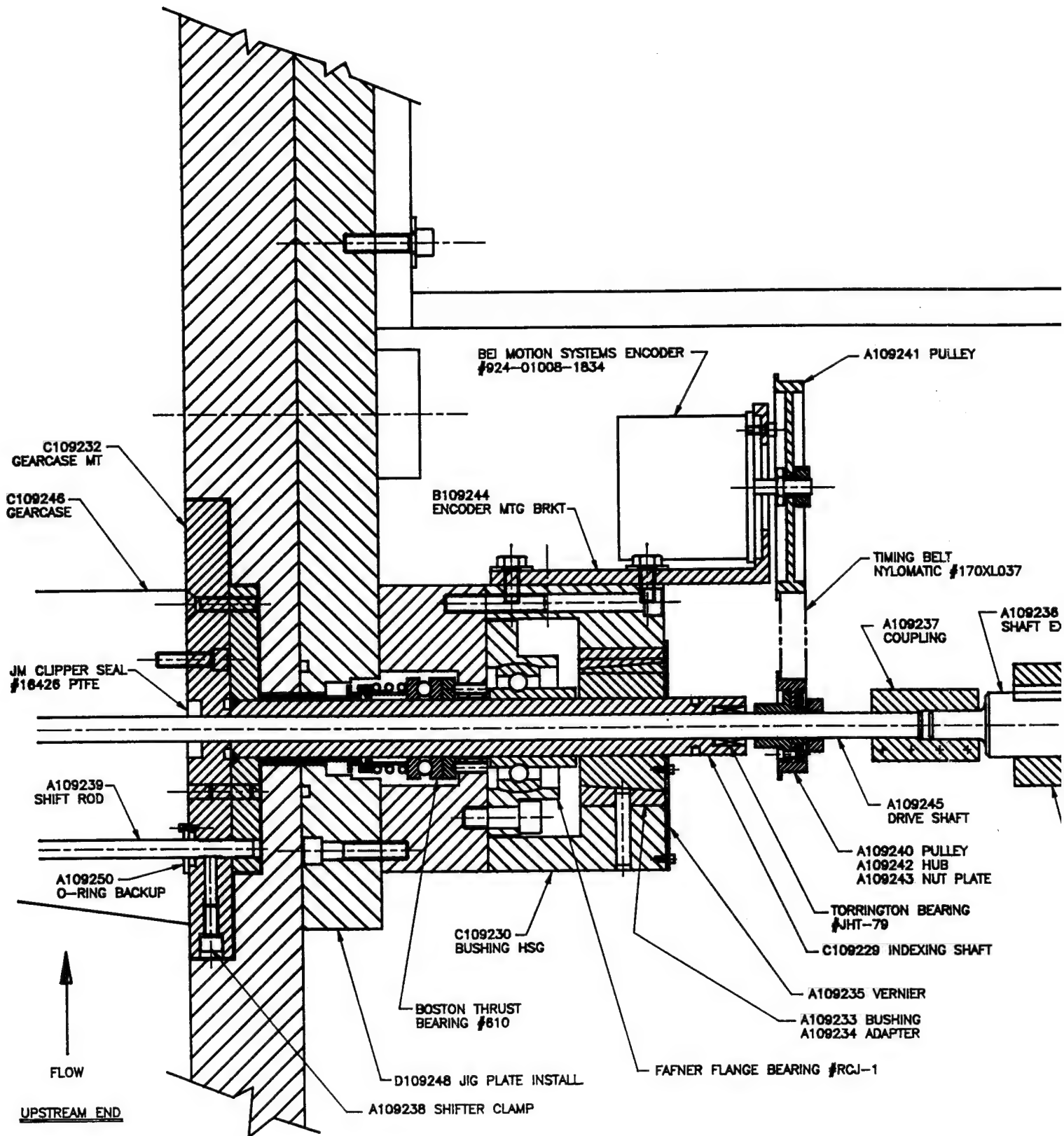
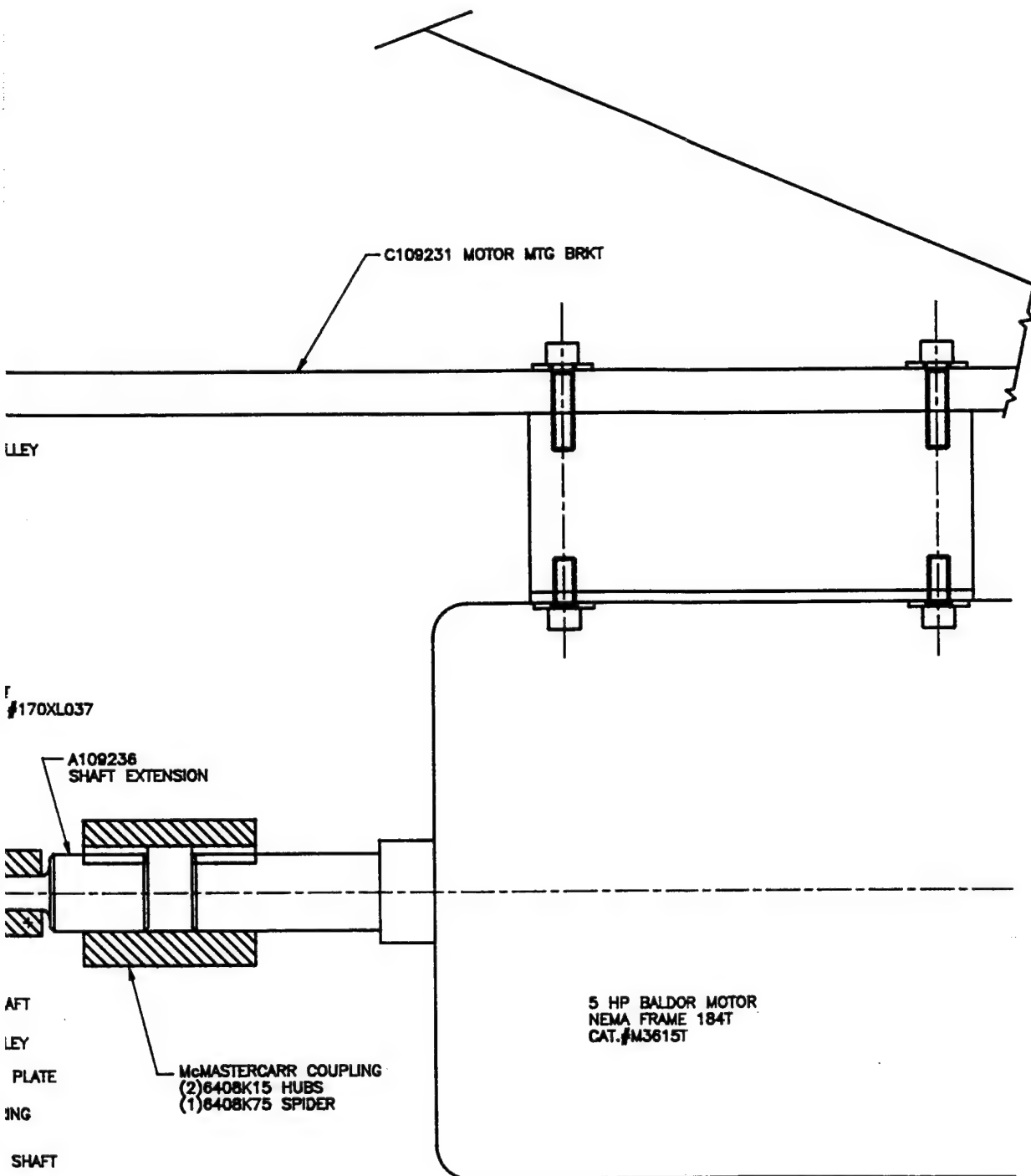
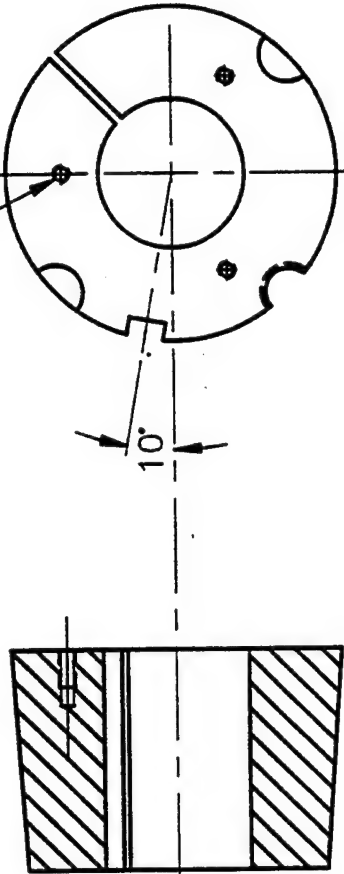


Figure A.7: Propeller apparatus drawings.

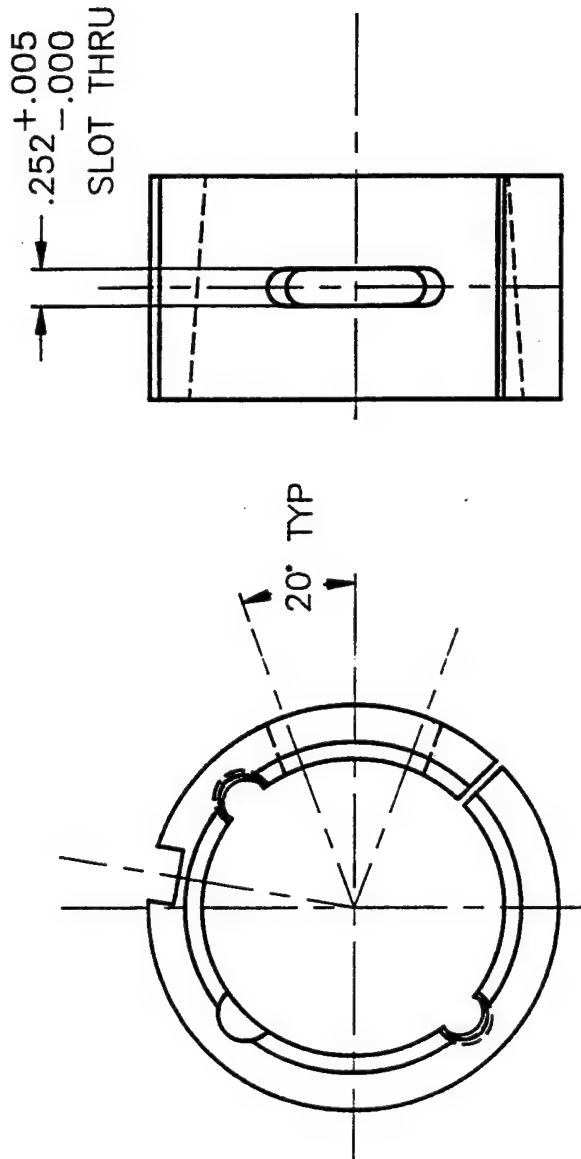


REV	DESCRIPTION	DATE	BY	CHKD	APP'D
1	ASSEMBLY	10/1/72	W. J. H.		
2	PROPELLER	10/1/72	W. J. H.		
3	TEST APPARATUS	10/1/72	W. J. H.		
CALIFORNIA INSTITUTE OF TECHNOLOGY CENTRAL ENGINEERING SERVICES					
TITLE ASSEMBLY, PROPELLER CAVITATION TEST APPARATUS			DWG. NO. D109249		CHG.

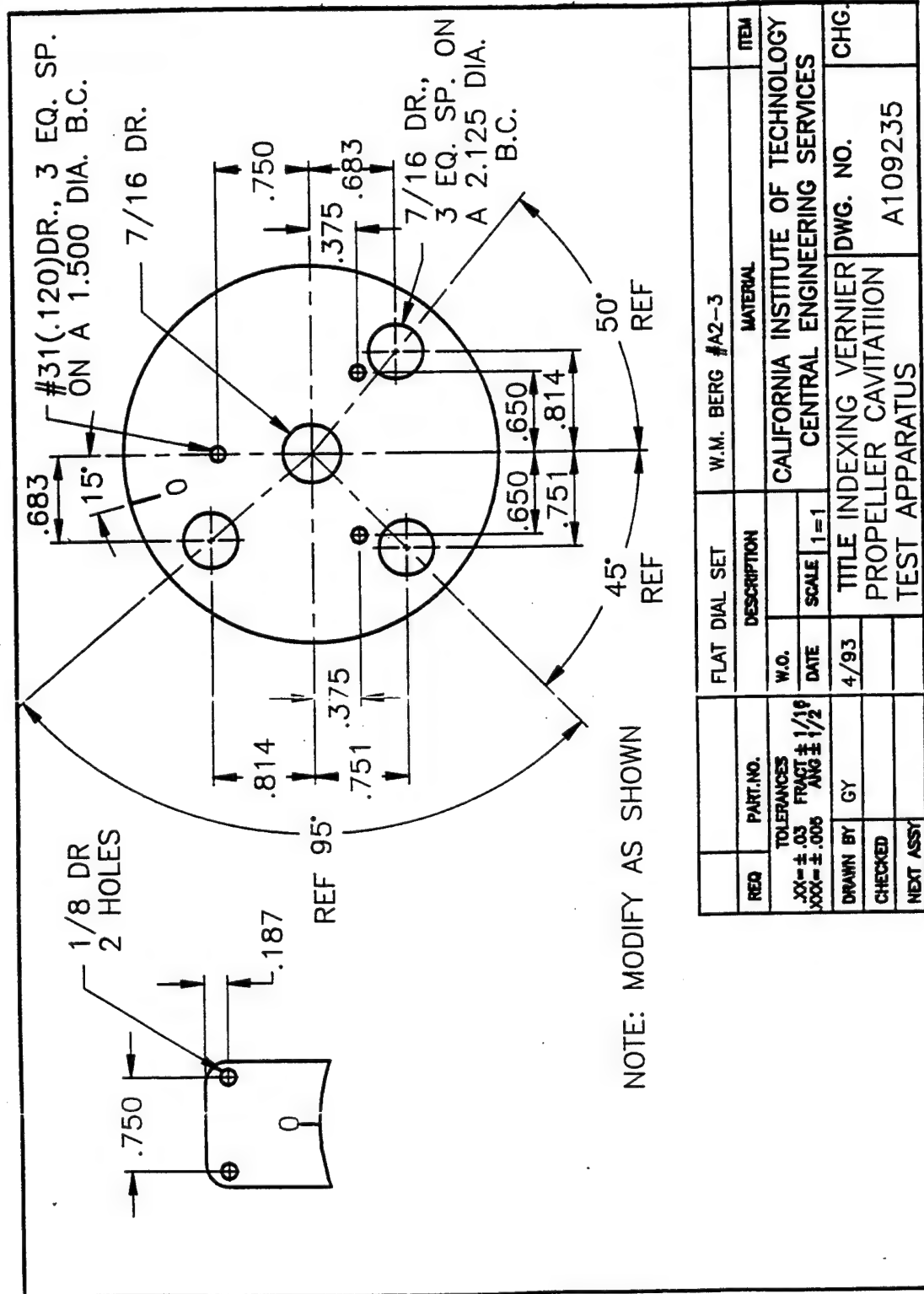
#4-40 X 1/4 DP
(3) EQ. SP. ON
A 1.500 DIA. B.C.



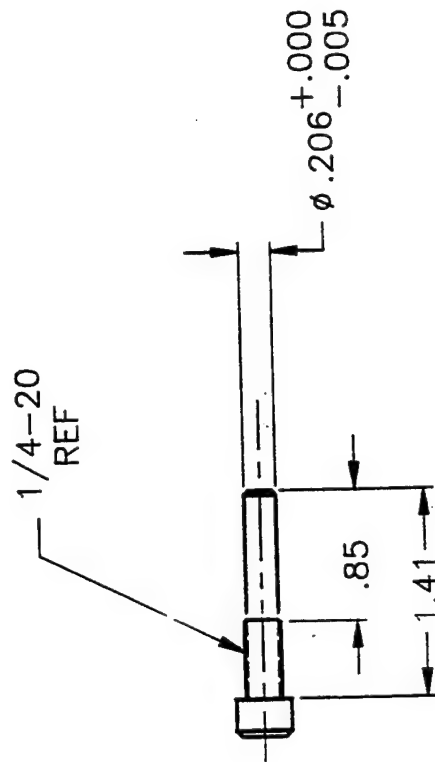
1	TAPER-LOCK BUSH. DODGE #1615 X 1		ITEM	
REQ	PART NO.	DESCRIPTION	MATERIAL	
TOLERANCES		W.O.	CALIFORNIA INSTITUTE OF TECHNOLOGY CENTRAL ENGINEERING SERVICES	
.XX = ±.03 FRACT ± 1/16		DATE		
XXX = ±.005 ANG ± 1/2		SCALE	1=1	
DRAWN BY	GY	4/93	TITLE BUSHING	
CHECKED			DWG. NO. A109233	
NEXT ASSY			PROPELLER CAVITATION TEST APPARATUS	
			CHG.	



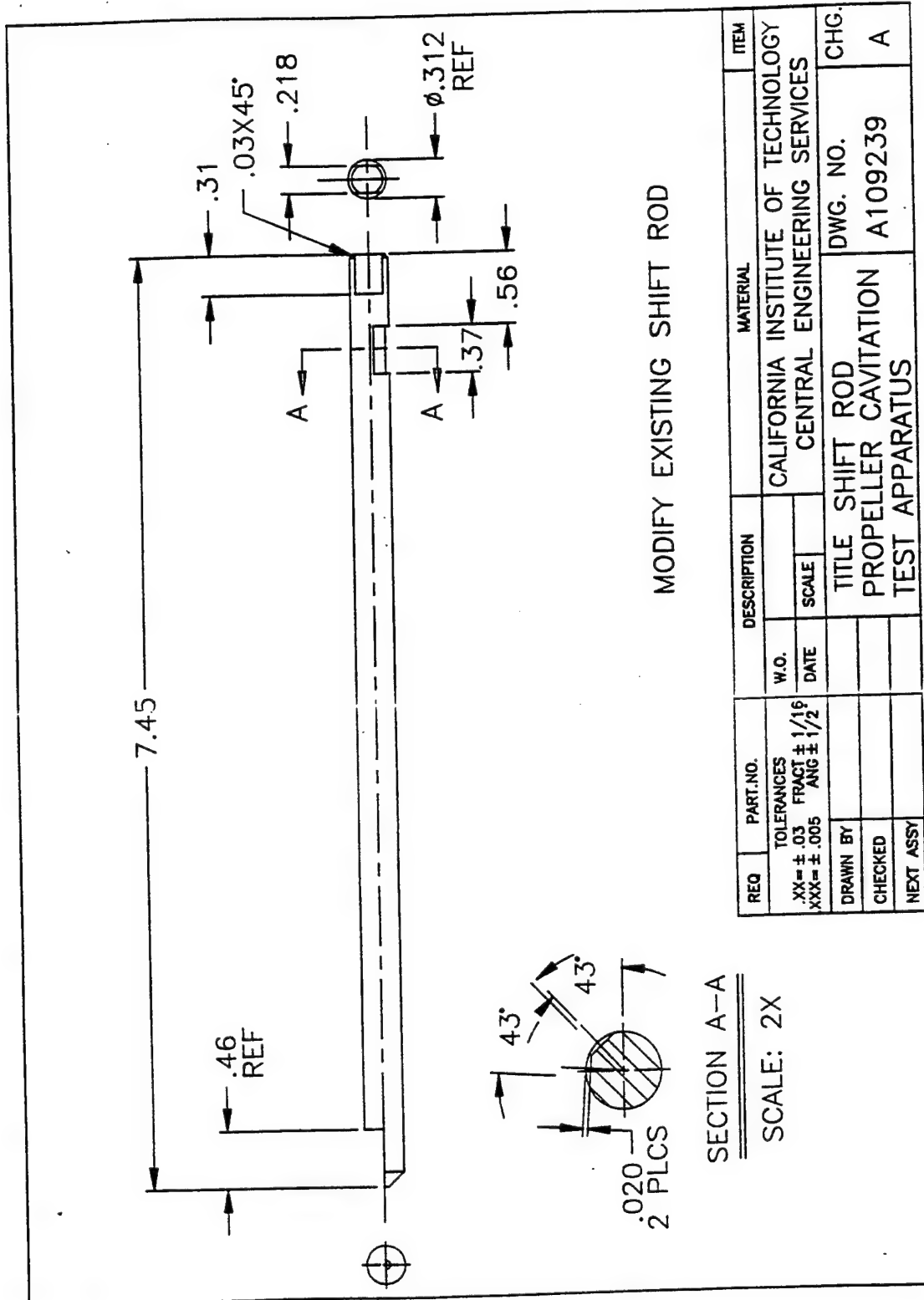
1	TAPER-LOCK ADPTR		DODGE#1615B		ITEM
REQ	PART NO.	DESCRIPTION		MATERIAL	
TOLERANCES XX = $\pm .03$ XXX = $\pm .005$		W.O.	SCALE	CALIFORNIA INSTITUTE OF TECHNOLOGY CENTRAL ENGINEERING SERVICES	
FRACT $\pm 1/16$ ANG $\pm 1/2$		DATE	1=1	DWG. NO. A109234	
DRAWN BY	GY	4/93	TITLE ADAPTER, PROPELLER CAVITATION TEST APPARATUS		CHG. A
CHECKED					
NEXT ASSY					



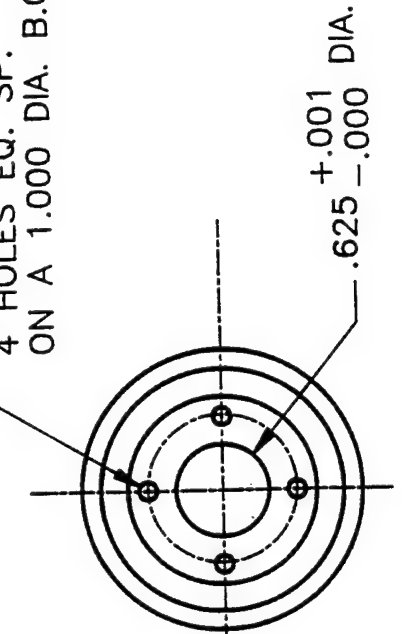
REQ	PART NO.	FLAT DIAL SET	W.M. BERG #A2-3	ITEM
TOLERANCES		CALIFORNIA INSTITUTE OF TECHNOLOGY		
XX = ± .03		CENTRAL ENGINEERING SERVICES		
XXX = ± .005		TITLE INDEXING VERNIER DWG. NO.		
ANG ± 1/2		PROPELLER CAVITATION		
DRAWN BY		TEST APPARATUS		
CHECKED		A109235		
NEXT ASSY		CHG.		



1	1/4-20 X 1-1/2 SHCS S.S.		ITEM	
REQ	PART. NO.	DESCRIPTION	MATERIAL	
TOLERANCES .XX = $\pm .03$ XXX = $\pm .005$		W.O.	CALIFORNIA INSTITUTE OF TECHNOLOGY	
FRACT $\pm 1/16$		DATE	CENTRAL ENGINEERING SERVICES	
ANG $\pm 1/2$		SCALE 1X	CHG.	
DRAWN BY	GY	5/93	TITLE SHIFTER CLAMP	
CHECKED			PROPELLER CAVITATION	
NEXT ASSY			TEST APPARATUS	
			DWG. NO. A109238	



#31(.120)DR
4 HOLES EQ. SP.
ON A 1.000 DIA. B.C.



.086
REF

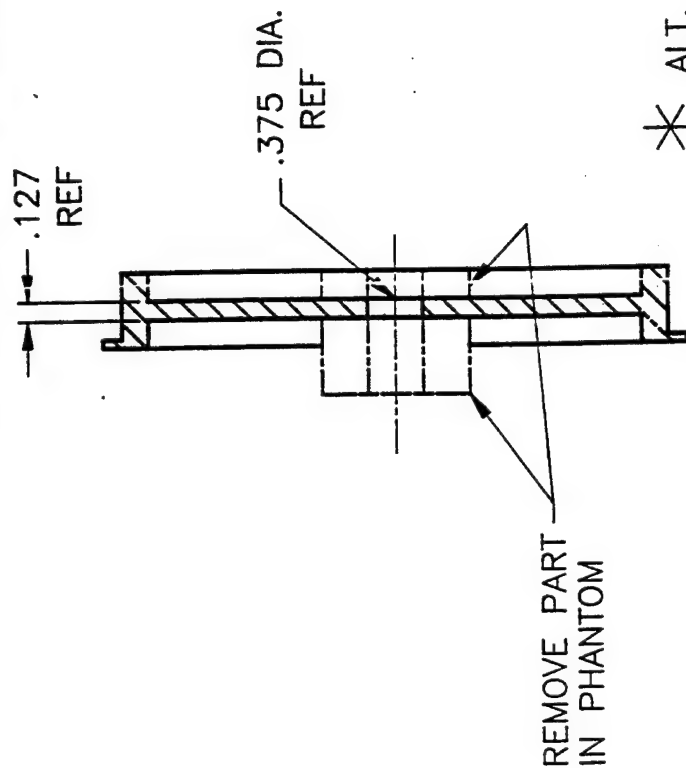


REMOVE PART
IN PHANTOM

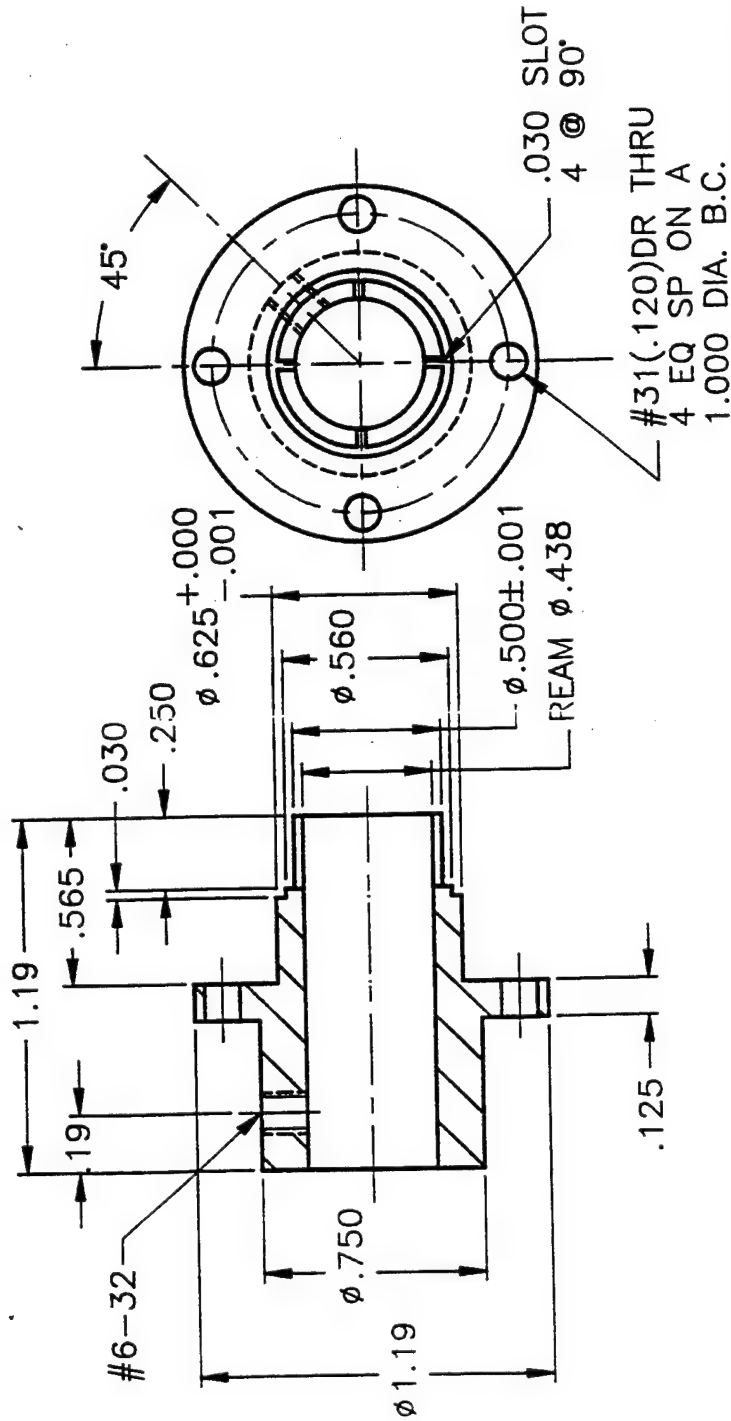
* ALT. SUPPLIER: SEITZ #0008701

1		PULLEY		NYLOMATIC #26XL037-SF		ITEM
REV	PART NO.	DESCRIPTION		MATERIAL		ITEM
TOLERANCES .XX = ±.03 FRACT ± 1/16 .XXX = ±.008 ANG ± 1/2		W.O.	SCALE	CALIFORNIA INSTITUTE OF TECHNOLOGY CENTRAL ENGINEERING SERVICES		CHG.
DRAWN BY	GY	DATE	1 = 1	TITLE PULLEY(SMALL) PROPELLER CAVITATION TEST APPARATUS		DWG. NO. A109240
CHECKED		5/93				
NEXT ASSY						

*

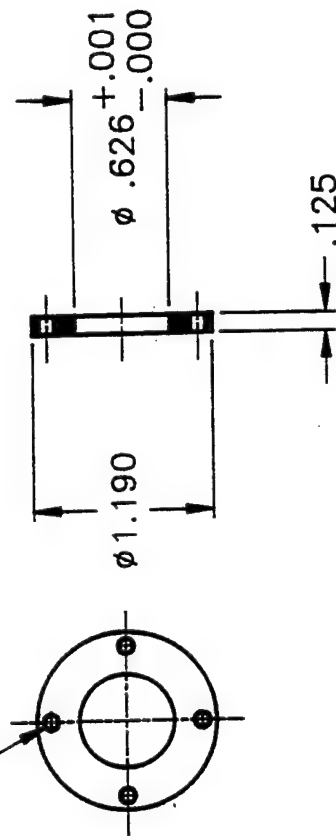


1	PART. NO.	PULLEY	NYLOMATIC #58X037-SF	ITEM
RED	TOLERANCES .001- ± .03 .002- ± .005	DESCRIPTION	MATERIAL	
	FRAC 1/16 ANG 1/2	W.O. DATE	CALIFORNIA INSTITUTE OF TECHNOLOGY CENTRAL ENGINEERING SERVICES	
DRAWN BY	GY	5/93	TITLE PULLEY (LARGE) PROPELLER CAVITATION TEST APPARATUS	DWG. NO. A109241
CHECKED				CHG.
NEXT ASSY				



1	REQ	PART. NO.	DESCRIPTION	303 ST. STL	ITEM
		TOLERANCES XX = $\pm .03$ XXX = $\pm .005$	W.O.	CALIFORNIA INSTITUTE OF TECHNOLOGY CENTRAL ENGINEERING SERVICES	CHG.
		FRACT $\pm 1/16$ ANG $\pm 1/2$	DATE	DWG. NO.	
	DRAWN BY	GY	5/93	PROPELLER CAVITATION TEST APPARATUS	A109242
	CHECKED				
	NEXT ASSY				

#4-40 THRU
4 EQ SP ON A
1.000 DIA. B.C.

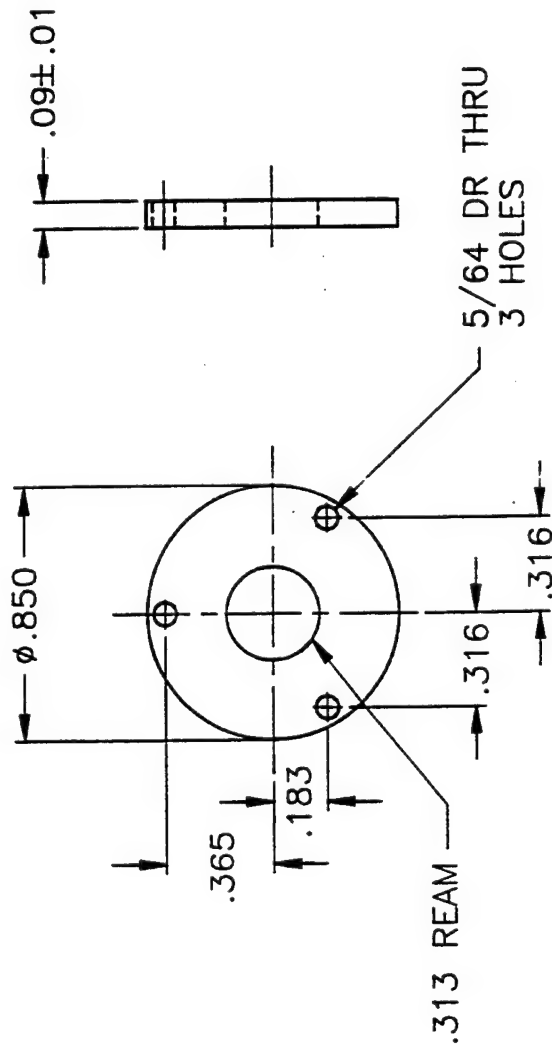


1	303 ST. STL		ITEM	
REQ	PART NO.	DESCRIPTION	MATERIAL	
TOLERANCES		W.O.	CALIFORNIA INSTITUTE OF TECHNOLOGY	
.XX = ± .03	FRACT ± 1/10	DATE	CENTRAL ENGINEERING SERVICES	
.XXX = ± .005	ANG ± 1/2	SCALE 1X	CHG.	
DRAWN BY GY	5/93	TITLE NUT PLATE		DWG. NO. A109243
CHECKED		PROPELLER CAVITATION		
NEXT ASSY		TEST APPARATUS		

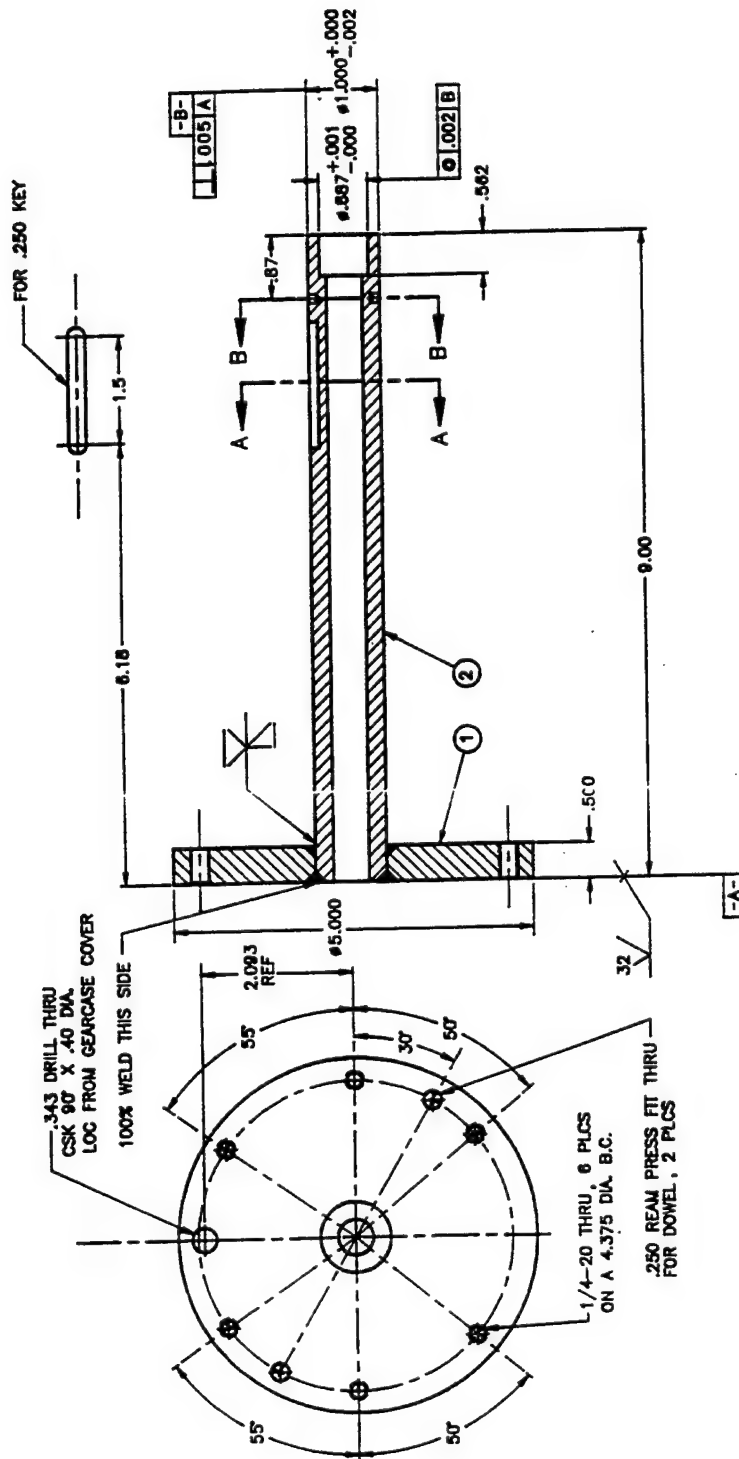


MODIFY LENGTH OF EXIST. .437 DIA. SHAFT

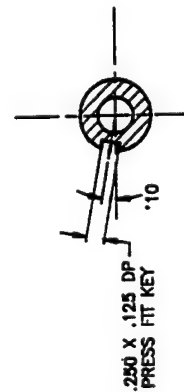
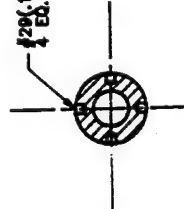
REQ	PART.NO.	DESCRIPTION	MATERIAL	ITEM
TOLERANCES .XX = ± .03 FRACT ± 1/16 .XXX = ± .008 ANG ± 1/2	W.O.	SCALE 1 = 1	CALIFORNIA INSTITUTE OF TECHNOLOGY CENTRAL ENGINEERING SERVICES	CHG.
DRAWN BY GY	7/93	TITLE DRIVE SHAFT, PROPELLER CAVITATION TEST APPARATUS	DWG. NO. A109245	
CHECKED				
NEXT ASSY				



1	303 ST STL		ITEM	
REQ	PART.NO.	DESCRIPTION	MATERIAL	
TOLERANCES		W.O.	CALIFORNIA INSTITUTE OF TECHNOLOGY	
.XX = ± .03		DATE	CENTRAL ENGINEERING SERVICES	
XXX = ± .005		SCALE	2X	
ANG ± 1/2		1/94	TITLE O-RING BACKUP-DWG. NO.	
DRAWN BY	GMV		PROPPELLER CAVITATION	
CHECKED			A109250	
NEXT ASSY			TEST APPARATUS	
			CHG.	



20(.156)DR., .12 DP
1 ED. SP. @ 90°



NOTE: PICKLE & PASSIVATE

1	2
1.250 O.D. X .500 I.D. 204 S.S. TUBE	2
204 S.S.	1
ENGINEER	DATE
CALIFORNIA INSTITUTE OF TECHNOLOGY	TEST NO.
CENTRAL ENGINEERING SERVICES	TEST DATE
100% WELD THIS SIDE	TEST TIME
1-1	TEST PLACE
TITLE INDEXING SHAFT	DWG. NO.
PROPELLER CAVITATION	C109228
TEST APPARATUS	

